multiphysics multiscale numerical modelling of the solidification of alloys under forced convection

Csaba Nagy

Communauté
UNIVERSITÉ Grenoble Alpes

MISKOLCI EGYETEM
UNIVERSITY OF MISKOLC

THÈSE

Pour obtenir le grade de
DOCTEUR DE LA COMMUNAUTE UNIVERSITE GRENOBLE ALPES
Préparée dans le cadre d'une cotutelle *entre la Communauté Université Grenoble Alpes* et Université de Miskolc

Spécialité : **Mécanique des fluides Energétique, Procédés**
Arrêté ministériel du 25 mai 2016

Présentée par
Csaba NAGY

Thèse dirigée par **Dr. Yves du Terrail Couvat** et **Pr. András Roósz**
codirigée par **Dr. Olga Budenkova**

préparée au sein des **Laboratoires SIMaP/EPM et Université de Miskolc**

dans **les Écoles Doctorales IMEP-2 (I**ngénierie - **M**atériaux, **M**écanique, **E**nvironnement, **E**nergétique, **P**rocédés**, P**roduction**) et Ecole Doctorale Antal Kerpely des science et technologie des matériaux (Université de Miskolc, Hongrie)**

Modélisation numérique multiphysique et multi-échelles de la solidification des alliages sous la convection forcée

Thèse soutenue publiquement le **7 Septembre 2018**,
devant le jury composé de :
Mme, Valéria, MERTINGER
Professeure á l'université de Miskolc (Président)
M, Mihály RÉGER
Recteur de l'université d'Óbuda (Rapporteur)
M, Henri, NGUYEN-THI
Professeur á l'universié d'Aix-Marseille (Rapporteur)
M, Menghuai, WU
Professeur agrégé á l'université de Leoben (Membre)

ANTAL KERPELY DOCTORAL SCHOOL OF MATERIALS SCIENCE & TECHNOLOGY

MISKOLCI EGYETEM

Multiphysic multiscale numerical simulation of the solidification of binary and ternary alloys under forced convection

A dissertation submitted in partial fulfillment of the requirements for the degree of Doctor of Philosophy in the subject of Material Science and Technology

by
Csaba Nagy

Supervisors:
András Roósz, Yves du Terrail, Olga Budenkova

Institute of Physical Metallurgy, Metalforming and Nanotechnology
MTA-ME Materials Science Research Group
Faculty of Materials Science and Engineering
University of Miskolc
Hungary

2018

Figures

Tables

Nomenclature

a	Radius of the grain	[m]
a, b	Coefficients proposed by Beckerman [6]	[-]
$\vec{A}$	Vector potential	[V•s•m^{-1}]
β_C	Volumetric solutal expansion coefficient	[1/wt.%]
β_T	Volumetric thermal expansion coefficient	[1/K]
B_0	Amplitude of the magnetic field	[T]
$\vec{B}$	Magnetic field vector	[T]
C_0	Initial concentration of solute	[wt.%]
$< C >$	Average concentration	[wt.%]
C_d	Solute concentration in interdendritic liquid	[wt.%]
C_f	Concentration in fluid	[wt.%]
C_l	Solute concentration in liquid phase	[wt.%]
C_l^E	Liquid concentration in the eutectic point	[wt.%]
C_l^*	Equilibrium concentration denoted to thermodynamic temperature	[wt.%]
c_p	Specific heat	[J/K]
C_s	Concentration in the solid phase	[wt.%]
$\bar{C}_x$	Solute concentration on solid – interdendritic interface (x: side of solid: “sd”, side of liquid: “ds”)	[wt.%]
C^*	Concentration according to phase diagram	[wt.%]
$\bar{C}_s$	Concentration on the interface of solid and liquid	[wt.%]
$C_{x,f}$	Concentration of solute x (Si or Fe) in fluid phase	[wt.%]
$C_{x,y}$	Concentration of solute x (Si or Fe) in phase y (α or β)	[wt.%]
δ	Diffusion length in solidification or electromagnetic skin depth	m
δ_e	Effective skin depth	m
D_l	Diffusion coefficient in liquid	[m^2/s]
EDL	Extradendritic liquid	[-]
$\vec{E}$	Electric field vector	[V/m]
$\vec{e}_z$	Unit vector	[-]

f	Frequency	[Hz]
f_α	Phase fraction of α	[-]
f_β	Phase fraction of β	[-]
f_d	Interdendritic liquid phase fraction	[-]
$\vec{F}_{em}$	Electromagnetic force density	[N/m^3]
f_f	Fluid phase fraction	[-]
f_g	Grain phase fraction	[-]
f_l	Extradendritic liquid phase fraction	[-]
$\vec{F}_L$	Lorenz force	[N]
$\vec{F}_{L,RMF}$	Lorenz force of RMF	[N]
f_s	Solid phase fraction	[-]
F_*	Lorenz force components (* = r,z or θ)	[N]
G	Thermal gradient in solidification or side parameter in electromagnetic equations	[K/m]
g	Gravitational acceleration	[m/s^2]
i	Imaginary part	[-]
IDL	Interdendritic liquid	[-]
$j_{ex,\theta}$	Instantaneous value of current	[A]
J_*	Electric current components (* = r,z or θ)	[A]
$\vec{J}$	Electric current vector	[A]
k	Wave number vector	[-]
K	Permeability of the porous zone (Karman-Cozeny)	[-]
k_p	Partition coefficient	[-]
k	Kinetic energy	[J]
$k_{x,\alpha}$	Segregation coefficient of solute x (Si or Fe) with α	[-]
L	Latent heat	[J/kg]
λ	Wave length or thermal conductivity	[m]
$\lambda_{2,ini}$	Initial secondary dendrite arm spacing	[m]
λ_1	Primary dendrite arm spacing	[m]
λ_2	Secondary dendrite arm spacing	[m]

λ_i	Characteristic size of a sinusoidal perturbation	[m]
λ_θ	Angular wave length	[m]
l_{ld}	Diffusion length in liquid phase by Beckerman [6]	[m]
l_{sd}	Diffusion length in solid phase by Beckerman [6]	[m]
m_l	Liquidus slope	[-]
m_*	Liquidus slope of solute * (Si or Fe)	[-]
μ_*	Dynamic viscosity (*: l for liquid phase, f for fluid phase)	[Pa•s]
μ_0	Magnetic permeability of vacuum	[-]
n	Density on grains	[1/m^3]
∇	Nabla operator	[-]
ν	Kinematic viscosity	[m^2/s]
ω	Angular velocity of the liquid	[rad/s]
Ω	Constitutional supercooling	[K]
p	Number of pole pairs	[-]
Φ	Any differentiable function	[-]
φ	Phase shift	[-]
$\Phi(\frac{r}{R})$	Function depending on the skin depth	[-]
$\psi(z)$	Variation of the axial magnetic field due to the size of the inductor	[-]
$\vec{P}$	Any vector	[-]
q_{Ohm}	Ohm's heating	[W/m^2]
R	Radius of crucible	[m]
r	Radial coordinate	[m]
R_e	Real part	[-]
ρ	Density	[kg/m^3]
ρ_0	Initial density	[kg/m^3]
$\tilde{\rho}$	Density calculated using Boussinesq equation	[kg/m^3]
R_{tip}	Radius of dendrite tip	[m]
R_{TOT}	Maximal envelope radius	[m]

S_g	Surface density of grain	[kg/m^2]
Γ	Gibbs-Thomson coefficient	[K•m]
σ	Electrical conductivity	[S/m]
Γ_*	Mass transfer rate of phase *	[kg/s]
$< >$	Average	[-]
$< >^*$	Average in phase *	[-]
T	Temperature	[K]
ΔT_0	Initial supercooling	[K]
τ	Polar step of inductor	[m]
θ	Angular coordinate	[rad]
T_l	Liquidus temperature	[K]
T_m	Melting point of the pure metal	[K]
T_0	Initial temperature	[K]
T_{th}	Thermodynamic temperature	[K]
$\vec{u}, \vec{v}, \vec{w}$	Velocity vector	[m/s]
u_θ	Velocity of material in the magnetic field	[m/s]
U_s	Magnetic field movement velocity	[m/s]
v	Solidification front velocity	[m/s]
$\vec{v}_f$	Velocity of fluid	[m/s]
v_{sample}	Sample lowering velocity	[m/s]
$\vec{w}_g$	Average growth velocity of the grain	[m/s]
z	Axial coordinate	[m]

Introduction

Aluminum and aluminum-based alloys are widely used in industry due to the corrosion passivity, lighter weight, yet – in several cases – comparable strength with steel. Often, the material is used "as-cast", that means that composition, macro- and microstructure of the material emerged during the casting define its behavior under different loads. Yet, convective flows generally arise in casting processes performed on-ground because of gravity. They modify local solidification conditions, and, consequently, solute distribution and affect properties of material. To understand and to be able to control such phenomena, detailed experimental and numerical work has been needed.

Two Bridgman-type furnaces were constructed in the University of Miskolc, Hungary, by MTA-ME Materials Science Research Group in the framework of the ESA funded MICAST project for experimental study of the effect of convective flow in solidification of alloys. These facilities were equipped with electromagnetic systems capable to generate rotating and travelling magnetic fields of various intensities.

Multiphase models developed at SIMaP/EPM, Grenoble, France, were applied for numerical study of the solidification of binary and ternary aluminum alloys under electromagnetically generated convective flow. Solidification of a binary Al-Si alloy under RMF stirring was done with Euler-Euler ensemble averaging and lever rule mesoscale models coupled with the macroscale transport both in 2D and 3D geometries. Further, effect of various modes of TMF stirring during solidification of a ternary alloys was studied in 3D geometry with lever rule based macroscopic model. Results of numerical simulations well explain the segregation observed in the experimental samples.

1. Chapter:
State of the art

1.1. Why aluminum-based alloys?

Aluminum is one of the most used metal around the world together with iron-based alloys, however the 1/3 specific weight ratio compared to iron provoked strong research and development work around aluminum-based alloys. Nowadays, it is hard to think where aluminum is not used. Starting from the simplest machines like bicycles, through passenger and heavy-duty vehicles, until airplanes and spaceships, aluminum has a major role. Bicycles have their frames, crankarms, main brake components, wheels based on aluminum. More-and-more cars have their bodywork made of aluminum, moreover the engine block, engine head, transmission housing, air condition parts, suspension parts, steering rack housings, heat exchangers, etc. made from aluminum-based alloys.

Several components like engine blocks and heads, different housing parts, bicycle brake components are used in as-cast condition including only complex CNC machining which is not affecting the structure or strength on the material itself (only the mechanical stability of the part / structure can be modified likewise). Regarding such a fact, it is essential to know the deepest details of how the parts is being made. If the structure of the metal is unknown, unwanted effects can appear and it can even be hazardous for human health.

Under terrestrial circumstances, melt flows are always appearing during casting processes. Any kind of flow is somehow modifying the concentration and / or temperature distribution inside the part which can result in porosity or macrosegregation. The second case is harder to keep in control and (also as porosity) have unchangeable effects on the part's properties, which cannot be changed with heat treatment or other processes.

For the investigation of the effect of the melt flow on the solidified structures, an ESA financed project series has started called MICAST (Microstructure Formation in Casting of Technical Alloys under Diffusive and Magnetically Controlled Convective Conditions) [1]. Several research groups were part of the work from France, Germany, USA, Austria, Hungary, etc. The main aim was to investigate the structure of various alloys in Earth and space (microgravity) conditions including forced convection. Electromagnetic stirring was chosen for the convection method since it can be performed without touching the metal and like this, the results can be closer to a real industrial case.

The aim of the current thesis is to numerically simulate the solidification cases realized with the experimental facilities equipped with travelling or rotating magnetic field stirrers in Miskolc and validate the results with the experimental data of MTA-ME Materials Science Research Group.

1.2. Microstructure related to solidification conditions – a general theory

Quantitative description of the microstructure binary metallic alloys and other materials are described via binary phase diagrams. Several models have been developed so far, but the simplest solution is still the so-called Lever rule.

The relation between liquid composition (concentration on solute in liquid) is described as the following:

$$C_l = \frac{C_0}{(1-k_p)f_l+k_p} \tag{1.1}$$

Where C_L is the liquidus composition, C_0 is the initial concentration of the melt (nominal composition), f_L is the liquid fraction and k_p is the segregation coefficient, which means the ratio between solid and liquid phases, assumed to be constant.

Figure 1.1 presents an arbitrary binary phase diagram where B material has limited solubility in alpha and eutectic forms on a specified temperature (+ A material has zero solubility in beta phase).

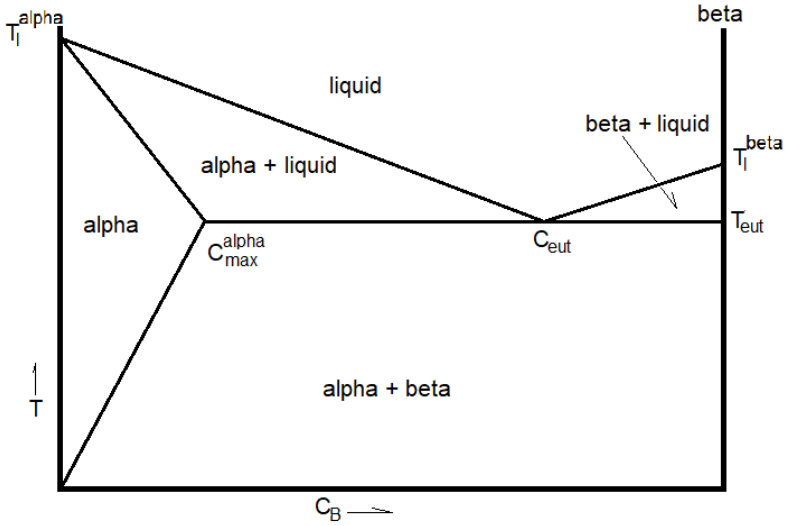

Figure 1.1 Binary phase diagram example

The lever rule can easily be visualized on a diagram like on Figure 1.2. The fraction of each phase and the concentration of solute can be declared easily.

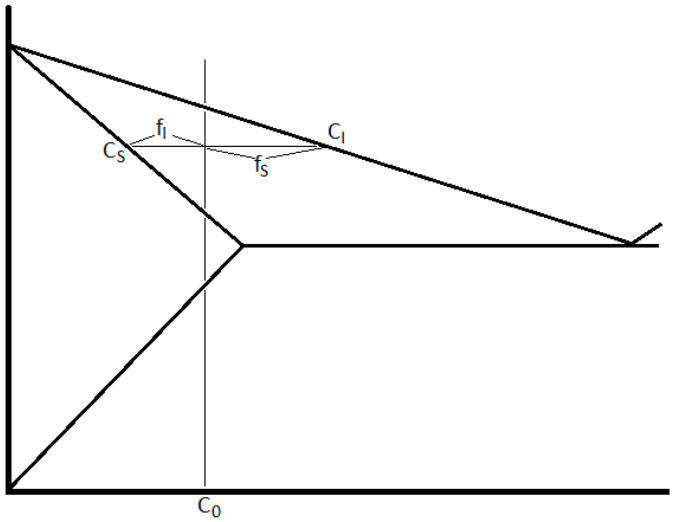

Figure 1.2 Visualized Lever rule

If the cooling of the melt starts, the solidification is not starting immediately on the liquidus line, since the undercooling of the liquid is needed for the formation of nuclei. Figure 1.3 presents the critical nucleus radius – ΔG as a function of nucleus radius.

The atoms are always hitting each other and forming unstable nuclei in the melt. If enough big agglomeration of atoms can be formed, a stable nucleus is generated, and crystal growth starts.

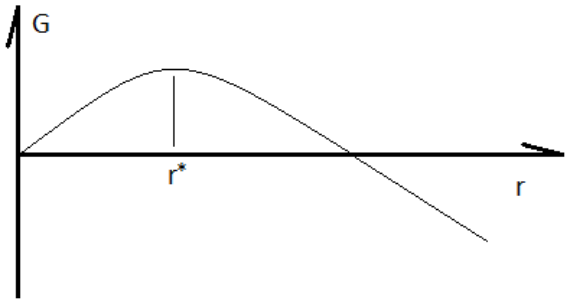

Figure 1.3 Critical nucleus size (r^*)

This process is called « homogeneous nucleation ». In fact, in the beginning of the solidification process the nucleation happens over the walls of the container filled with the liquid metal over the sites preferable from the energetic point of view (increased solid surface). In the bulk, the nucleation happens over impurities which are always present in the liquid, on the pieces of oxide film entrained from the surface of the sample inside the sample by flow, on the gas bubbles etc. Some refined particles can be introduced into the melt intentionally to increase the number of nucleus. In the case of nucleation over a seed, the process is named « heterogeneous nucleation ». Another origin for nucleation is fragmentation of dendrites. Depending on the cooling rate, several growth forms can happen – Figure 1.4. If the thermal gradient can be changed significantly, columnar to equiaxed transition can occur.

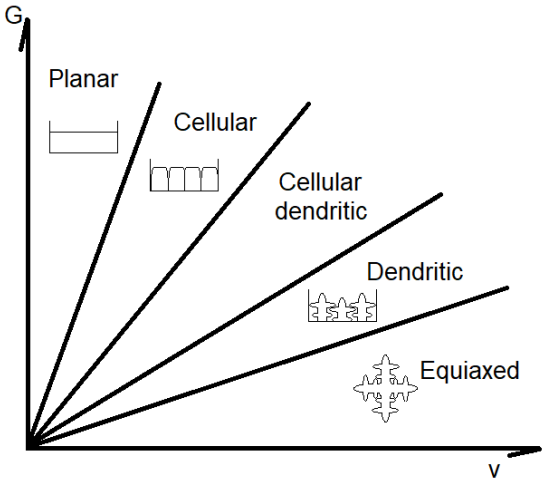

Figure 1.4 Form of growth depending on the thermal gradient (G) and growth rate (v)

Depending on the alloy type and the solidification conditions, several final structures can be achieved which can significantly change the properties of the product. The phase

diagram defines what kind of phases can be expected. Then the cooling rate and the flow of the melt can modify the crystallographic structure – mainly the grain size. Also macrosegregation can occur, which is mostly an unwanted result, since special phases can appear also, modifying the tensile stress or the thermal conductivity of the product.

This is true both for pure materials and mixture, i.e. alloys. Yet, since the growth of the pure material is governed by the thermal conditions, dendritic solidification can be rarely observed and occurs only with extremely fast cooling rates that lead to the large thermal under cooling of the liquid ahead of the solidification front.

For the alloys which present, actually, a mixture of two materials, the melting temperature (liquidus temperature) depends on the local composition of the mixture. Consequently, two processes define the local melting temperature: the heat transfer and the transport of the solute. In the absence of convective flows, the speed of the former process is defined by a thermal diffusion, while the solute transport is governed by the chemical diffusion whose value is at least two orders less, that means that the solute transport is at least 100 times slower than the heat dissipation. During solidification, a latent heat is released, and the solute is rejected at the solid-liquid interface. The released heat is evacuated through the lateral boundary and a cooler mushy and solid zone. The rejected solute rests in the liquid and, because of slow diffusion process, forms a « pile-up » ahead the solidification front. A schematic view for the distribution of the temperature and the solute in the pure liquid ahead the solidification front moving with the velocity V during stationary growth is presented in Figure 1.5.

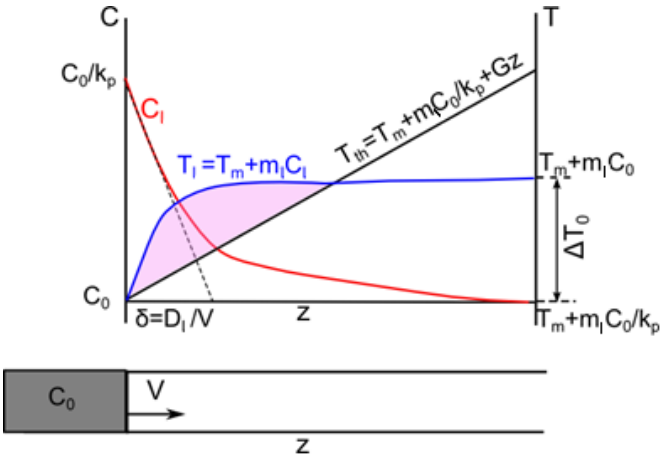

Figure 1.5 Presentation of a linear distribution of the thermodynamic temperature T_{th} (black line) defined by the thermal gradient G, solute profile C_l (red line) and the liquidus temperature $T_l = T_m + mC_l$ (blue line) in the pure liquid ahead of the solidification front moving with a stationary velocity V. The maximal solute value in the liquid is defined by the partition coefficient k_p and the thickness of the boundary diffusion layer is $\delta = D_l / V$ with D_l for chemical diffusion. The undercooled zone $T_{th} < T_l$ is shown in a rose color (after Kurz and Fisher [34]).

Because of the accumulation of the solute in the vicinity of the solid-liquid interface, the thermodynamic temperature defined by the imposed thermal gradient, may occur below the liquidus temperature, i.e. the liquid is “constitutionally undercooled”. Moreover, this undercooling increases toward the pure liquid that means that if a local perturbation like a protrusion occurs, it will grow further toward the pure liquid, i.e. it will increase.

A more rigorous analysis of linear stability performed by Mullins and Sekerka [31] allowed estimation of a characteristic size of a sinusoidal perturbation λ_i which will survive because of the constitutional undercooling given as

$$\lambda_i > 2\pi\sqrt{\frac{k_p D_l \Gamma}{V m_l C_0 (1-k_p)}} \qquad (1.2)$$

Further, the minimal value of λ_i was associated with the radius of dendrite tips R_{tip} (Figure 1.6) which appear under given conditions. Another two characteristic sizes for the dendritic growth are primary arm spacing λ_1 and secondary arm spacing, λ_2 (Figure 1.6).

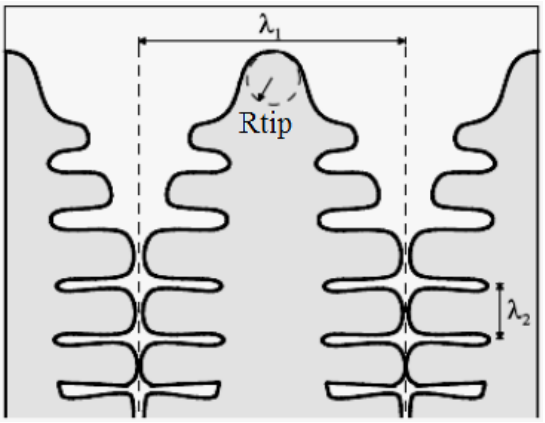

Figure 1.6 Illustration to the characteristic sizes in denrtitic growth: the tip radius R_{tip} and primary λ_1 and secondary λ_2 dendrite spacing [57]

Several equations were proposed for the estimation of the primary arm spacing in an alloy solidifying under diffusional growth Trivedi [32], Hunt [33], Kurtz and Fischer [34], all have the same dependence on the thermal gradient, growth velocity and constitutional undercooling that can be given as:

$$\lambda_1 \approx A\left(\Delta T_0^{1/4} G^{-1/2} V^{-1/4}\right) \qquad (1.3)$$

with ΔT_0 for the constitutional undercooling illustrated in Figure 1.5 and different constant A, depending on the model.

According to Ciobanas and Fautrelle [35], the secondary arm spacing at the moment they form is defined as

$$\lambda_{2,ini} \approx 2R_{tip} = 2\lambda_i \tag{1.4}$$

After some period of time the, secondary arms continue to growth inside the mushy zone filled with a highly enriched liquid and a so-called « coarsening » happens during their growth. The coarsening consists in eliminating of widening of some (larger) branches at the expenses of thinner branches (which disappear), so the initial distance $\lambda_{2,ini}$ increases with solidification time as [34]:

$$\lambda_2 = 5.5(Mt)^{1/3} \tag{1.5}$$

$$M = {\Gamma D_l \ln(C_l^E/C_0)}\Big/{m_l(1-k_p)(C_0 - C_l^E)} \tag{1.6}$$

Role of convection in solidification

Convective flow may develop naturally in every crystallisation process under on-ground convection because of natural convection mainly due to lateral thermal gradients existing in almost all set-ups, even if a stable configuration (cold zone in the bottom) is adopted. Also, if solidification of an alloy with components of large density difference is performed, convection occurs due to the segregation during the solidification and accumulation of the solute in the liquid (fig.). Convection, being caused by the variation in temperature and concentration, further affects the heat and mass transfer that creates a positive feedback. As a result, the strong accumulation and impoverishment can form during the solidification of an ingot.

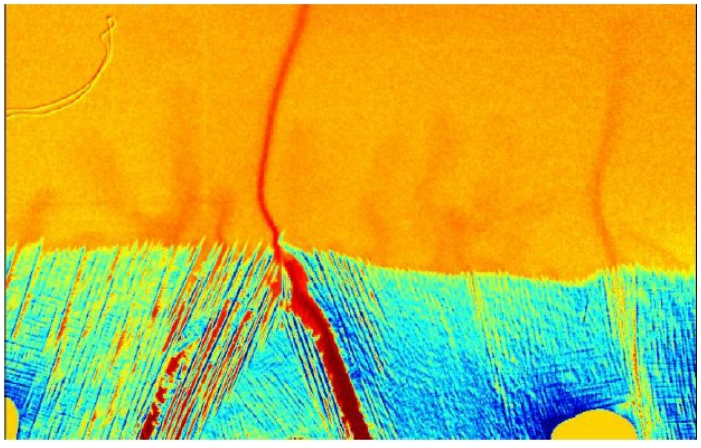

Figure 1.7 Formation of plumes (freckles) in the pure liquid ahead of the solidification front and channels inside the mushy zone in solidification of the In-75wt%Ga alloy observed in-situ with X-Ray imaging technique [36][37]

Since natural convection is unstable and cannot be controlled, the idea to counter-pose it with a controlled forced convective flow seems to be highly attractive. The latter can be generated in different ways, in particular, using the effect of the electromagnetic induction, as discussed below in this chapter. Yet, the effect of the forced convection is not straightforward since via its influence on the heat and mass transport it affects also the evolution of the microstructure. Depending on the local direction and intensity of the convective flow the primary and secondary arm spacing can be altered differently. Generally, it is supposed that the primary arm spacing diminishes with the convective flow because of better evacuation of the solute away from the dendrite tips yet, in Figure 1.8 an increase of the primary arm spacing is shown in solidification of Ga-In after a forced flow was generated [36].

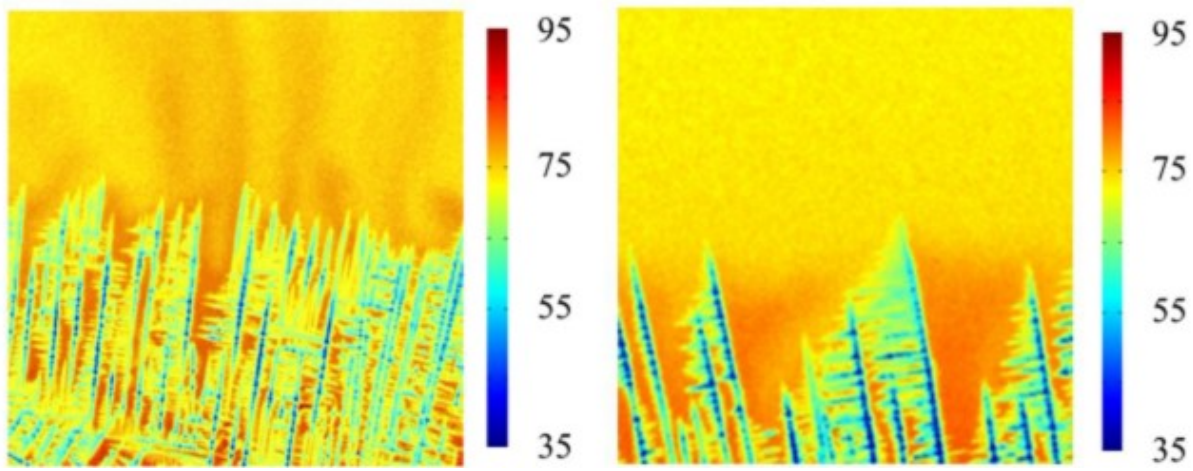

Figure 1.8 In situ radiographs during solidification of thin sample experiments showing microstructure morphology and concentration (%wt. Ga) in the melt. Left: Natural convection. Right: Forced convection (flow is from left to right).

Moreover, it is generally expected that more intense fluid flow occurs mechanical impact on the solidified dendrite and may promote their fragmentation: detachment of the small parts of dendrites. Since these fragments can serve as nucleation centers, increase of their number would promote equaixed solidification growth.

1.3. Effect of electromagnetic stirring on the solidified structure

Aphrodité benchmark experiment

For the investigation of TMF stirring's effect on the solidified structure, a benchmark experiment was designed in SIMaP/EPM laboratory and solidification tests were performed by [57] et al. The experimental setup holds a thin rectangular volume of melt with the possibility of electromagnetic stirring. The side of the sample is equipped with a raster of thermocouples, which is used to monitor the temperature distribution during the experiment. The magnetic field is provided by a linear motor and has limited penetration into the melt, so the liquid is partially stirred with the field and partially by the shear stress of the flow. The sketch of the setup can be seen on Figure 1.1.

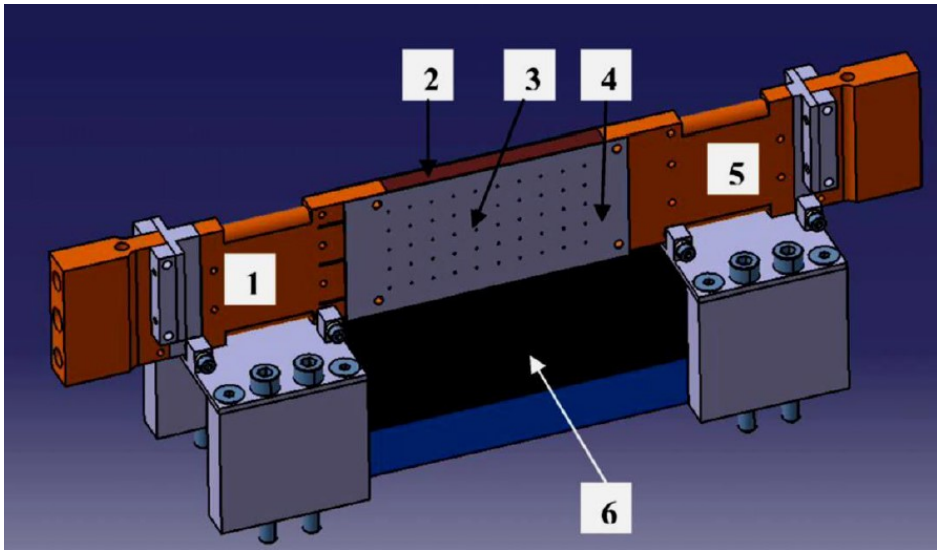

Figure 1.9 The experimental setup designed in SIMaP/EPM – AFRODITE–II. 1: left heat exchanger, 2: Sample, 3: raster of thermocouples, 4: Stainless steel sample holder, 5: right heat exchanger, 6: linear motor [57]

The solidified macrostructure of Sn-10wt.%Pb can be seen on Figure 1.10. Four different cases are presented. (a) is with natural convection. (b) is with mixing in the direction of the natural convection. (c) is with convection in opposed direction of the natural convection and (d) is with alternating mixing with the frequency of 0.,125 Hz. The columnar to equiaxed transition is achieved in all cases, but the structure can be strongly refined with the choice of the correct stirring.

The results can be useful for the development of different solidification models and numerical approaches, moreover unknown structures can be realized. The effect of the melt flow on the microstructure is clear (depending on the type of convection). Such results' comparison will be performed in the work later on, either the results of the experiments reflects to a particular set of the related phenomena.

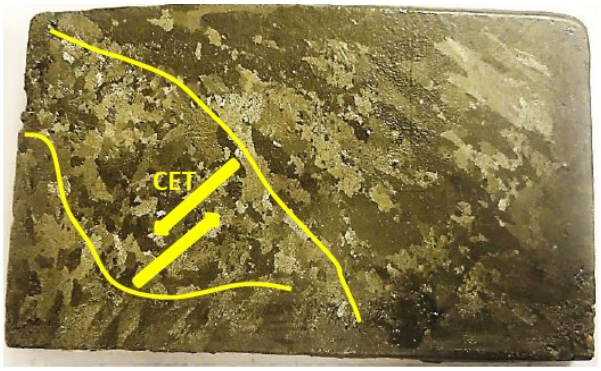

(a) Natural convection

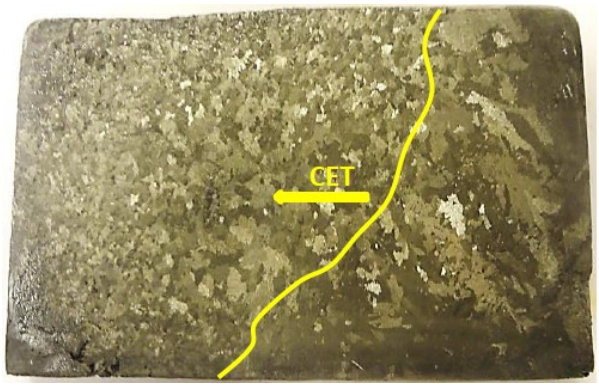

(b) Forced convection in the direction of the natural convection

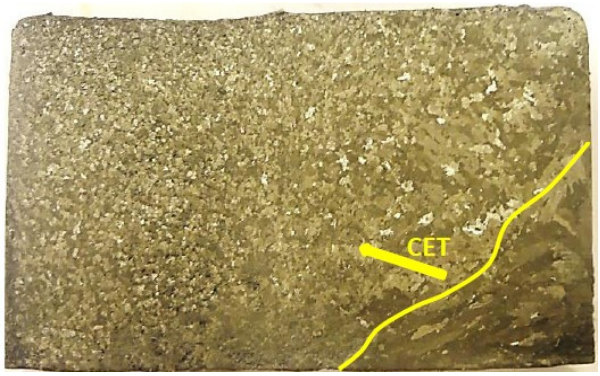

(c) Forced convection in opposed direction of the natural convection

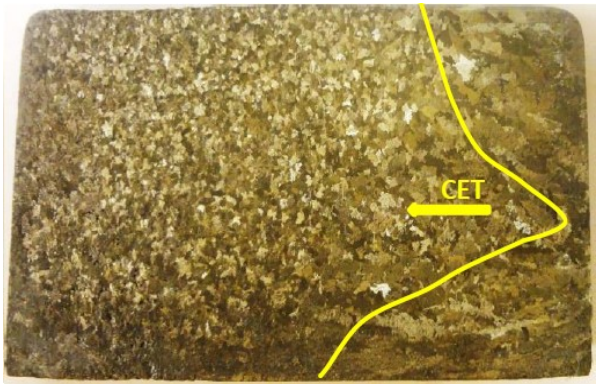

(d) Forced alternating convection

Figure 1.10 Experimental results on Sn-10wt.%Pb alloy in the APHRODITE-II system [56]

Reduction of grain size in copper alloys

Several research groups are working to investigate the effect of melt flow on the solidified metallic structure. Using RMF or TMF field, the control of the grain size or columnar to equiaxed transition is achieved, but also new – yet unknown – structures are provided. Most of the model alloys are aluminum-based (Al-Si, Al-Mg-Si, Al-Ni), but results on tin and copper alloys also can be found.

Zhiming Yan et al [52] were solidifying a hollow Cu-Ni tusk and were controlling the grain size using RMF stirring. The sketch of the machinery is the following (Figure 1.11):

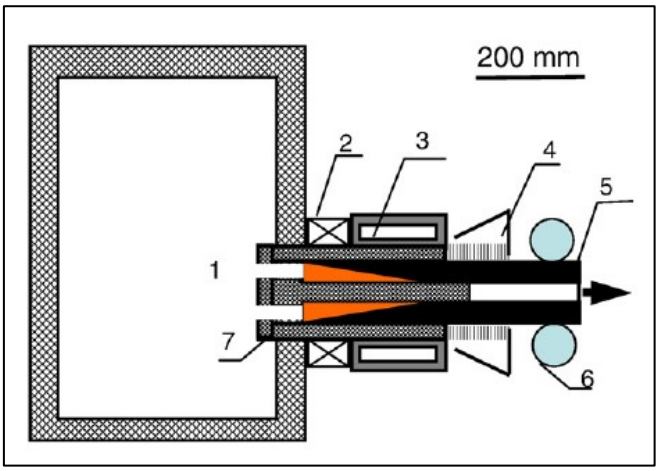

Figure 1.11 The melt (no. 1) is passing thru the RMF stirrer (no. 2), then solidifies in the crystallizers (3–4). The tusk indicated as no. 5 is pulled out by the mechanism (no. 6) thru the casing (no. 7).

Figure 1.12 shows the structure of stationary and mixed case. The difference in the grain structure is visible even without deeper investigation.

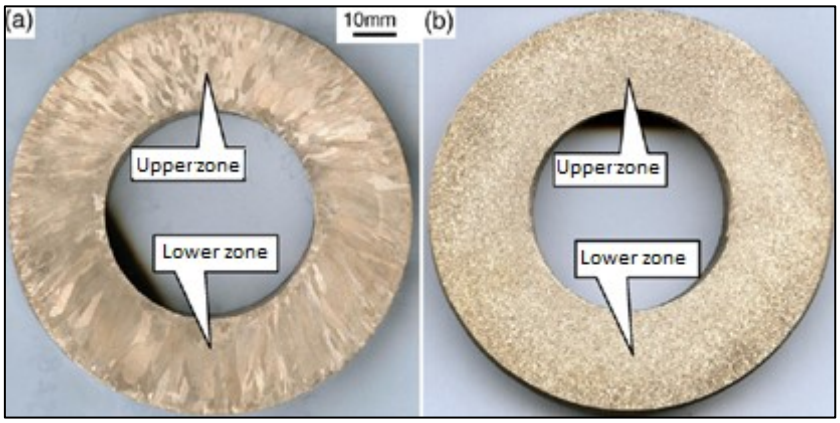

Figure 1.12 Effect of RMF mixing on the grain structure of a Cu sample

Continuous casting of steel under RMF

Karel Stransky et al [53] were researching the effect of RMF stirring on the solidified structure of continuously cast iron. The stirring was applied on the crystallizer and after the first and second supporting rollers (Figure 1.13 a)). On Figure 1.13 b, the solidified dendritic structure can be seen with and without stirring. If the stirring is applied, the ratio of columnar structure is significantly lower and the central core's size is lowered.

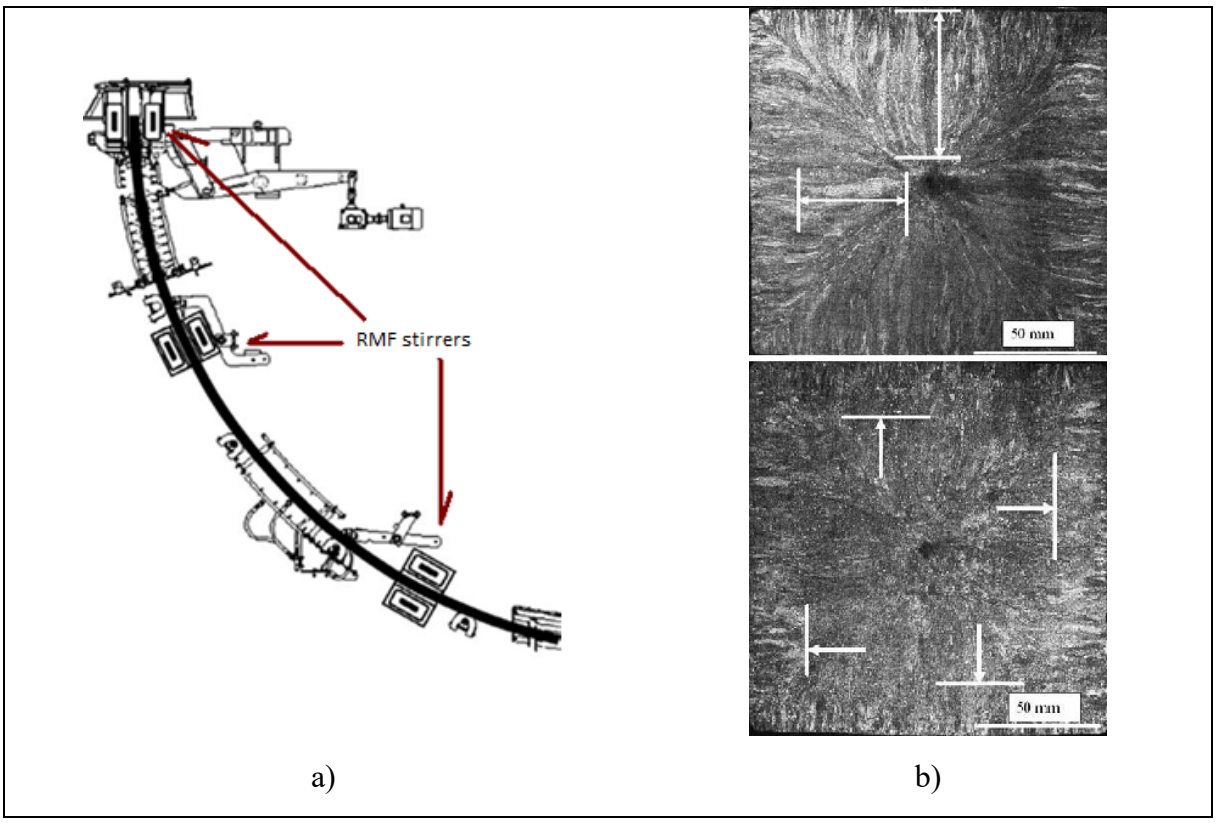

Figure 1.13 RMF stirring on continuously cast-iron billet

Al-Si-Mg ternary alloy under weak RMF field

S. Steinbach and L. Ratke [54] were investigating the effect of RMF stirring on the microstructure of Al-Si-Mg alloy. Figure 1.14 shows the difference between the stable and mixed part's structure. The experiments were made in a classical Bridgman type furnace using weak – 3 mT – rotating magnetic field. Even this force have waken macrosegregation.

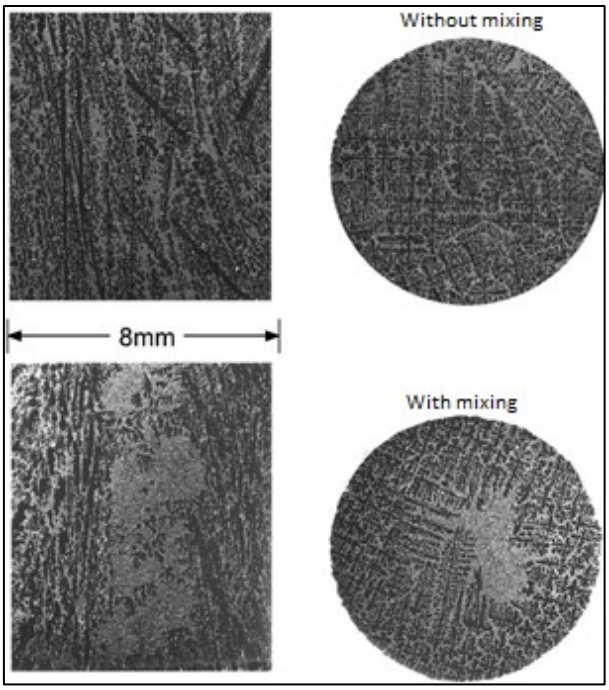

Figure 1.14 Al–Si–Mg alloy's microstructure with and without RMF stirring

Pb-Sn alloy's structure with RMF stirring – CET

S. Eckert et al [55] were investigating the effect of RMF stirring on the columnar to equiaxed transition of Pb-Sn alloy. The CET occurs right in the moment when the magnetic field is turned on. The effect is also visible on the microstructure.

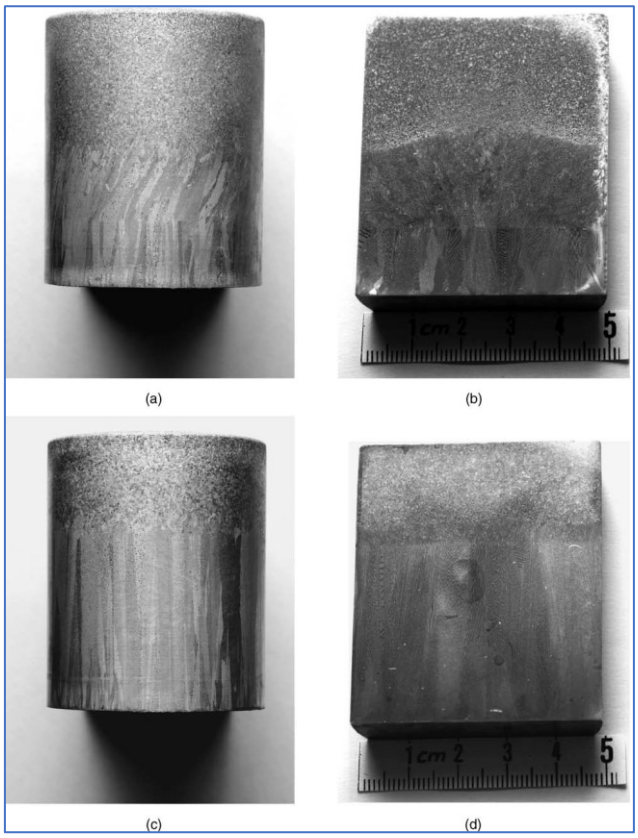

Figure 1.15 CET zone in Pb–Sn alloy

Effect of RMF stirring of Al based alloys

In Hungary, only the host institute of this PhD project – MTA-ME Materials research Group – is working on the research of solidification under forced convection. J. Kovács et al [56] were examining the effect of the flow on the macro- and microstructure of binary and ternary eutectics. Comparison experiments were done with identical conditions, but with and without stirring.

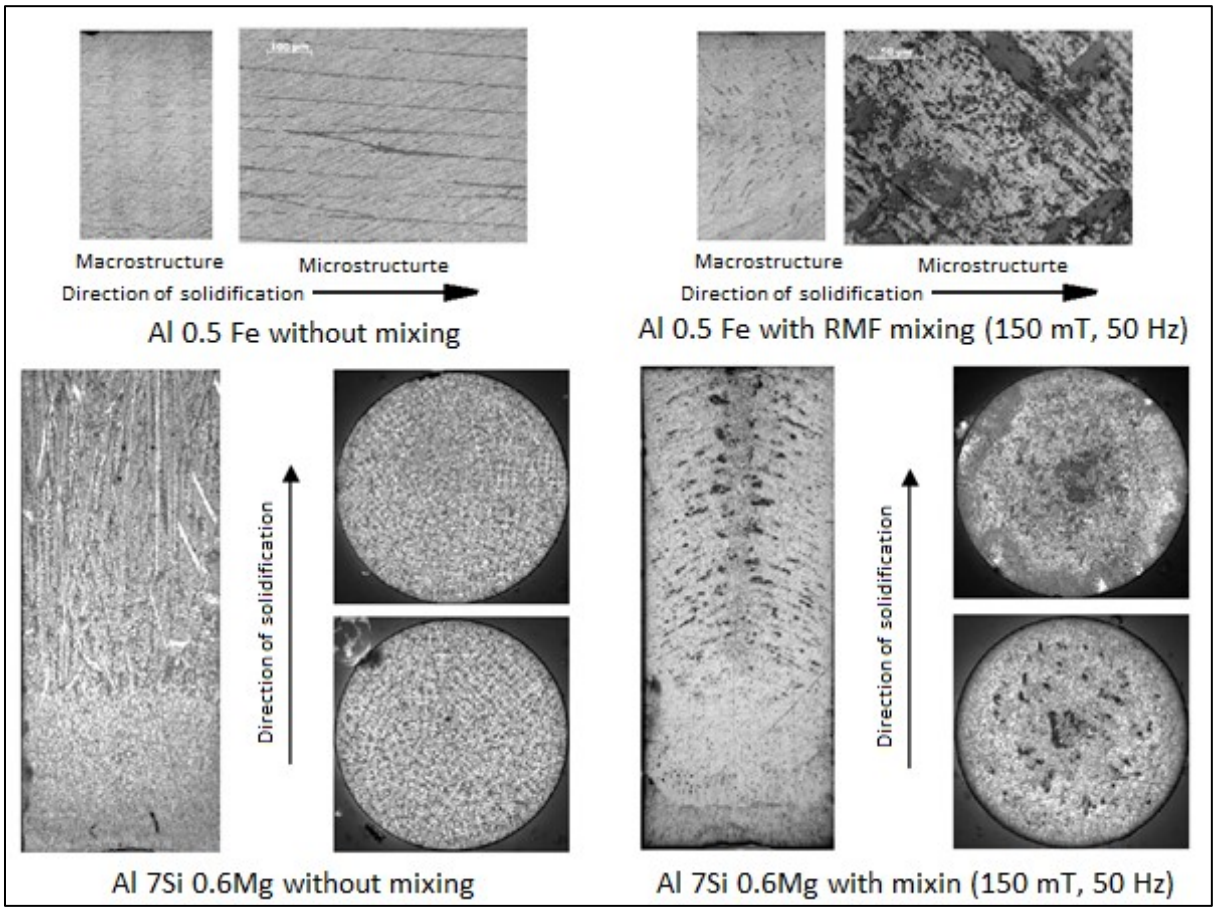

Figure 1.16 Structure of unidirectionally solidified Al0,5Fe and Al7Si0,6Mg alloy with and without RMF mixing [56]

On Figure 1.16, the structure of Al0,5Fe and Al7Si0,6Mg is presented with and without RMF stirring – 150 mT, 50 Hz. Even the low alloying content of the first metal shows central macrosegregation. The mentioned structure appears even stronger inside the higher alloyed specimen. The axis-wise macrosegregation presented by Steinbach is appearing here too.

Free surface of the melt, measurement of angular velocity in RMF

A. Rónaföldi et al [51] have performed several experiments to investigate the effect of forced convection on the solidified structure. Many times, the free surface of the melt solidified in a paraboloid, which came from the stirring itself. The sketch of the case can be seen below.

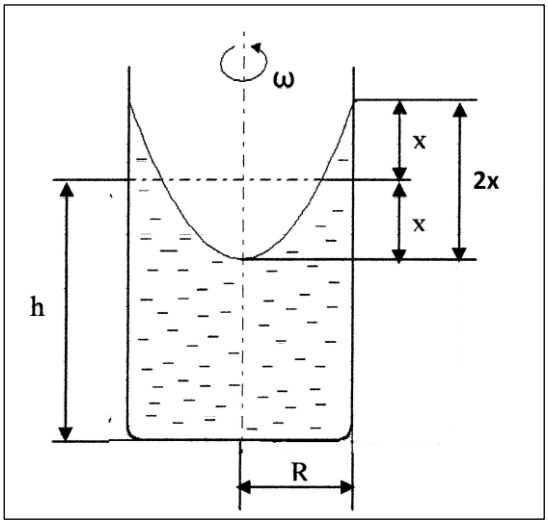

Figure 1.17 Form of the free surface during mixing

The correlation between the height of the paraboloid and the angular velocity is as follows:

$$2x = {(R^2\omega^2)}/{2g} \qquad (1.7)$$

The exact mechanism of the solidification in the top section is still unknow. Several parameters can influence the shape and dimensions of the free surface:

- Stationary height of the melt
- Temperature gradient
- Cooling rate
- Thickness of the mushy zone
- Surface wetting and surface tension

Examples on the “frozen” free surfaces can be seen in Figure 1.18.

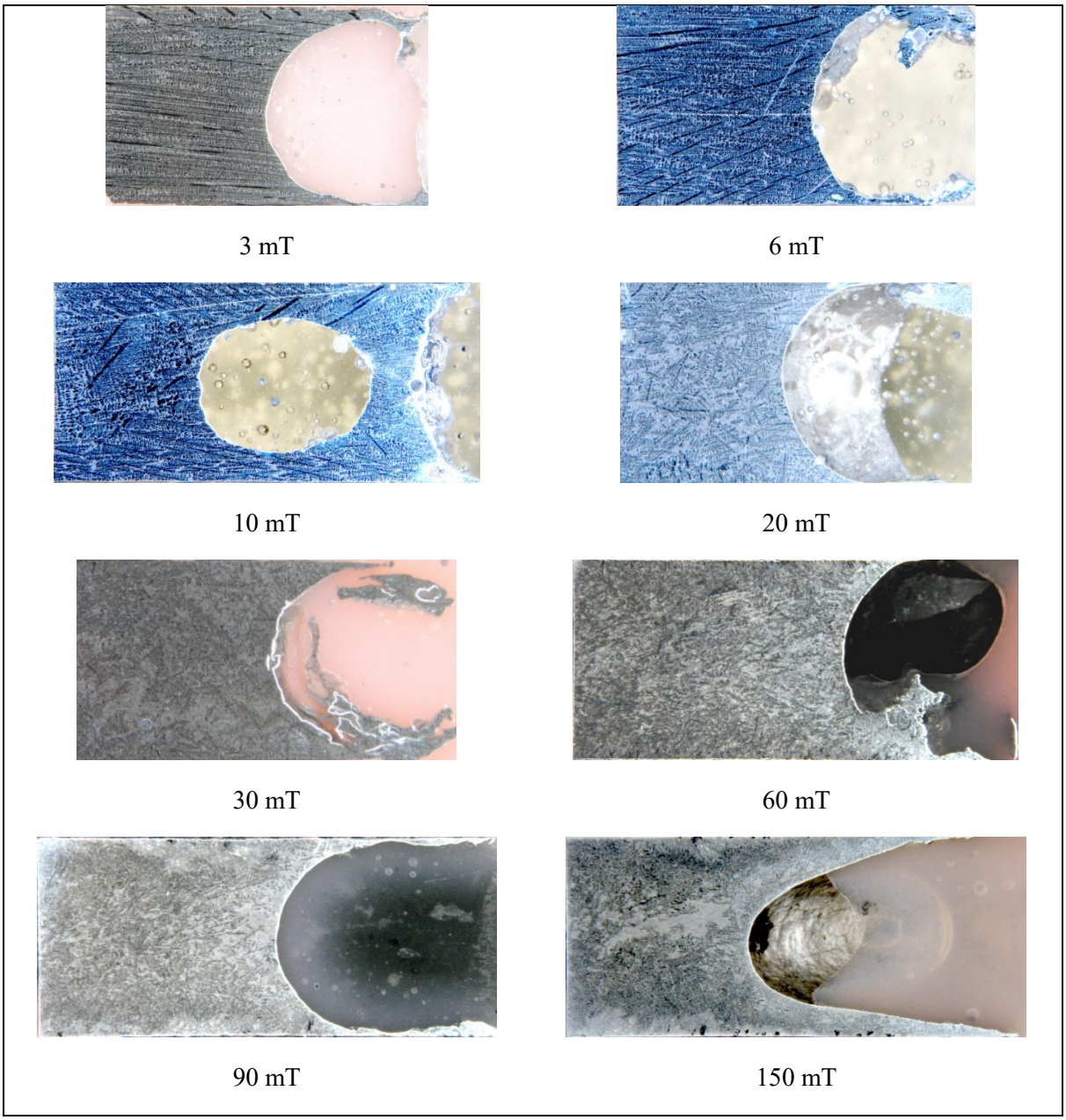

Figure 1.18 Frozen free surfaces of aluminum samples

The phenomena appearing on the free surface of the melt can be used for measuring the average volumetric angular velocity of the liquid, which was also used by Rónaföldi. The so-called “pressure compensation method” is based on the Bernoulli equations. As the melt rotates, the metallostatic pressure is pushing the liquid to the wall of the crucible and due to this pressure, also starts to climb up the wall. In laminar case, on the top layer of the surface, the melt turns back to the center of the crucible and starts to flow outside again. If a semi-closed crucible is prepared, the compensation pressure for reaching the “flat” melt surface during rotation can be measured and using the results, the average angular velocity of the media can be computed.

The experiments were useful to be able to see the validity of the mathematical approach presented. According to the visual comparison, the equations can be used.

Effect of RMF stirring on primary and secondary dendrite arm spacing

In the framework of MICAST V. project, an experiment series was performed in MTA-ME Materials Science Group by A. Roósz et al [58] on Al-7wt.%Si-1wt.%Fe to investigate the effect of weaker rotating on the solidified structure focusing on grain size, primary- and secondary arm spacing. The sample was Ø8x100 mm. 50 mm was solidified without stirring and the rest with stirring on constant induction. Each induction level had different dedicated sample. Figure 1.19 and Figure 1.20 presents the results.

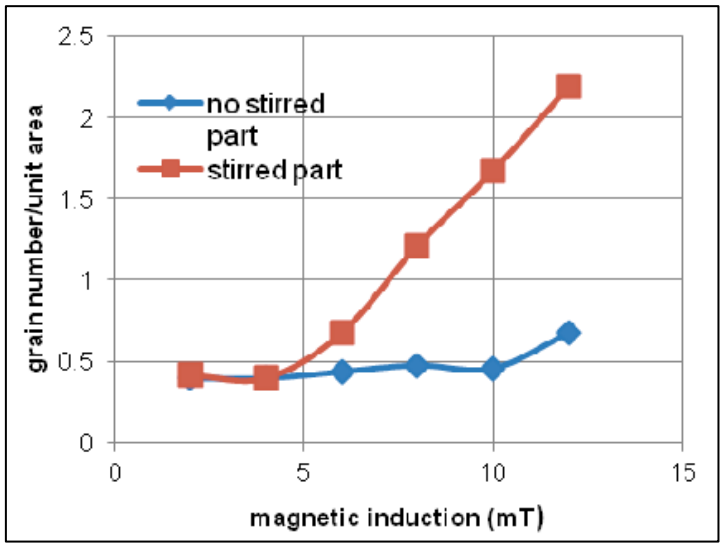

Figure 1.19 Effect of RMF stirring on the grain size [58]

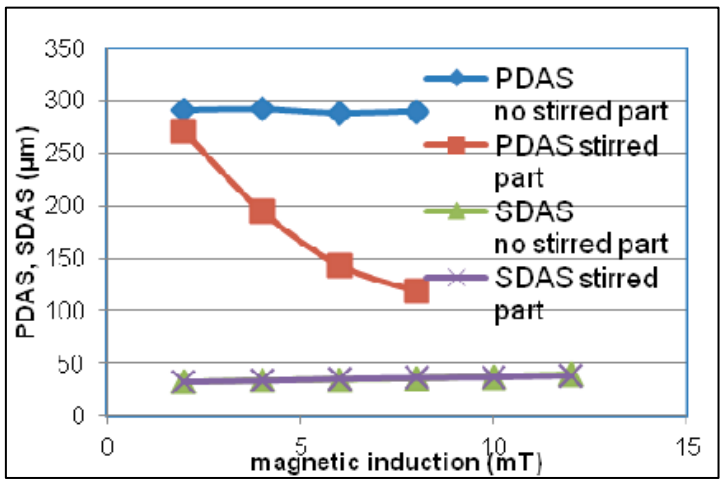

Figure 1.20 Effect of RMF stirring on the primary (PDAS) and secondary (SDAS) dendrite arm spacing [58]

The grain structure has been refined significantly which is related to the change of thermal and solutal environment near the dendrite tip and possible fragmentation of the dendrites – resulting in individual equiaxed grain growth. The primary dendrite arm spacing could be measured only in parts, where columnar grains were still visible. The secondary dendrite arm spacing stayed constant. Such effect will be significant for calculating the Karman-Cozeny constant for the porous flow in the mushy zone in chapter 3.

Effect of TMF mixing on the structure of Al-3.5%Ni alloy refined with Al-Ti-B

Zaidat [59] has performed experiments on the effect of TMF mixing on the solidified structure of Al-3.5wt.%Ni binary alloy. Figure 1.21 shows the micro- and grain structure for non-mixed and mixed samples (10. 30 and 350 mT).

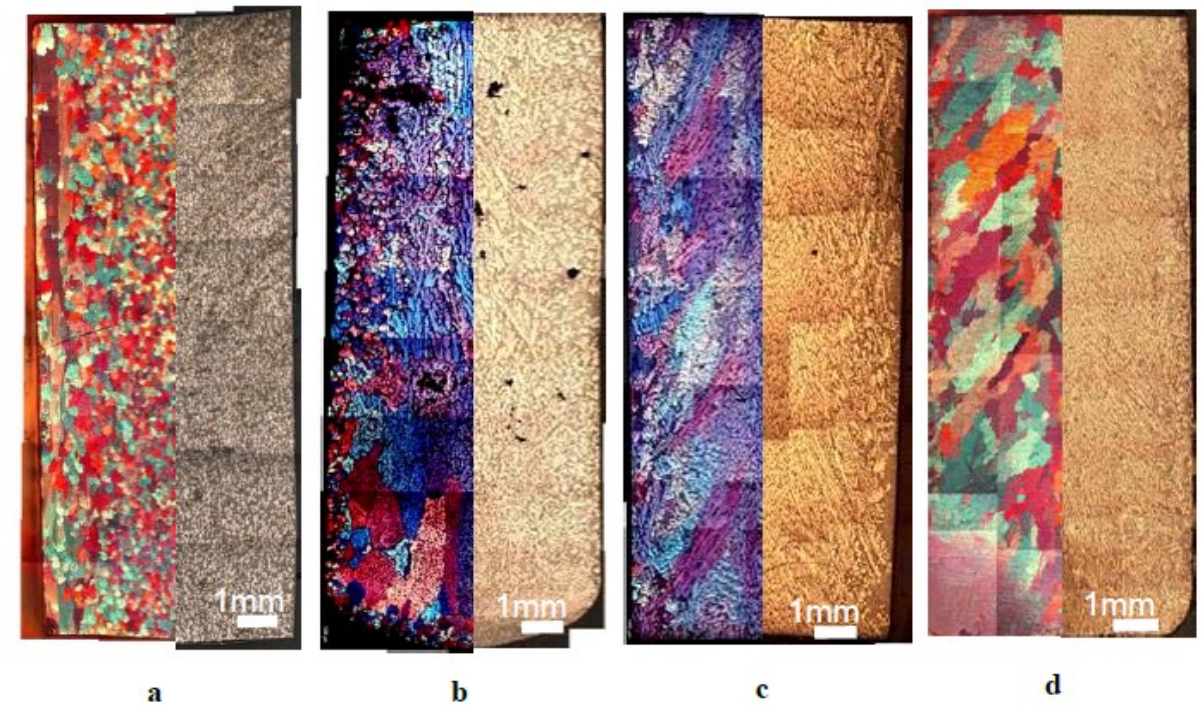

Figure 1.21 Effect of TMF mixing on the solidified grain- and microstructure. a) natural convection, b) 10 mT, c) 30 mT, d) 350 mT [59]

On 10 mT, the center of the part – which is not stirred directly by the magnetic field – stays columnar. On 30 and 350 mT, equiaxed structure develops and as the stirring becomes stronger, finer and more elongated grains are appearing.

1.4. Numerical macroscopic modelling for segregation in solidification of binary and multicomponent alloys

The macroscopic models for the solidification of the binary alloys are dated back to eighties of XX century. These models were developed on the basis of models for porous media, for two-phase flows and for mixtures, not reviewed here. The set of equations required to model the segregation at the macroscopic level includes transport equations: momentum equation, energy equation, transport of solute(s) are necessary. Some other equations (transport of solid grains, grain structures) are optional but they can help to mathematically represent the process closer to the real one. This system of transport equation is usually coupled with a "zero-dimension" (microscopic) solidification model. Here by "zero-dimension" we mean that such model is applied at each calculation cell, i.e. to a "point". It is customary to divide the solidification "zero-dimension" models on those which used equilibrium approach based on the lever or Scheil rule and those where a growth kinetic was introduced. These models are reviewed briefly in the chapter 3.1. Then, the macroscopic models coupled with equilibrium ones (reviewed in the chapter 3.1.1), in principle, allows one to obtain a qualitatively and even quantitatively correct macro-segregation pattern and channel/freckles formation provided good knowledge of the materials properties and experimental conditions. Their main advantage is much less requirement in the computational resources and better stability compared with the other approach. The approach where macroscopic equations are coupled with the microscopic models accounting for the kinetics (presented in the section 3.1.2), in principle, allows one to treat the columnar-to-equiaxed transition since difference in growth kinetics may appear between the columnar and equiaxed grains.

1.4.1. Microscopic models: equilibrium and kinetic approach in solidification of binary and multicomponent alloys

1.4.1.1 Equilibrium approach

Hereafter by "equilibrium" approach we name a calculation of the solid and liquid fractions and concentration in the solid and in the liquid at the microscale using the equilibrium phase diagram. As it was mentioned above, two general cases exist, in both, the diffusion in the liquid is supposed to be infinitely large, i.e. the concentration in the liquid becomes uniform instantly, and always equal to the liquidus concentration at a given temperature C_l. Consequently, there is no constitutional supercooling in the system. In both cases the relation between the concentration in the liquid C_l and concentration in the solid at the solid-liquid interface $\overline{C}_s$ are related through the partition coefficient k_p as $\overline{C}_s / C_l = k_p$.

Then a so-called lever rule supposes that the diffusion in the solid phase also occurs instantaneously, i.e. the concentration in the solid becomes equal to that at the interface. Then, introducing notions for the liquid and sold fractions f_l and f_s whose

sum is equal to unity and accounting for the conservation of the concentration, obtain the following system of equations:

$$f_l + f_s = 1 \tag{1.8}$$

$$C_l f_l + C_s f_s = C_0 \tag{1.9}$$

$$C_s / C_l = k_p \tag{1.10}$$

Solution of this system provides a relation between the liquid fraction and liquidus concentration:

$$C_l = \frac{C_0}{(1-k_p)f_l + k_p} \tag{1.11}$$

In solidification subjected to the Scheil rule, the diffusion process in the solid does not exist. The relation between the liquid fraction and liquidus concentration is:

$$C_l = C_0 f_l^{(k_p - 1)} \tag{1.12}$$

Equilibrium approach can be rather easily extended for the ternary and further to multicomponent alloys. A detailed mathematical description for a ternary alloy is given, for example, in [1]. In [3] the microsegregation in solidification of a ternary Al-Mg-Si system was considered and diffusion calculation was coupled with the calculation of the phase diagram in CALPHAD.

The macroscopic simulations for the ternary Al-7wt%Si-1wt%Fe alloy presented in the Thesis were made with such approach and the system of equations can be found in the chapter 3.

1.4.2. Models with the kinetic approach

One of the earliest publications which proposed a model for the solidification of an equiaxed grain accounting for the constitutional supercooling and finite diffusion in the liquid phase was the work of Rappaz and Thevoz (RT) [4]. For the better description of the solute concentration in the environment of the grain, two fluid phases were considered together with the solid. The three phases in such system are: solid, interdendritic liquid (hereinafter referred to as IDL) and extradendritic (bulk) liquid (hereinafter referred to as EDL). The model got the name from the envelope which is keeping the modelled grain (solid and IDL) together. Outside of the envelope, the bulk liquid exists. The shape of the envelope is a sphere of a radius R_g in the calculations, which connects the tips of the primary dendrite arms. The maximum radius of the grain is R_{tot}. There is no back diffusion in the solid (1), however complete mixing presents (infinitely fast diffusion) in the IDL (2), like in the Scheil model. Outside of the grain (3), pure diffusion occurs. In reality, the complete mixing zone smoothly fits of the dendrite and has a very complicated shape, which is replaced by a sphere. The envelope grows until it reaches the maximum possible radius R_{tot} while the solid grows from the IDL until

all liquid disappears. Figure 1.22 shows the distribution of the solute during growth as a function of the volume fraction – f_s for solid and f_g for the grain.

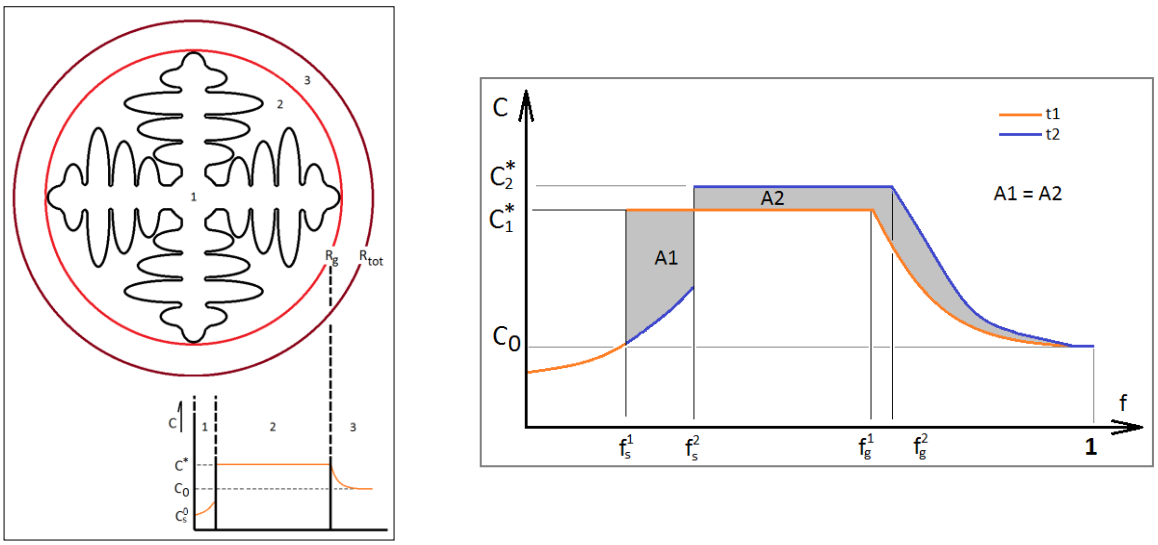

Figure 1.22 Visualizing the Envelope principle: Presentation of the equiaxed grain and schematic evolution of solute concentration during solidification from time t1 to t2 (A1 and A2 must be equal) – index 1 and 2 refers to t1 and t2 time-step

Since thermal diffusivity is more than 3 orders higher than the solute diffusivity, the temperature of the whole grain is equal to the dendrite tip temperature (T*). The curvature undercooling is supposed negligible under normal solidification conditions and, because of the size, the concentration in the IDL is supposed to be uniform and correspond to the liquidus concentration C^* which can be deduced from temperature. The diffusion in the EDL should be calculated with an appropriate boundary condition at the boundary of the grain for the concentration (a constant value or a zero diffusive flux). The grain growth occurs with a velocity quadratically proportional to the constitutional supercooling, i.e. to the difference between the C^* and the concentration at the boundary of the grain. Generally, one obtains a system of closed equations which can be solved and the evolution of the solid and grain fractions f_s and f_g , value of concentration in the IDL and in the solid, as well as of the concentration profile in the EDL.

It should be noted that ten years later Rappaz and Boettinger extended the approach of the equiaxed grain growth for multicomponent alloys with unequal liquid diffusion coefficients [5].

Soon after the RT model was presented, Wang and Beckermann [6] introduced the volume averaging formalization it model. Their envelope method was first presented for a one-grain or “zero-dimension” (0D) model which, according to authors, “can readily be incorporated into a maroscopic heat flow model”. Indeed, in the WB model the solute profile in the EDL was replaced with values of concentration averaged over the

extradendritic volume $\langle C_l \rangle^l$ and over the solid $\langle C_s \rangle^s$, and diffusion between the solid and IDL and between the IDL and EDL was related to the characteristic diffusion lengths l_{sd} and l_{ld}, respectively (Figure 2.2). Also, the inverse Ivantsov Function [49] was introduced in order to describe the envelope growth velocity. The composition within the dendritic zone supposed to be uniform and corresponds to the liquidus concentration. Yet, this model required calculations of the diffusion lengths, not known a priori, for which some proposals were made.

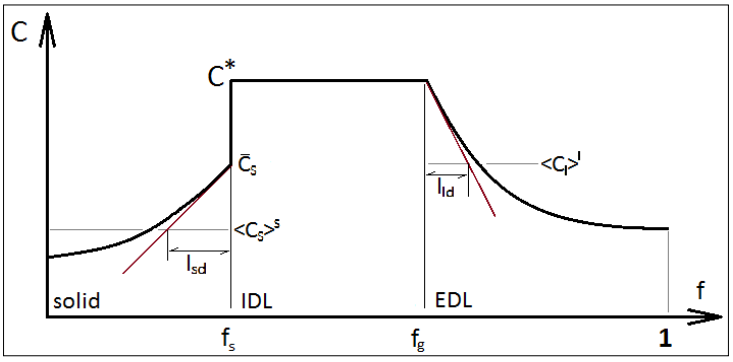

Figure 1.23 Solute balance in the model of Wang & Beckerman with the definition of the diffusion lengths in solid and extradendritic liquid

In further development of the model, Wang & Beckerman considered the case with a non-uniform concentration in the dendritic zone and introduced a shape factor for the envelope [WB2].

In the present work one part of the macroscopic simulations was made accounting for the solidification at the grain level based on the model formulated by Ciobanas and Fautrelle [8]. This model was developed using the approach of ensemble average initially employed for two-phase flows [9]. Generally, this approach has more solid physical background than the averaging over a volume since the latter, in fact, imposes rather strong restriction on the representative volume and requires uniform distribution of the properties (the elements) inside the volume. Yet, for many physical processes the resulting equations obtained with ensemble averaging are similar to those obtained with volume averaging. Similar to the model in [4] and [6], the model developed by Ciobanas and Fautrelle assumed an equiaxed dendrite growth represented by 3 phases: solid, interdendritic and extradendritic. The thermal equilibrirum between two phases was supposed and the liquid in the interdenritic zone was well-mixed with the concentration equal to the one on the liquidus line. In terms of equations, the main difference of the model from the one presented in [6] was in calculation of the diffusion length. The governing equations of the model are given in chapter 3 – in this section coupled with the macroscopic transport equations.

Among other works generally based on the model initially proposed in [4] for binary alloys are those developed by the team of research from University of Loeben, Austria, one can see [10] and references within.

Some other models which deserve attention but are not mentioned here are those with the idea to reproduce the shape of the dendrite grains in the final macroscopic pattern [11][12].

1.4.3. Macroscopic models with equilibrium approach for solidification of binary alloys with the thermosolutal convection.

A continuum model for momentum, heat and species transport in binary solid-liquid phase change systems was proposed by Bennon and Incropera [13][14] and obtained with the averaging of microscopic equation written for two phases over a representative volume. To close the system of the averaged equations, the solidification was described with the lever rule, yet, the system of transport equations was formulated for the mixture. The authors further applied the proposed model to solidification of an aqueous ammonium chloride solution in a rectangular cavity [14]. Later, S.D. Felicelli, J.C. Heinrichi and D.R. Poirier used another continuum approach with a stationary (columnar) solid phase and moving liquid and demonstrated a formation of the freckles in the solidification of binary alloys due to thermo-solute convection [15] and references within. A Scheil rule was used for the solidification part. A more detailed description of the equations and their mathematical statement is given below (chapter 3). This system of equations was used by other researchers [16] and quite recently was re-employed and proposed within the frame of a numerical benchmark for the solidification of the binary alloy SMACS (Numerical Simulation of MACrosegregation and Structure) [17][18] with either the lever rule or Scheil rule for description of solidification. Some results of the benchmark were summarized in [19]. One of the interesting results was that with both approaches for solidification the macrosegregation pattern in a totally solidified ingot was similar while differences were observed in the position and intensity of mesosegregation, i.e. in local channels/freckles. Further, using this system of equations, R. Boussaa et al. performed 3D simulation of a physical benchmark Afrodite on solidification of a Sn-3wt%Pb alloy under natural convection using the lever rule approach and obtained results in a good agreement with the experimental ones [21].

As far as multicomponent alloys are concerned, quite a few publications can be found with this approach, the most cited are [22], [23] and [24].

The number of publications related to the simulation of the solidification under the action of the external magnetic field is significantly less. Some of these publications took the equations based on the equilibrium approach while some others accounted for kinetic effects.

M. Medina et al. used the system of equations developed in [24] to study the effect of the travelling magnetic field on the segregation pattern in the solidification of binary alloys [25]. For the first time they revealed numerically appearance of the channels in the solidified ingots despite the idea of a well-mixed liquid due to the application of the electromagnetic stirring. Using similar model, Nikrityuk et al. predicted that rotating magnetic field (RMF) could provoke a radial segregation during solidification of binary alloys using the same system of equations with a lever rule for solidification [27]. After

observation of the strong radial segregation, another stirring mode with pulse sequences of a RMF stirring was realized for a small laboratory sample and numerically modelled and demonstrated a smoother segregation pattern. Finally, the work [28] combined the study of the solidification of ternary alloy under the action of the rotating magnetic field.

In the works mentioned above the electromagnetic stirring was introduced via a volume force whose spatial distribution was obtained either analytically or from some measurements performed on the experimental set-up using approach described in the 4.5.2. Consequently, variation of the force which could happen in the mushy zone, for example, because of the change in electrical conductivity due to phase change, was not considered. On the other hand, Poole [29] included in the numerical model calculation of the electromagnetic field coupled with the solidification model. Yet, the latter was based on the mixture model [13], the electric conductivity was similar for the solid and the liquid phase and the frequency of the electromagnetic field was chosen quite high (~4900Hz), i.e. more appropriate for the heating than for the effective stirring.

1.4.4. Macroscopic models for simulation of the segregation accounting for the kinetics of solidification

There are numerous applications of the macroscopic models which accounts for the diffusionally governed dendrite growth to the simulation of solidification processes under thermo-solute convection. The works were presented by Ni and Beckermann for the multicomponent two-phase system [20] and by Wang and Beckermann for binary two-phase systems [38]-[40]. Among other works, one can find already mentioned work [WL_2010] and more recent publications of these authors [42], [43]. Actually the Web of Science reports about more than 300 publications with a subject related to the combination of words «macrosegregation», «convection », «modeling or simulation» excluding « fragmentation » « slag » and « phase-field » with a constantly increasing number of publications. Of course, this number of publications includes those based on the equilibrium approach.

Yet, very few publications were devoted to the modeling of the solidification with the electromagnetic stirring coupled with diffusionally governed dendrite growth. Actually, almost all such studied were performed in Grenoble. The two-dimensional axisymmetric simulations of Budenkova et al. [44] based on the multiphase statistical averaging model which accounted for the kinetic effects [8] for the solidification confirmed the predictions made in [27] and qualitatively explained the experimental results observed in solidification under the RMF in [45]. Further, a publication of Noeppel et al. [46] using the statistical averaging model [8] demonstrated the effect of the secondary arm spacing on the convection and segregation in the mushy zone via permeability of the latter for the free and forced convection caused both by RMF and TMF. This work explained the segregation pattern observed in [30] in the solidification of the AlNi alloy.

1.5. Theory of the electromagnetism in application to the elaboration of alloys

The use of the external alternating electromagnetic field in the elaboration of alloys is related to the induction phenomena. When an electrically conducting material is subjected to the external AC magnetic field, the induced electric current (eddy currents) arises in the conductor. Further, because of the interaction of the electric current and the magnetic field inside the conductor a Lorentz force $\overrightarrow{\mathrm{F_L}}(\mathrm{x,y,z})$ appears and may affect the motion of the conductor. In the case of liquid metals, the spatial distribution of the Lorentz force may lead to the deformation of the free surface of the liquid or to the generation of the stirring inside the liquid volume. The resulting effect of the application of the AC electromagnetic field depends both on the characteristics of the field (frequency, phases, geometry of the inductor) and on the properties of the materials (electrical conductivity, viscosity, volume configuration). The system of equations which allows one to solve the coupled electromagnetic and hydrodynamic problem includes the Maxwell equations and Naviers-Stokes equations given below.

The system of Maxwell equations includes

The equation which states the absence of the magnetic monopoles (”magnetic charges”)

$$\vec{\nabla}\vec{B} = 0 \tag{1.13}$$

Further, the Lentz law demonstrating that the electric field is originated with variable magnetic fields:

$$\vec{\nabla} \times \vec{E} = \frac{\partial \vec{B}}{\partial t} \tag{1.14}$$

The Ampere law which relates the circulating current $\vec{j}$ and magnetic field $\vec{B}$ (with the displacement current neglected)

$$\vec{\nabla} X \vec{B} = \mu_0 \vec{j} \tag{1.15}$$

with current conservation law:

$$\vec{\nabla}\vec{j} = 0 \tag{1.16}$$

and the Ohm’s law

$$\vec{J} = \sigma\left(\vec{E} + \vec{u} \times \vec{B}\right) \tag{1.17}$$

Where $\vec{u}$ is the velocity vector and σ is the electric conductivity of the material. To solve the electromagnetic equation a so-called vector potential $\vec{A}$ such that $\vec{\nabla} \times \vec{A} = \vec{B}$ is used. Then, the eq. (1.13) is fulfilled automatically. It should be noted also that the same magnetic field is defined by the vector $\vec{A}$ and the vector $\vec{A}' = \vec{A} + \vec{\nabla}\emptyset$, $\emptyset$ is any differentiable function since $\vec{\nabla} \times \vec{A} = \vec{\nabla} \times (\vec{A} \times \vec{\nabla}\emptyset)$. With use of the vector potential $\vec{A}$, the Ohm’s equation can be also presented in the form

$$\vec{j} = \sigma(-\frac{\partial \vec{A}}{\partial t} + \vec{\nabla}\emptyset + \vec{u} \times \vec{B}) \quad (1.18)$$

Rather often it is convenient to get rid of the electric current from the eqs.3-5 and to get the equation for the magnetic field $\vec{B}$ and the vector potential $\vec{A}$:

$$\frac{\partial \vec{B}}{\partial t} = \frac{1}{\mu\sigma}\vec{\nabla}^2\vec{B} + \vec{\nabla} \times (\vec{u} \times \vec{B}) \quad (1.19)$$

$$\frac{\partial \vec{A}}{\partial t} = \frac{1}{\mu\sigma}\vec{\nabla}^2\vec{A} + \vec{u} \times \vec{B} + \vec{\nabla}\emptyset \quad (1.20)$$

In obtaining last equation the vectorial identity $\vec{\nabla} \times (\vec{\nabla} \times \vec{\mathrm{P}}) = \vec{\nabla}(\vec{\nabla} \cdot \vec{\mathrm{P}})$, with $\vec{\mathrm{P}}$ for any vector was used, and a generally employed condition $\vec{\nabla} \cdot \mathrm{A}$ was applied.

The Maxwell equations should be coupled with hydrodynamic equations, which for the incompressible pure fluids are written as follows:

$$\vec{\nabla}\vec{u} = 0 \quad (1.21)$$

$$\rho\frac{\partial \vec{V}}{\partial t} + \rho(\vec{V}, \nabla)\vec{V} = \rho\vec{g} - \nabla P + \vec{j} \times \vec{B} + v\vec{\nabla}^2\vec{V} \quad (1.22)$$

Also, an additional term related to the resistive Ohm's heating, generally, should appear in the energy equation $q_{ohm} = \vec{j}^2/\sigma$. However, with the typical intensity and frequencies of the AC current used to create the stirring in liquid metals the value of this term is negligible.

In practice to generate the stirring of the liquid metal, mainly two types of the AC magnetic fields are used that are traveling and rotation magnetic field presented below.

1.5.1. Traveling magnetic field

The AC monophase electromagnetic systems are widely employed in metallurgical industry, yet they are mostly aimed at the inductive heating while traveling magnetic field allows one to create various regimes for the stirring. A traveling AC magnetic field is generally realised with polyphase inductors as shown in the Figure 1.24. In such configuration each coil in the system is alimented with an external current of the density j_0 and the frequency $\omega = 2\pi f$ in a way to have a phase shift φ with respect to the previous coil. Using rough approximation, one can think that at each instant the magnetic field lines are closed and have form of tors which are displaced in z-direction.

In a general case, the instant value of the electric current supplied to each coil is given as

$$j_{ex,\theta} = j_0\, cos(\omega t - kz) = Re\{j_0 e^{i(\omega t - kz)}\} \quad (1.23)$$

where *Re* is for the real part of the imaginary number and *i* is the imaginary unit $i^2 = -1$. Consequently, magnetic field induced by this current can be considered as a longitudinal wave of the length λ moving along the sample with the velocity U_s:

$$U_s = f\lambda = \frac{\omega}{k} \qquad (1.24)$$

known also as synchronism velocity, for which $k = 2\pi/\lambda$ is a wave number-vector. It should be stressed out that the geometry of the coils, namely their size and winding density, defines the length λ.

A polar step $\tau = \lambda/2 = \pi/k$ is often used in practice to characterize the coil.

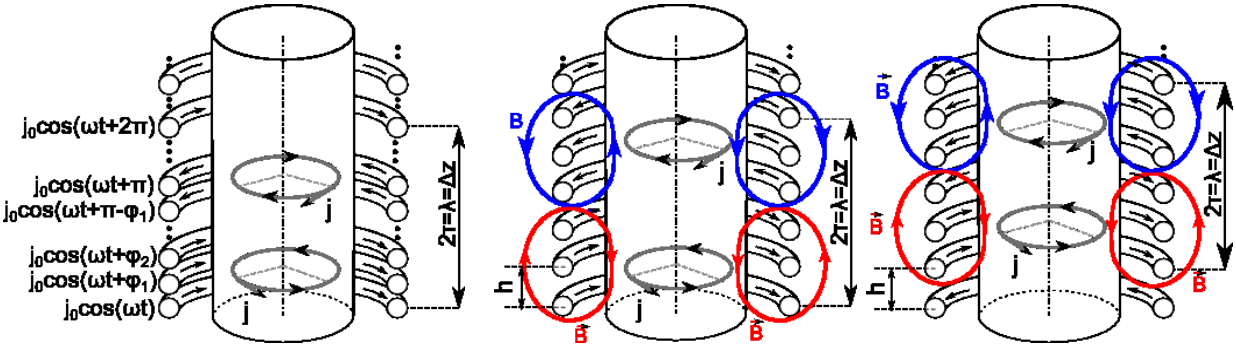

Figure 1.24 A scheme for a polyphase travelling magnetic field

1.5.2. Skin depth

Suppose that outside the sample at its surface ($r = R$) the amplitude of the magnetic field created by the current $j_{ex,\theta}$ is B_0. Then it can be demonstrated that inside the charge the amplitude of the magnetic field decreases toward the center of the sample as $e^{(r-R)/\delta_e}$ where

$$\delta_e^{-1} = Re\left\{\sqrt{k^2 + i\mu\sigma\omega G}\right\} = Re\left\{\sqrt{\frac{\pi}{\tau} + i\mu\sigma\omega G}\right\} \qquad (1.25)$$

is termed *effective skin depth* and $G = (1 - u_\theta \cdot r)$ is a so-called slide parameter. The latter is close to one if the forced velocity of liquid is weak with respect to U_s and tends to zero if these velocities tends to be equal. This parameter is discussed below in the text, yet we should mention here that for most of the calculations presented in the thesis the value of $G \approx 1$.

The skin depth shows that for the high frequencies the magnetic field will be mostly concentrated in a thin layer along the lateral side of the charge. On the contrary, with lower frequency the penetration, of the magnetic field inside the charge is deeper.

1.5.2.1 Polar step

It is important to note that in the case of polyphase AC electromagnetic field the skin depth depends on the polar step τ and that with a smaller polar step the penetration of the magnetic field in the sample is weaker.

1.5.3. Distribution of the Lorentz force in the sample for TMF case

In the presented axially symmetric system the instantaneous magnetic field inside the charge has two components, both with the frequency of the supplied current. If the helicity of the coil winding and the effects related to the finite height of the inductor or of the sample are neglected, the instantaneous eddy current has only the azimuthal component which has the same frequency as the external supplied current:

$$\vec{B} = (B_r, 0, B_z) \qquad \vec{j} = (0, j_\emptyset, 0)$$

Consequently, the instantaneous Lorentz force also has a radial and an axial component:

$$\vec{F}_L = \vec{j} \times \vec{B} = (F_r, 0, F_z)$$

Since the oscillation period of the Lorentz force is very short compared to the characteristic time of the fluid flow, the force averaged over several periods is introduced into the Navier-Stokes equation. The average force generally also has radial and axial components and is proportional to the AC frequency ω. For the infinitely long inductor or the charge, the radial component of the force is irrotational, i.e. it creates oscillation of the pressure inside the liquid but do not initiate the motion while the axial component of the Lorentz force is directly responsible for the liquid motions.

Generally, for a particular inductor with its proper power supply the distribution of the Lorentz force inside the charge can be calculated numerically.

Yet, if the end effects are neglected, that is for an ideal case of an infinite inductor and the charge, the driving axial force can be presented in the form:

$$\langle \vec{F}_{L,TMF} \rangle = \frac{1}{2} \sigma \omega B_0^2 \frac{k}{|\delta|^2} \left| \frac{sh(\delta r)}{ch(\delta r)} \right|^2 G \vec{e}_z$$

Similarly, in the case of planar geometry (two-dimensional, Figure 1.24) the average Lorentz force has a component directed perpendicularly to the planes containing the coils and a component directed along the charge. In a real situation because of the end effects both components actually create motion of the liquid, yet if the end effects are neglected, only the vertical component of the force initiate convection in the liquid.

An advantage of the use of two (or more) set of coils instead of a helicoidal inductor is that the phase shift can be done in a more sophisticated way, for example, the magnetic wave on the left ($x < 0$) and on the right ($x > 0$) side can propagate in opposite directions thus creating another motion in the liquid.

1.5.4. Rotating magnetic field

A rotating magnetic field can be considered as an AC polyphase coil being rolled. A realization of a polyphase scheme with 3 phases is shown in Figure 1.25 from where it is seen that variation of the magnetic field created by the AC current is equivalent to the

field of a magnet which would rotate in the plane (*x,y*) and generally would have mainly a radial and an angular component, similar to the case of the TMF.

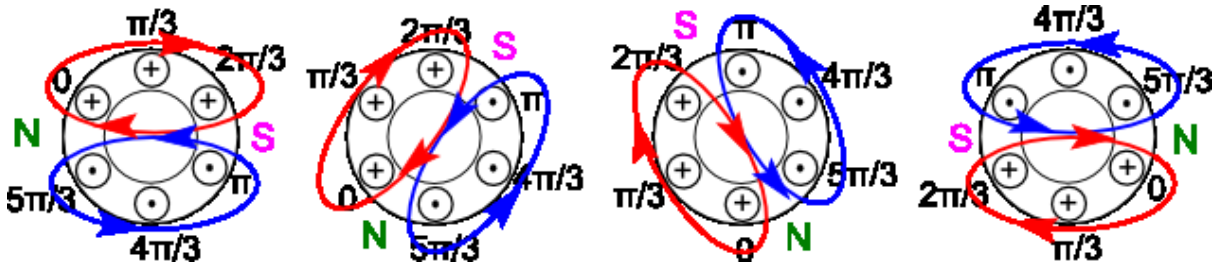

Figure 1.25 A scheme for a polyphase rotating magnetic field

The eddy current created by such magnetic field is moving along the sample, that is it has only the z-component while its phases are dependent on the azimuthal angle theta. The angular wavelength is defined by the number of poles pairs *p* as

$$\lambda_\theta = \frac{2\pi}{p}$$

Then, the instant current supplied to each coil along the *z*-axis is

$$j_{ex,z} = j_0 \cos(\omega t - p\theta)$$

The "tores" of the magnetic lines rotate around the charge as shown in fig.2. At each instant, the magnetic field has radial and azimuthal component:

$$\vec{B}_{rmf} = (B_r, B_\theta, 0) \qquad \vec{j}_{rmf} = (0,0,j_z)$$

Consequently, the instantaneous Lorentz force also has azimuthal and radial components:

$$\vec{F}_{L,rmf} = \vec{j}_{rmf} \times \vec{B}_{rmf} = (F_r, F_\theta, 0)$$

Yet, after time averaging procedure, only the azimuthal component of the force will remain. In many practical cases the average Lorentz force acting inside an electrically conductive volume can be approximated as

$$\langle \vec{F}_{L,rmf} \rangle = \frac{1}{8}\sigma\omega B_0^2 \psi(z) \Phi(\frac{r}{R}) G$$

where $G = (1 - u_\theta \cdot r)$ is again a slide parameter accounting for the effect of the fluid flow on the magnetic field, with u_θ being the azimuthal component of the velocity field in the liquid and *r* a radial coordinate in the cylindrical coordinate system.

The function $\psi(z)$ considers the variation of the axial magnetic field because of the size of the inductor while $\Phi(r/R)$ depends on the penetration of the magnetic field into the charge which is characterized by the *skin depth*:

$$\delta = \left(\frac{2}{\mu\sigma\omega G}\right)^{1/2} \qquad (1.26)$$

If $\delta >> R$, then

$$\Phi\left(\frac{r}{R}\right) = \left(\frac{B_0 R}{p}\right)^2 \left(\frac{r}{R}\right)^{2p}$$

1.6. Conclusions on chapter 1

Seeing the results of electromagnetic stirring on the solidified metallic structure it is clear, that deeper investigation of the solidification processes is needed to be able to control industrial cases and achieve the desired characteristics of the part. The solute distribution cannot be predicted in many case; therefore, the simulation can be a useful tool, however the coupling between electromagnetic simulations and solidification models is a great challenge. The Lorenz force field induced by rotating magnetic field is described with an analytic equation, on the other hand TMF can be more complex. The solution of such a case will be presented in chapter 4.5.

The solidifications simulations were performed using Lever rule and Envelope method for binary alloys. In the next chapters, we will follow this approach and extend it to simulations of ternary alloys under TMF forces.

2. Chapter:
Experimental installation constructed in Miskolc University

2.1. Introduction of chapter 2

The MTA-ME Materials Science Research Group is working with solidification processes since the early 2000s – and some members many since years before. The main aim is to see the effect of melt flow on the solidified metallic structures in all scales. The group has joined the ESA funded MICAST project in 2000. The RMF and TMF solidification facilities were designed and constructed in the framework of the mentioned project.

In case of TMF, the structure of the inductor has an innovative design resulting in 5 different mixing directions and with magnetic field equally penetrating in the complete sample.

During the past 18 years, several new materials micro- and macrostructures were found – e.g.: Al, Sn Pb or Cd based binary and ternary alloy. The strong forced convection leaved its footprint inside the material as driving the solute into special forms. The primary and the secondary dendrite arm spacing is affected also.

The facilities and the effect of mixing on the temperature and solute distribution in the sample, are presented in this chapter.

2.2. The solidification facilities

The experimental basis of my work was the two solidification facilities designed at the MTA-ME Materials Science Research group on the University of Miskolc. The facilities are modified Vertical Bridgman furnaces equipped with electromagnetic stirrers – using rotating- and travelling magnetic field. These machines were designed to investigate the effect of various flow fields on the solidified structure of Al-based binary and ternary alloys. The sketches of these can be seen below.

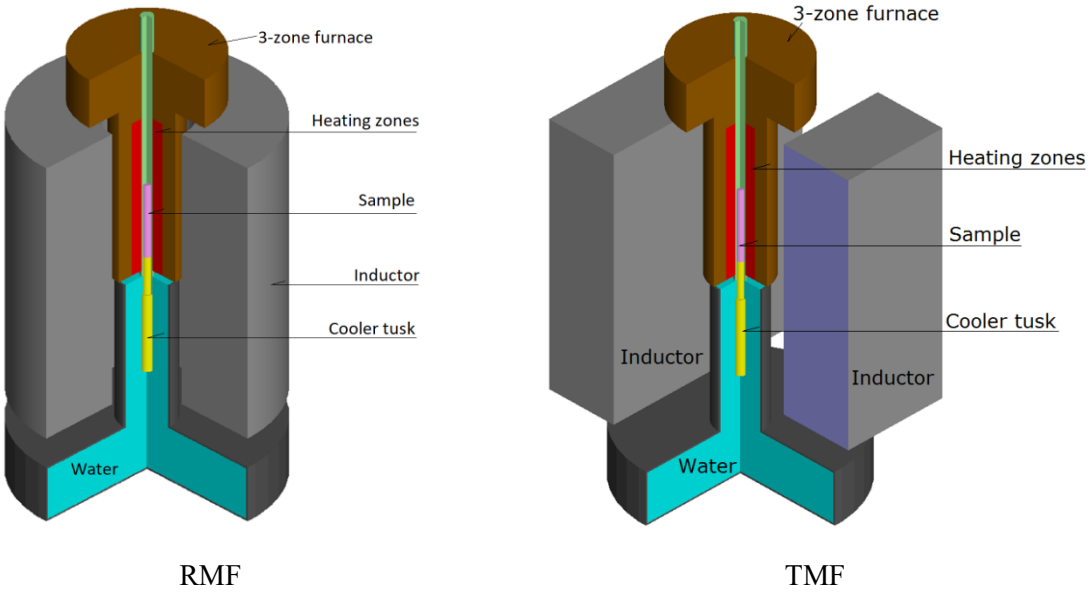

RMF TMF

Figure 2.1 Sketch of the solidification facilities

The sample is placed into the centerline of the furnaces – and due to the design – also in the center of the inductors. The molten metal requires a special holding system to keep it in the correct position during the experiments. The following assembly is used in both cases:

Figure 2.2 The sample and the ceramic crucible

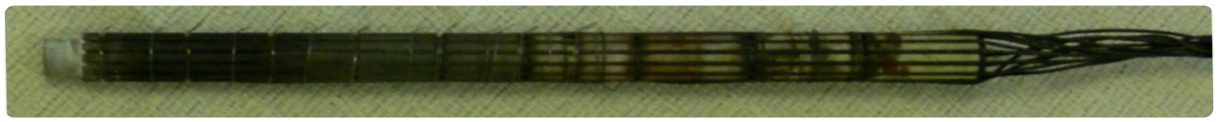

Figure 2.3 Thermocouples applied on the crucible

Figure 2.4 The complete sample holder assembly

The prepared solid alloy is placed into the two-piece ceramic crucible, which has 13 grooves. Those are used for the thermocouples to monitor the temperature field during the whole experiment. For the control of the heat extraction during the experiment, a copper cooler tusk is attached to the bottom of the crucible with heat conductive paste between each. The crucible is closed with a silicon glass.

2.2.1. RMF

The sample is placed into the centerline of the furnace (which is also in the center of the RMF inductor) which can be melted inside without any other equipment. During the experiment, the sample is lowered into the cooling water. According to the alloy composition, the flow strength and the thermal gradient, several different and yet unseen material structures can be achieved – like presented in chapter 1.3.

The magnetic field distribution was measured by A. Rónaföldi [51]. The inductor is designed to provide constant induction in the volume, where the sample is placed. The radial and longitudinal distribution is presented on Figure 2.5.

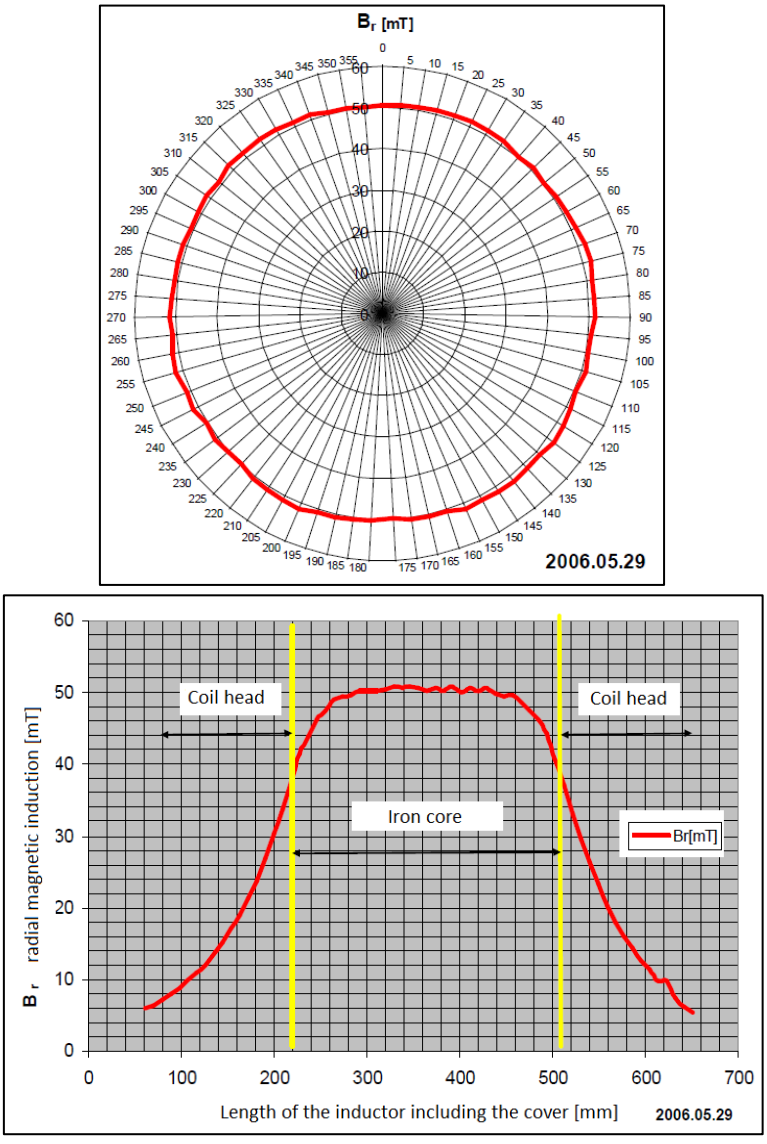

Figure 2.5 Radial and longitudinal distribution of B_r [mT]

2.2.2. TMF

As could be seen of Figure 2.1, the main structure of the facility is the same as in case of RMF, only the inductor is replaced with a twin-head travelling magnetic field inductor. Since the exact technical parameters of the inductor were not shared, simulations were made using Comsol Multiphysics and Ansys Fluent to obtain similar magnetic field as the experimental ones. The work will be presented in chapter 4.5. A special thermal effect appearing in the system was used for indirect validation of the Comsol results.

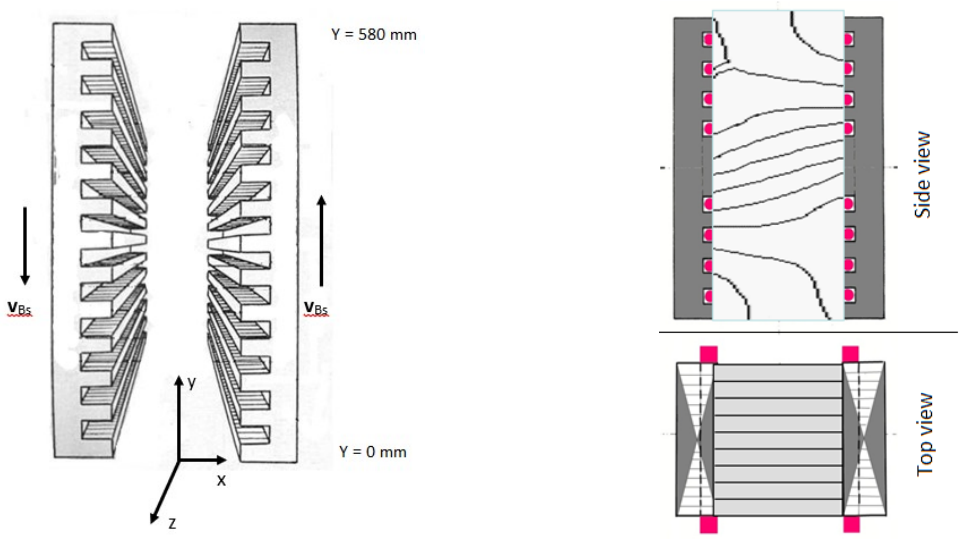

Figure 2.6 Sketch of the TMF inductor and sketch of the magnetic fluxes in case of bidirectional stirring

The two sides can be controlled separately resulting in 5 different Lorenz force field configurations. If the magnetic field is controlled to be vertical (“X”) in the air gap, an upward Lorenz force appears. If B horizontal (“Y”) in the air gap, a downward Lorenz force field appears.

The combination of the two results in a bidirectional Lorenz force field. These two force fields can also move upwards and downwards. In the third case (“XY”), one side of the melt is pushed upwards and the other downwards.

As a summary, the 5 configurations are:

1. Vertical magnetic field, upward Lorenz force moving upwards
2. Vertical magnetic field, upward Lorenz force moving downwards
3. Horizontal magnetic field, downward Lorenz force moving upwards
4. Horizontal magnetic field, downward Lorenz force moving downwards
5. Combination of the horizontal and vertical magnetic field, bidirectional Lorenz force

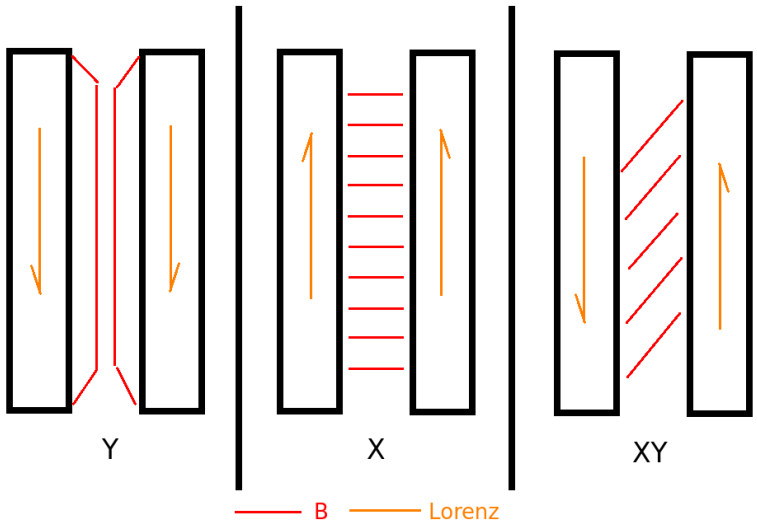

Figure 2.7 Magnetic flux and induced Lorenz force combinations of the twin head inductor

The magnetic field components were measured between the inductor heads by Dr. Arnold Rónaföldi. This could be used for validation purposes in later simulations for acquiring the correct Lorenz force field. The air gap between the two heads is 130 mm. The magnetic field is equal in front of both sides – 10 mm far from the heads. The total height of the inductor is 580 mm with the pole pitch of 290 mm. The synchronous velocity is 29 m/s, since the frequency is 50 Hz. The magnetic field components (except component z ~ 0) and the resulting B are shown on the diagrams below for different field strengths – measured only for the position of the sample.

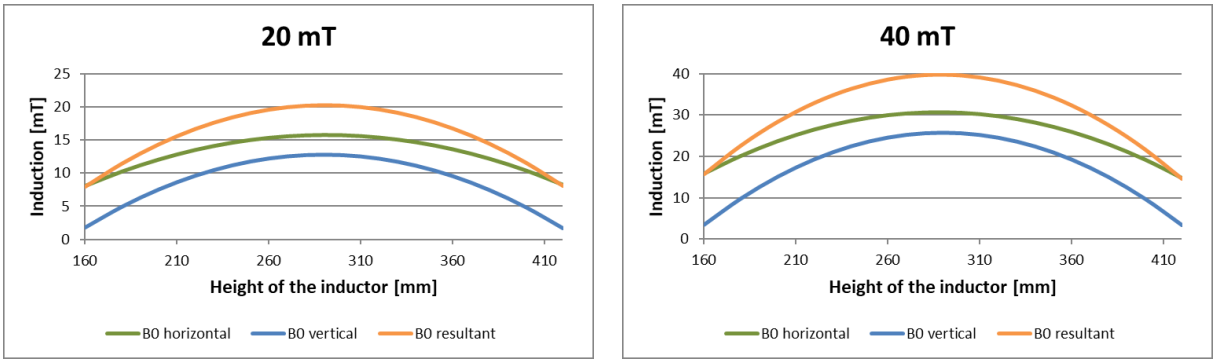

Figure 2.8 Measured magnetic field strength in the inductor – on the area of the sample

2.3. Experimental results of Miskolc

The presented experimental results are used later in the thesis as reference and / or validation values. The measurements were performed and published by other associates of the research group. The results were transferred for free usage in the simulations.

2.3.1. RMF experiment

In 2007 Kovács et al. performed experiments on Al-7Si-0.6Mg alloy using various magnetic field intensities. For the thesis project 20 mT magnetic induction was chosen based on the experience coming from the pure flow simulations. Such induction results in a flow of transient zone regarding turbulence. The used solidification model is designed for laminar flow, but a more intense test was in interest. The sample was provided using 99,99% base materials and cut into 8 mm mean diameter and 100 mm length. The following technical parameters were used:

- B_r magnetic induction 20 mT
- f frequency 50 Hz
- $F_{L\text{-}max}$ maximal Lorenz force 965 N/m^3
- v_{sample} sample lowering velocity 0.1 mm/s
- G thermal gradient 8 K/mm

During the experiment, the temperature data of the 13 thermocouples were collected and saved. It will be used as a boundary condition in the simulations. The plot of the dataset can be seen below.

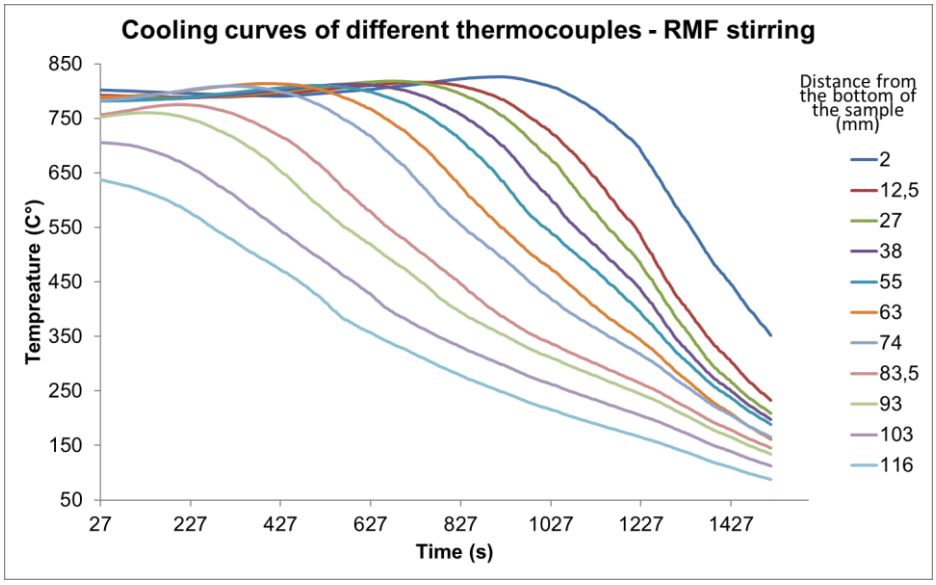

Figure 2.9 Temperature dataset of the experiment

The samples were cut into 4 equal pieces having length about 20 mm and the all sections were cut into half along their axis. The 4 longitudinal sections were grinded, polished and etched in 0,5% water solution of HF. Cross section specimens were also made with the same metallographic method. The macrostructure of the samples can be seen on Figure 2.10.

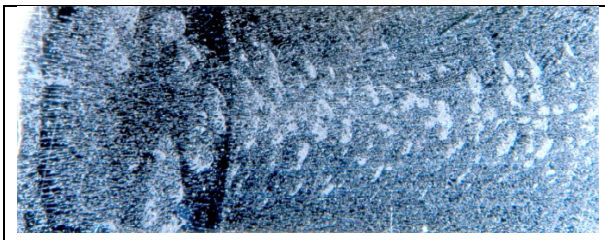

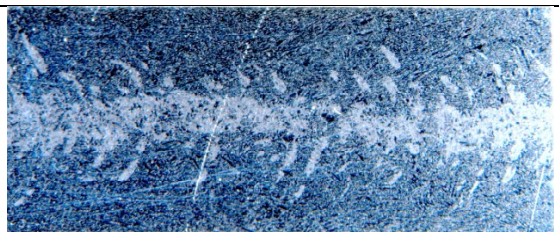

Bottom–middle part – direction of solidification →

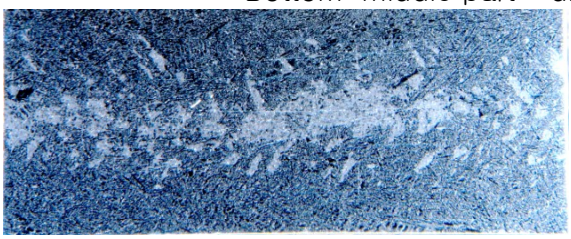

Middle–top part – direction of solidification →

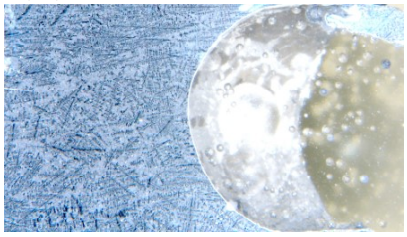

Top of the sample – direction of solidification →

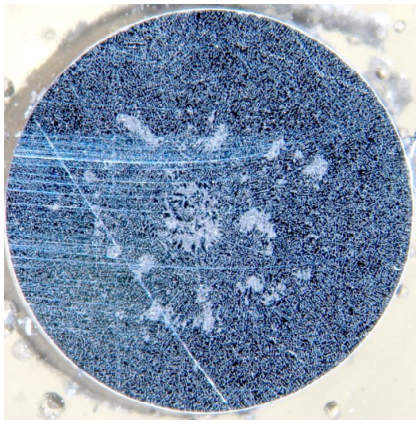

First cross section

Second cross section

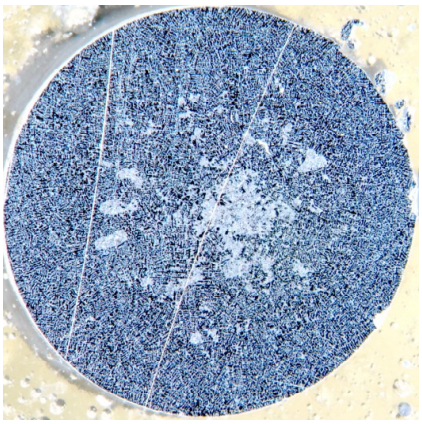

Third cross section

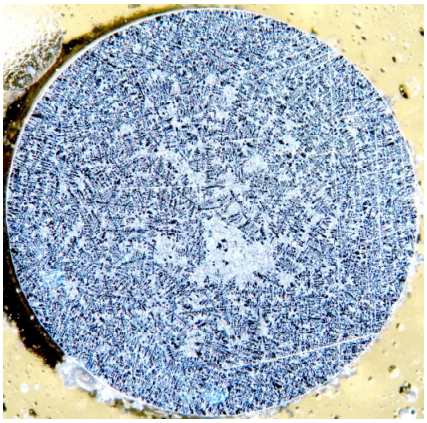

Fourth cross section

Figure 2.10 The resulting macrostructure

The concentration distribution was also measured by Kovács et al. The result can be seen on the diagram below, but it is not showing clear enough the expected effects

based on the etched samples. Therefore, a repetition of the measurement was essential with the aim of higher accuracy, since the currently available measurement devices have significantly better resolution. Moreover, the simulation results have helped in the design of the new measurement method.

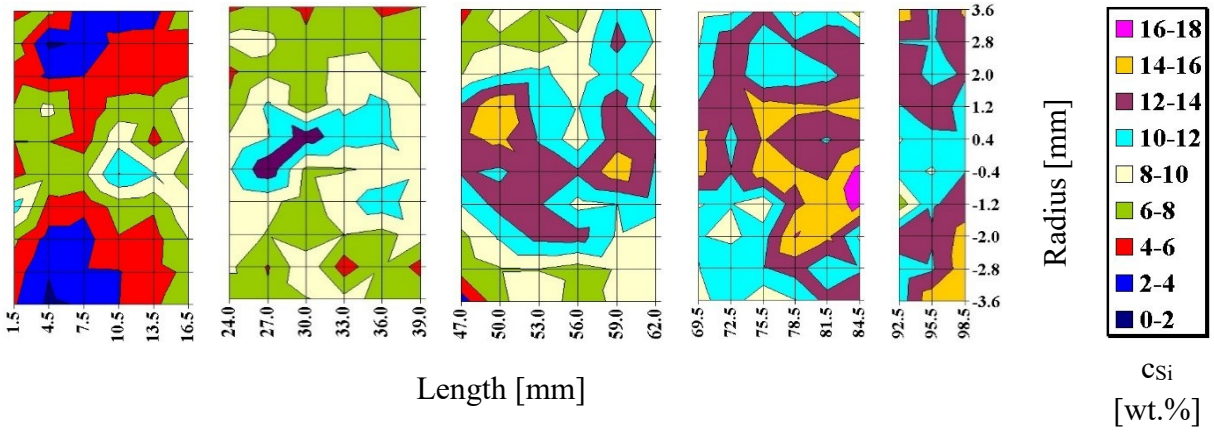

Figure 2.11 Concentration distribution measured by Jenő Kovács

The concentration distribution of 20 mT RMF sample was done on 3 longitudinal sections: 0-19 mm, 25-45 mm and 50-70 mm using the Edax EDS microprobe of a Zeiss electron microscope. A measuring window of 0.8 x 1 mm was chosen. Using this window, the whole sections could be mapped – 10 images across the diameter times 20 across the height. The first window was adjusted “by hand” to the proper position and then the automatic mechanism of the table was used to map the whole sample. The complete window area was measured so the values should be used as averages of an area of 0.8 x 1 mm.

Due to the morphology of silicon, the X-ray spectra had to be compensated. For that the cross section of an unmixed sample was used. The concentration has been measured and the resulting peaks were indicated as 7% Si and 93% Al.

The samples are a bit conical, so the last images do not completely cover the window, but it doesn’t affect the accuracy of the measurement.

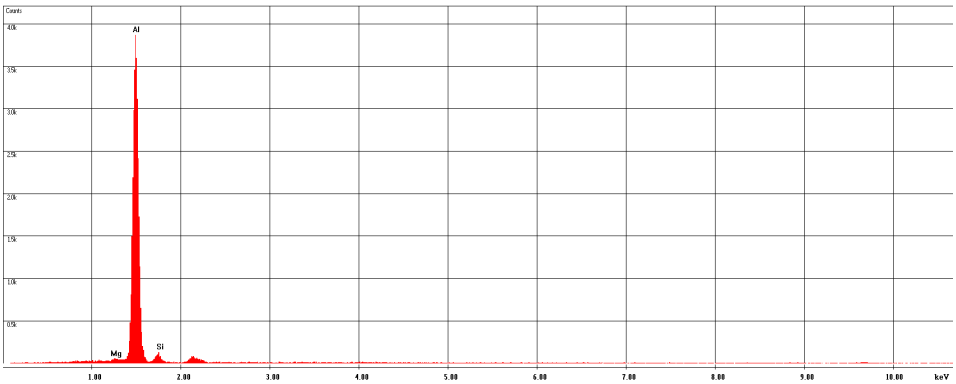

Figure 2.12 Sample spectrum of the measurement series

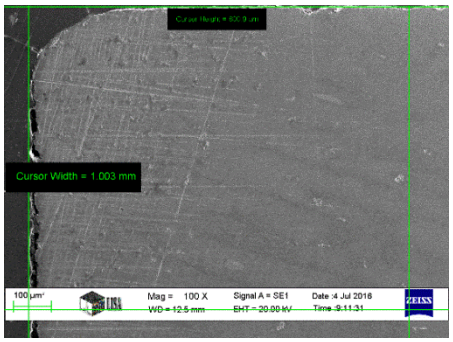

First window adjusted

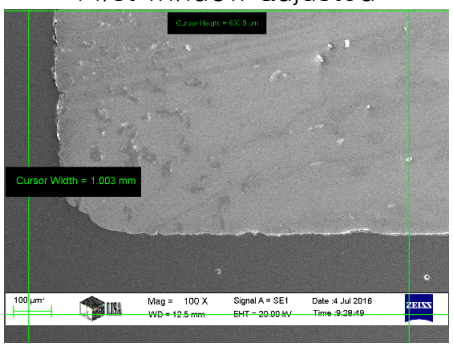

Last window of the first column

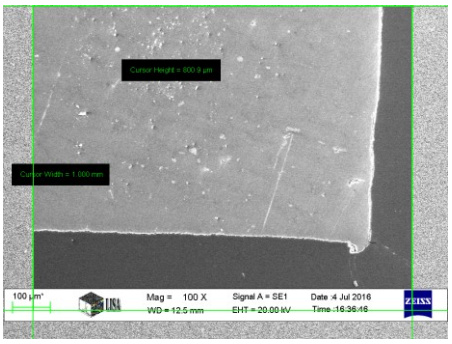

Last window of the measurement

Figure 2.13 Measuring windows

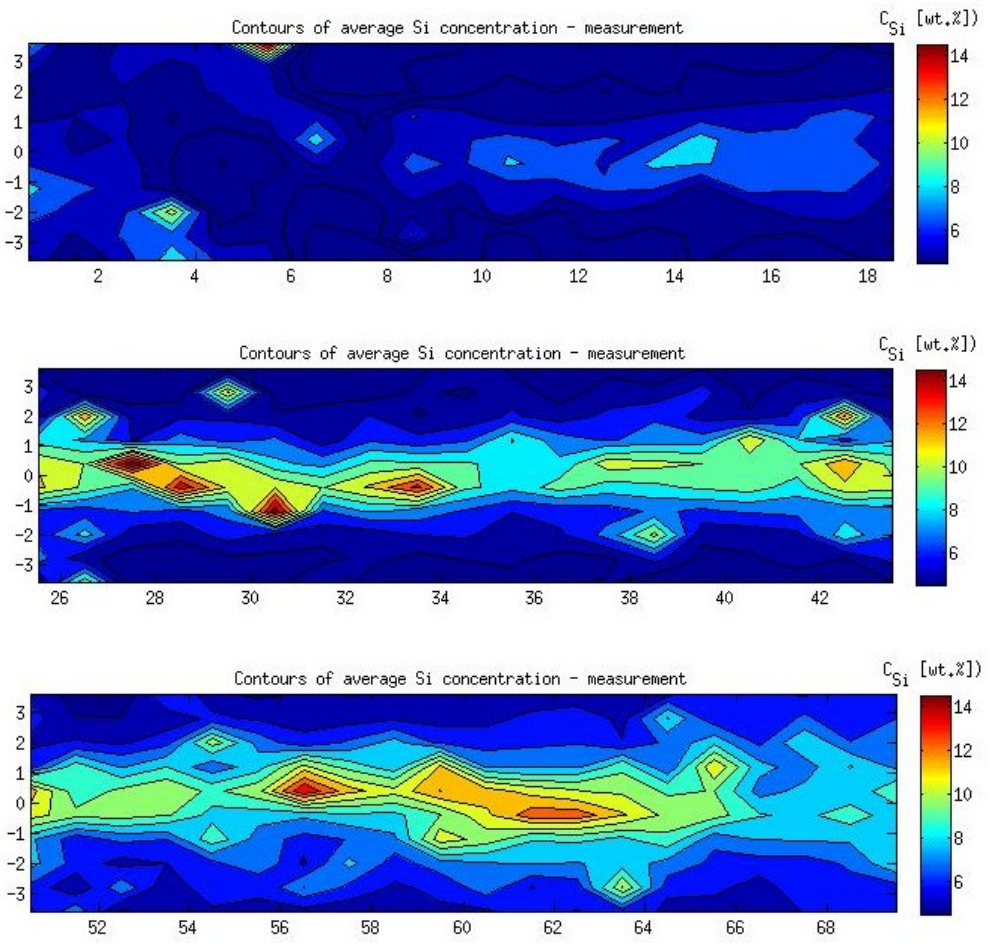

Figure 2.14 Contour plot of measurements

2.3.2. TMF experiments

2.3.2.1 Thermal effect in TMF

During the first experiments (performed by Arnold Rónaföldi) using the TMF facility, a yet unknown thermal effect occurred. The phenomenon is appearing the strongest way in case of the "XY" field configuration, when one side of the melt is pushed upward, the other one is pushed downwards. All the experiments start with an isothermal holding state when only the technical thermal gradient is set up and no lowering of the sample or mixing is used. The simple aim of this is to melt everything completely and have a complete thermal equilibrium in the system – Figure 2.15.

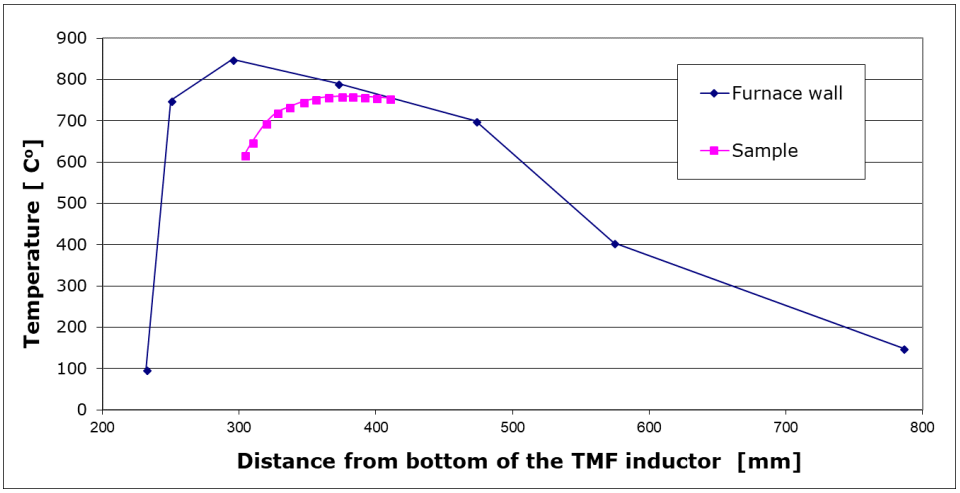

Figure 2.15 Temperature distribution in the system without stirring

Regardless if there is sample lowering or not, at the moment of switching the stirring on, the thermal gradient crashes and a new one appears – Figure 2.16.

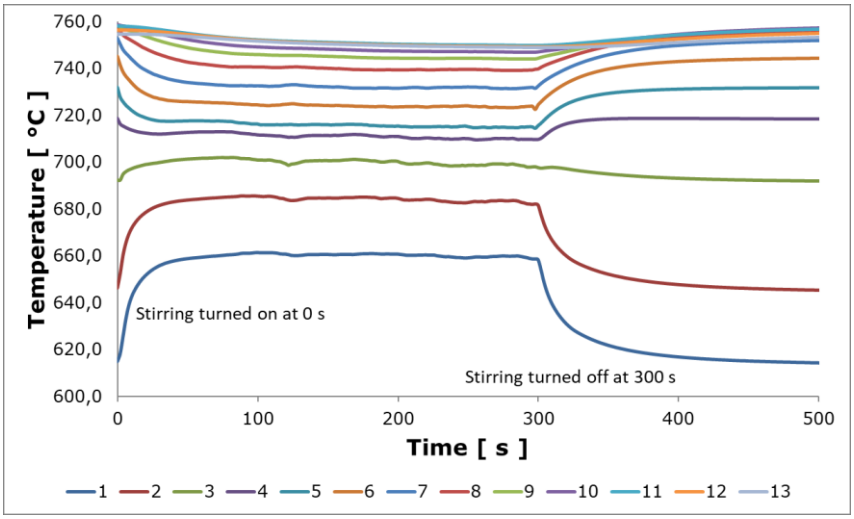

Figure 2.16 Effect of 40 mT stirring (up-n-down) on the temperature distribution in the sample. No. 1 is the lowest thermocouple. 0-300 s stirred, 300-500 sec not stirred.

The experiment was performed for 5. 10, 20 & 40 mT, but 40 mT is the most spectacular one.

2.3.2.2 TMF experiments on solidification

A series of experiments were performed using the new TMF inductor – by A. Roósz, A. Rónaföldi and A. Jenő. The key force field is the "bi-directional" which is pushing the melt's two side upward and downward, since this is provides the strongest and most directed Lorenz force field. Al7Si1Fe alloy was used for the experiments on various inductions: 0, 20, 40, 80. For the current research, the 20 mT was chosen, since its flow field was validated via the thermal effect which was presented in chapter 2.3.2 and it is laminar (the current solidification solvers are not tested on turbulent flow). The main technical parameters were:

- Sample lowering velocity v_{sample} 0,05 m/s
- Thermal gradient G 5 K/mm
- Frequency f 50 Hz
- Magnetic induction B_0 20 mT
- TMF form XY bidirectional

The concentration distribution was measured with image analysis method. A mosaic image was provided of a cross section of the sample and two different areas were chosen – Figure 2.17. The left are shows higher Si content based on eutectic fraction. Such fraction was measured on the image and the Si content was calculated based on the phase diagram. The result of the two blue areas are presented in Table 2.1.

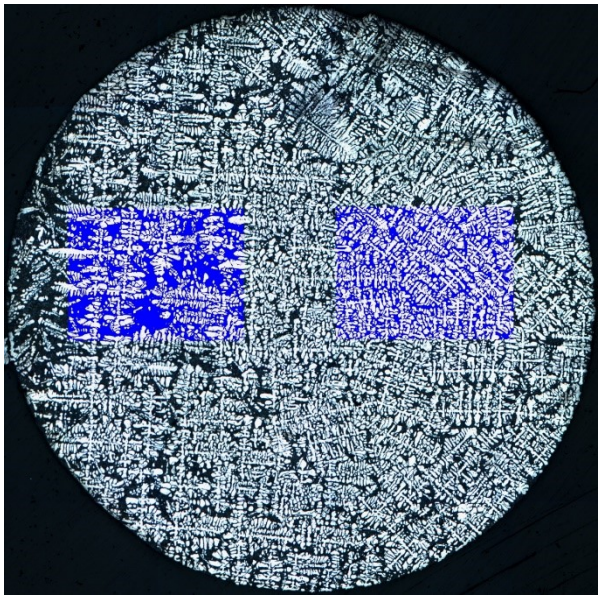

Figure 2.17 Mosaic image of the cross section (XY–TMF, 20 mT) and the measurement areas

Table 2.1 Measurement results on XY–TMF sample

	Left area	**Right area**
Eutectic fraction [%]	54,7	42,5
C_{Si} *[wt.%]*	7,64	6,31

2.4. Conclusions on chapter 2

The solidification facilities constructed on the University of Miskolc were presented. Rotating and travelling magnetic field experiments can be performed with various flow patterns and strengths. The results on binary Al-7wt.%Si using RMF stirring and ternary Al-7wt.%Si-1wt.%Fe alloy with TMF stirring were presented. Both cases' results are useful for validation purposes of the simulations presented in chapter 4.

The gradient shift effect was also presented appearing after turning on the TMF stirring. Such an effect will be used in chapter 4.5.3 for the validation of electromagnetic simulations for the TMF Lorenz force field.

3. Chapter:
Numerical models used in the thesis

3.1. Introduction – Mathematical models used in the thesis

In the Thesis the 2D and 3D numerical simulations were performed for solidification of a binary Al-7wt%Si alloy under the action of the rotating magnetic field (RMF) using macroscopic approach coupled with equilibrium microscopic solidification. Further, simulations with the same boundary conditions were performed with macroscopic approach coupled with the diffusion governed growth model (referred hereafter "envelope model"). Results of simulation were compared with the segregation observed in the Al-7wt%Si sample solidified under these conditions and will be presented in 4. The systems of governing equations used in simulations for the solidification of a sample of a binary alloy under the RMF action are presented in the part 3.1.1 and 3.1.2 respectively.

Further, in the Thesis the 3D simulations were performed for solidification of a ternary Al-7wt%Si – 1wt%Fe alloy under the action of the travelling magnetic field (TMF) using macroscopic approach coupled with equilibrium microscopic solidification. This alloy is characterized by formation of an intermetallic along with the primary dendrites as described in the subsection 3.1.3. The microscopic model based on the lever rule approach and accounting for the presence of the two solid phases is presented in the part 3.1.3 while the part 3.1.4 contains macroscopic equations coupled with the microscopic ones.

To present the equation in the unified manner the index s denotes hereafter solid phase and the index f is related to the fluid phase which can be either pure liquid or the union of the interdenritic and extradendritic liquid depending on the microscopic model. The index l is reserved for extradendritic liquid.

3.1.1. Macroscopic equations for solidification of a binary alloy coupled with an equilibrium solidification

In the system of macroscopic equations coupled with equilibrium solidification model at the microscale was realised in ANSYS Fluent. The columnar solid phase is stationary, and its description does not require any momentum equation. All thermo-physical properties were considered equal for the solid and liquid phase and the Boussinesq linear approximation was used to treat the thermo-solute convection using the thermal and solute volume expansion coefficient β_T and β_C, respectively – presented in chapter 4.2. The thermodynamic temperature T was unique for the liquid and the solid phase, and a heat release (characterized by the latent heat L) due to the phase transition was taken into account. The momentum equation was formulated only for the liquid phase with its intrinsic velocity $\vec{V} = f_f \vec{v}_f$ – f_f presents the fraction of fluid. The presence of the solid phase was taken into account using the Karman-Cozeny approach [Karman][Cozeny] for the pressure drop in the porous zone formed by dendrites. There, the secondary dendrite arm spacing λ_2 was used as a characteristic length for the permeability. The segregation during the solidification was observed using the transport

equation for the average concentration $\langle C \rangle = f_f C_f + f_s C_s$ in which the advection term contained the concentration in the liquid phase C_f .

The liquidus line from the phase diagram was linearized with the liquidus slope m_l and the solid fraction and concentrations were calculated using the partition coefficient $k_p = c_s / c_l$ with a usual agreement $m_l(k_p - 1) > 0$. This gives the following system of equations:

Mass conservation in the liquid phase:

$$\rho_0 \frac{\partial f_f}{\partial t} + \rho_0 \nabla \vec{v} = -\rho_0 \frac{\partial f_s}{\partial t} \tag{3.1}$$

Momentum equation:

$$\rho_0 \frac{\partial \vec{V}}{\partial t} + \frac{\rho_0}{f_f}(\vec{V}.\nabla)\vec{V} = \nabla(\mu_f \nabla \vec{V}) - f_f \nabla p - \frac{\mu_f f_f}{K}\vec{V} + f_f \tilde{\rho}\vec{g} + f_f \vec{F}_{em} \tag{3.2}$$

where $\vec{F}_{em}$ is the density of the effective electromagnetic force calculated elsewhere or approximated analytically and K is a permeability (eq. 3.5).

Heat equation:

$$\rho_0 \frac{\partial T}{\partial t} + \rho_0 c_p \vec{V}.\nabla T = k\nabla^2 T + \rho_0 L \frac{\partial f_s}{\partial t} \tag{3.3}$$

where L denotes the latent heat.

Solute transport

$$\frac{\partial \langle C \rangle}{\partial t} + \vec{V}.\nabla C_f = 0 \tag{3.3}$$

Boussinesq approximation:

$$\tilde{\rho} = \rho_0 (1 - \beta_T (T - T_0) - \beta_C (C_f - C_0)) \tag{3.4}$$

Permeability for the porous zone:

$$K = \frac{\lambda_2^2}{180} \frac{f_f^3}{(1 - f_f)^2} \tag{3.5}$$

Where λ_2 is the secondary dendrite arm spacing.

A linearized phase diagram is presented with the lever rule:

$$T = T_m + m_l C_f \tag{3.6}$$

$$f_s = \frac{1}{k_p - 1} \frac{C_f - \langle C \rangle}{C_f} \tag{3.7}$$

$$f_f + f_s = 1 \tag{3.8}$$

3.1.2. Macroscopic equations for a binary alloy coupled with a diffusion driven growth of dendrites

Models for the solidification and the microscale which accounts for the diffusion growth of the grains were briefly presented in the part 1.4 devoted to the literature review. In particular, a model by Ciobanas and Fautrelle proposed in [8] was mentioned. Further, these authors proposed a coupling of this micro-model with the model for calculations of the transport equations at the macroscale [35]. The latter was realized in ANSYS Fluent using the "user-defined functions" facilities provided by this software. In this section a more detailed presentation of the model is given.

3.1.2.1 A Recall of a diffusion governed gain growth

Similar to the model of Rappaz and Thevoz [4] and Wang a Beckerman [6], the model for the grain growth proposes the presentation of a grain using the notion of the grain envelope and with the introduction of the solid, interdendritic and extradendritic fractions (Figure 3.1) denoted hereafter as f_s, f_d and f_l, whose sum (union) is equal to unity: $fs + f_d + f_l = 1$. Apart from this, the following unions can be identified: the grain fraction f_g is given as union of the solid and dendritic fractions $f_s + f_d = f_g$ and the fluid fraction f_f unifies interdendritic liquid (IDL) and extradendritic liquid (EDL) : $f_d + f_l = f_f$. The interface between the IDL and EDL corresponds to the envelope of grain, i.e. to the imaginary surface connecting the tips of dendrite arms. It is supposed that the maximal possible size of the grain is bounded with a sphere of a radius of R_{tot}. This size is related to the density of the grains $n : R_{tot} = (4\pi n/3)^{-1/3}$. Also, a radius of the grain a and a surface density of the grain S_g are introduced as $a = R_{tot} f_g^{1/3}$ and $S_g = 4\pi a^2 n$.

Further, C_s, C_d, C_l present the average concentration in the solid, IDL and EDL, respectively and their weighted sum is related to the average concentration C within the whole grain: $fsC_s + f_d C_d + f_l C_l = C$. Also, the average concentration in the fluid phase C_f can be introduced as: $f_d C_d + f_l C_l = C_f$. Apart from the concentrations in the volume, two concentrations at the interface between the solid and the IDL exist, $\overline{C}_{sd}$ and $\overline{C}_{ds}$ which are from the side of the solid and from the IDL, respectively. Because of assumption formulated below no interfacial concentration is introduced at the interface between the IDL and EDL.

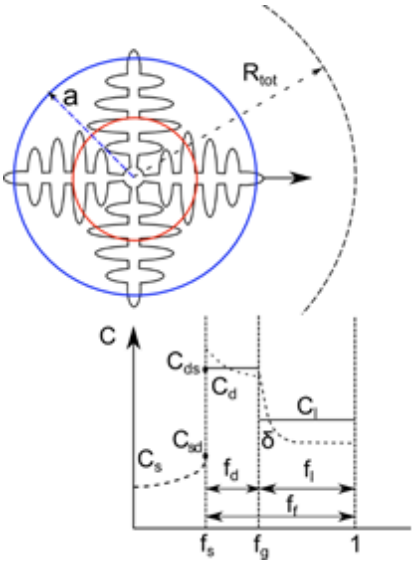

Figure 3.1 Graphical presentation of the grain in the model of Ciobanas and Fautrelle [8] with notions of fractions and concentrations

The assumptions used in the model are similar to those in [4] and [6]:

- the grain is under thermal equilibrium, i.e. the temperature within all zones in the grains is the same and equal to a thermodynamic temperature T.
- the IDL liquid is well mixed and the concentration in this zone corresponds to the liquidus concentration at the thermodynamic temperature denoted here after C_l^*, because of this, the interfacial IDL concentration is also the same: $\overline{C}_{ds} = C_l^*$
- the chemical diffusion in the solid is zero
- the relation between the concentration at the interface solid – IDL in case of solidification is defined with the equilibrium partition coefficient: $\overline{C}_{sd} / \overline{C}_{ds} = \overline{C}_{sd} / C_l^* = k_p$, where in case of the melting the concentration is equal to C_s.
- the average growth velocity of the grain $\overline{w}_g$ (the velocity of the envelope "displacement") is defined by the constitutional supercooling: $\Omega = \left(C_l^* - C_l\right) / \left(C_l^* - \overline{C}_{sd}\right)$ and is given as:

  $$\overline{w}_g = \frac{D_l m_l \left(k_p - 1\right) C_l^*}{\pi^2 \Gamma} a^2 \left(\frac{\Omega}{1-\Omega}\right)^{2b}$$

  where $a = 0.4567$ and $b = 1.195$ are coefficients proposed in [6], D_l is a chemical diffusion in the liquid and Γ is a Gibbs-Thomson coefficient.
- the diffusive flux from IDL to EDL occurs through the surface of the grain S_g and is defined by a diffusion length δ, the expression for the latter being complicated is not given here but can be found in [8].

A closed system of equations allowing one to obtain solution for the fractions and concentration is formulated in the next subsection.

3.1.2.2 Macroscopic equations

The solidification micro-model presented above was introduced in ANSYS Fluent and coupled with the Euler-Euler two-phase flow. The consideration of only two phases in the macroscopic transport equations is necessary because the solid and the grain fraction move together being linked one to another. In fact, there is a choice to be made for which phases the convective transport equations have to be calculated. The most evident options are either fluid and solid or fluid and grain. The system of equations proposed in [50] the choice for a pair "fluid and solid" was made. This implies that the fluid phase includes IDL and EDL and extradendritic liquid assumes both the pure liquid and the liquid in the vicinity of a grain (within the R_{tot}) but outside its envelope. Then, with the notion for the intrinsic velocity in the fluid phase $\vec{V} = f_f \vec{v}_f$, the system of macroscopic equations can be presented as follows:

Energy equation shared by both phases:

$$\rho_0 \frac{\partial T}{\partial t} + \rho_0 c_p \vec{V}.\nabla T = k\nabla^2 T + L\Gamma_S \tag{3.9}$$

where L denotes the latent heat.

Mass conservation in the fluid phase (union of IDL and EDL):

$$\rho_0 \frac{\partial f_f}{\partial t} + \rho_0 \nabla \vec{V} = -\Gamma_s \tag{3.10}$$

Momentum equation in the fluid phase:

$$\rho_0 \frac{\partial \vec{V}}{\partial t} + \frac{\rho_0}{f_f}\left(\vec{V}.\nabla\right)\vec{V} = \nabla\left(\mu_l \nabla \vec{V}\right) - f_f \nabla p - \frac{\mu_l f_f}{K}\vec{V} + f_f \tilde{\rho}\vec{g} + f_f \vec{F}_{em} \tag{3.11}$$

where, similar to (eq. 3.2), $\vec{F}_{em}$ is the density of the effective electromagnetic force calculated elsewhere or approximated analytically (presented in several chapters below) and K is a permeability, similar to the one given by (eq. 3.5):

$$K = \frac{\lambda_2^2}{180}\frac{f_f^3}{(1-f_f)^2}$$

Macroscopic solute transport equations in the fluid phase:

$$\rho_0 \frac{\partial (f_l C_f)}{\partial t} + \vec{V}.\nabla C_f = -\Gamma_s \overline{C}_{sd}$$

No macroscopic transport equations are solved for the solid phase since it is supposed to be columnar, i.e. stationary.

Yet, the system of equations (3.9), (3.10) and (3.11) is coupled with the following equations from the microscopic model:

Liquidus concentration:

$$C_l^* = \frac{T - T_m}{m_l}$$

Mass conservation in the solid and IDL:

$$\rho_0 \frac{\partial f_s}{\partial t} = \Gamma_s \qquad \text{and} \qquad \rho_0 \frac{\partial f_d}{\partial t} = -\Gamma_s + \Gamma_g \text{ with } \Gamma_g = \rho_0 S_g \overline{w}_g$$

Solute conservation in the solid and IDL:

$$\rho \frac{\partial (f_s C_s)}{\partial t} = \Gamma_s \overline{C}_{sd} \qquad \text{and} \qquad \rho_0 f_d \frac{\partial (C_l^*)}{\partial t} = \Gamma_s \left(C_l^* - C_{sd}\right) + \frac{\rho_0 S_g D_f}{\delta}\left(C_l - C_l^*\right)$$

$$\overline{C}_{sd} = \begin{bmatrix} k_p C_l^* & if \quad \Gamma_S > 0 \\ C_s & if \quad \Gamma_S < 0 \end{bmatrix}$$

3.1.3. Microscopic model for the solidification of a ternary alloy

3.1.3.1 Linearization of the phase diagram for the ternary alloy

Equilibrium theoretical models based on a lever or Scheil rule and on their combinations for solidification of a ternary alloy are presented in detail in [2]. It should be noted that in all solidification regimes, including eutectic, [2] proposes to use partition coefficients to calculate the equilibrium concentration in the solid. Yet, another approach can be used based on the knowledge of the composition of the solid which is formed. In solidification of a Al-Si-Fe alloy in aluminum-rich corner, various intermetallics can form depending on the initial composition of the alloy (Figure 3.2).

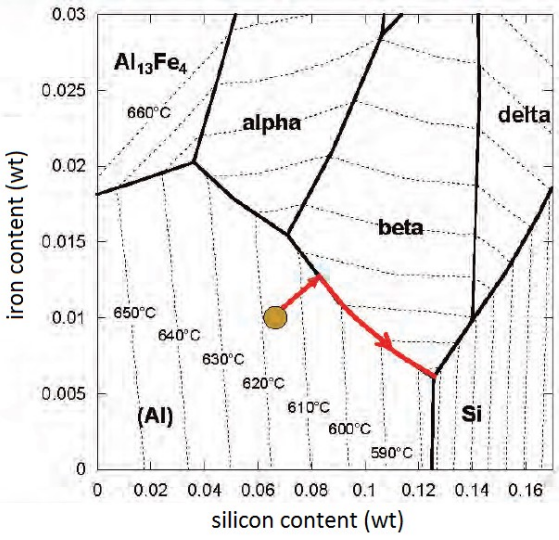

Figure 3.2 Projection of the phase diagram on the liquidus surface: isolines of liquidus temperature are shown with dot lines. Composition of the beta phase is $Al_9Fe_2Si_2$

The phase diagram for the ternary alloy (Figure 3.2) was linearized using data for the liquidus surface and partition coefficients calculated by J. Lacaze in ThermoCalc software (http://www.thermocalc.com/).

The liquidus surface which corresponds to the solidification of primary aluminum rich dendrite was approximated with a plane using multiple (multivariable) linear regression method (https://en.wikipedia.org/wiki/Linear_regression). This resulted in its presentation in the form

$$T_l = T_m + m_{Si}C_{si,f} + m_{Fe}C_{Fe,f} \tag{3.12}$$

where T_m is a melting temperature of a pure aluminum whose value is discussed below, and the slope coefficients are the partial derivatives:

$$m_{Si} = {\partial T_l}/{\partial C_{Si,f}} \quad \text{and} \quad m_{Fe} = {\partial T_l}/{\partial C_{Fe,f}} \tag{3.13}$$

The linearization procedure was made in order to have a minimal error between the liquid temperature given by eq. (3.12) and the one calculated in ThermoCalc in the region of interest, i.e. for the range of concentration of silicon and iron $0.06wt < C_{Si} < 0.126wt$ and $0.5wt < C_{Fe} < 1.7wt$, respectively. Consequently, the value for the melting temperature of a pure aluminum T_m used further in calculations was found slightly different from the actual one and equal to 939.17049 K. Other values can be found in the Table 1.

Further, the line of eutectic solidification along which the solidification of the primary aluminum-rich dendrites and formation of the intermetallics was approximated with a straight line passing through the ternary eutectic point having the concentrations $C_{Si,E}$, $C_{Fe,E}$. That gives the following relation between two concentrations in the liquid along this line:

$$C_{Fe,f} = q_f C_{Si,f} + r_f \tag{3.14}$$

Combining the eq. (3.12) and eq. (3.13), one can obtain also a direct relation between the liquidus temperature and both concentrations in the liquid:

$$m_{Fe}C_{Fe,f} = T_l - T_m - m_{Si}C_{Si,f}$$

$$m_{Fe}(qC_{Si,.f} + r) = T_l - T_m - m_{Si}C_{Si,f}$$

$$(m_{Fe}q + m_{si})C_{Si,f} = T_l - T_m - m_{Fe}r$$

$$C_{Si,f} = \frac{T_l - T_m - m_{Fe}r}{m_{Fe}q + m_{Si}} = q_1 T_l + r_1 \tag{3.15}$$

Similarly, one can obtain the relation between the liquidus temperature and concentration of the second component in the liquid:

$$C_{Fe,f} = q_2 T_l + r_2$$

Finally, the value of the concentrations of the silicon in the ternary eutectic point was taken equal to $C_{Si,E} = 0.126wt$, other values can be found in the Table 1.

Table 3.1 Values used for the linearization of the Al-rich corner of AlSiFe phase diagram

Variable	Value	Variable	Value
Melting temperature (in Eq.1) T_m^* **[K]**	939.17	Coefficient q_1 in eq.(3.15)	-0.15
Partial liquidus slope for Si, m_1 **[K/%wt]**	-7.0486	Coefficient r_1 in eq.(3.15)	139.8
Partial liquidus slope for Fe, m_2 **[K/%wt]**	-2.1025	Coefficient q_f in eq.(3.14)	-0.17757
Partition coefficient for Si, k_1	0.115	Coefficient r_f in eq.(3.14)	2.75
Partition coefficient for Fe, k_2	0.01	Eutectic temperature T_{EP} [K]	849.208

Using the linearization of the liquidus surface and eutectic line on the phase diagram, the following equations were developed for the solution of the solidification problem under lever rule approximation.

3.1.3.2 Equation for the solidification of a ternary alloy with formation of a unique primary aluminium-rich dendrite phase

In the case when only the primary dendrite α - phase is solidified, the average concentration of each component is divided between the liquid and solid phase. In the lever rule approach, because of the infinitely rapid diffusion in both phases the concentration in the solid phase is equal to the one at the solid-liquid interface, defined with a partition coefficient:

$$C_{Si} = f_f C_{Si,f} + f_{s,\alpha} C_{Si,s} = f_f C_{Si,f} + k_{Si,\alpha} f_{s,\alpha} C_{Si,f}$$

$$C_{Fe} = f_f C_{Fe,f} + C_{Fe,s} = f_f C_{Si,f} + k_{Fe,\alpha} f_{s,\alpha} C_{Si,f}$$

$$f_f + f_{s,\alpha} = 1$$

That gives a standard relation of a lever rule between the concentrations in the liquid, the average concentration and the solid fraction, applied for each component:

$$C_{Si,f} = \frac{C_{Si}}{1 + f_\alpha \left(k_{Si,\alpha} - 1\right)} \tag{3.16}$$

$$C_{Fe,f} = \frac{C_{Fe}}{1 + f_\alpha \left(k_{Fe,\alpha} - 1\right)} \tag{3.17}$$

Along with the equation for the liquidus temperature defined by the average concentration of each component:

$$T_l = T_m + m_{Si} C_{Si,f} + m_{Fe} C_{Fe,f}$$

Accounting for these equations, a quadratic equation for the solid fraction can be deduced that gives:

$$A f_\alpha^2 + B f_\alpha + E = 0$$

With

$$A = (k_{Si,\alpha} - 1)(k_{Fe,\alpha} - 1)(T_l - T_m) \tag{3.18}$$

$$B = \left(k_{Si,\alpha} + k_{Fe,\alpha} - 2\right)(T_l - T_m) - \left(k_{Fe,\alpha} - 1\right) m_{Si,\alpha} C_{Si} - \left(k_{Si,\alpha} - 1\right) m_{Fe,\alpha} C_{Fe} \tag{3.19}$$

$$E = T_l - T_m - m_{Si} C_{Si} - m_{Fe} C_{Fe} \tag{3.20}$$

Then the primary solid fraction of the aluminum dendrites is defined via solution of the quadratic equation:

$$f_\alpha = \frac{-B + \sqrt{B^2 - 4AE}}{2A} \tag{3.21}$$

Further, the concentrations of the components in the liquid phase, $C_{Si,f}$ and $C_{Fe,f}$, can be found with equations (3.16) and (3.17).

3.1.3.3 Equation for the solidification with intermetallic phase in the approximation of the lever rule

The solidification of a unique dendritic phase occurs until the concentrations in the liquid phase reach the eutectic line on the ternary phase diagram. Taking into account the approximation of the eutectic line by a straight line given by eq.4, we can recognize that under the condition $C_{Si,f} < qC_{Fe,f} + r$ only the dendrite phase is solidified (Figure 3.3), therefore, eqs. (3.16) –(3.21) can be applied. Otherwise, another system of equations should be used.

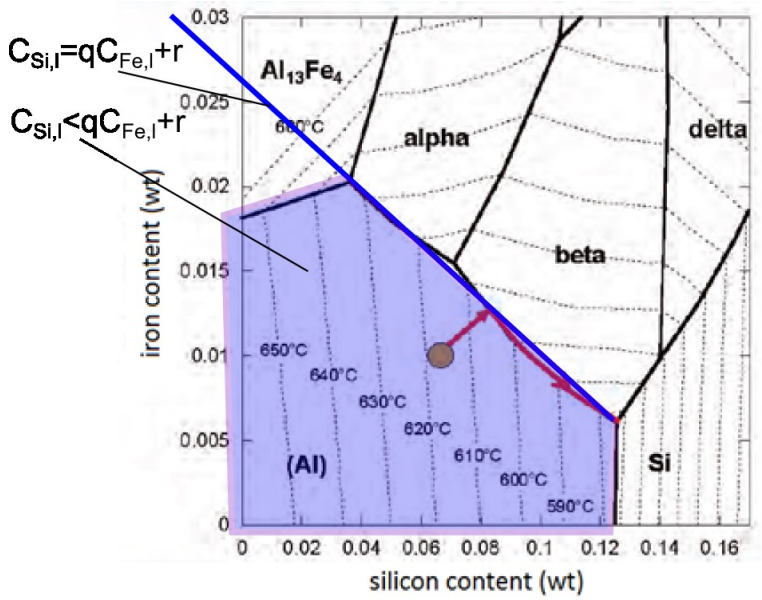

Figure 3.3

Indeed, with the presence of the third, intermetallic phase, we can present the equations for the concentration of the two components as follows:

$$C_{Si} = f_f \cdot C_{Si,f} + f_\alpha \cdot C_{Si,\alpha} + f_\beta \cdot C_{Si,\beta} \tag{3.22}$$

$$C_{Fe} = f_f \cdot C_{Fe,f} + f_\alpha \cdot C_{Fe,\alpha} + f_\beta \cdot C_{Fe,\beta} \tag{3.23}$$

First, a concentration in the liquid for both components $C_{Si,l}$ and $C_{Fe,l}$, can be obtained directly from the liquidus temperature using the equations (3.14) and (3.15) from the linearization of the eutectic line. Second, the composition of each component taken by the intermetallics is known while for the crystallization of the primary phase the segregation coefficients for each component can be used. That gives:

$$C_{Si} = f_f \cdot C_{Si,f} + f_\alpha \cdot k_{Si,\alpha} \cdot C_{Si,f} + f_\beta \cdot C_{Si,\beta}$$

$$C_{Fe} = f_f \cdot C_{Fe,f} + f_\alpha \cdot k_{Fe,\alpha} \cdot C_{Fe,f} + f_\beta \cdot C_{Fe,\beta}$$

Accounting for the summation of the phases:

$$f_f + f_\alpha + f_\beta = 1$$

One can obtain expression for the calculation of the fractions of the intermetallic phase and primary phase:

$$f_\alpha = \left[\frac{C_{Si} - C_{Si,f}}{C_{Si,f} - C_{Si,\beta}} - \frac{C_{Fe} - C_{Fe,f}}{C_{Fe,f} - C_{Fe,\beta}}\right]\left[\frac{C_{Fe,f}\left(1-k_{Fe,\alpha}\right)}{C_{Fe,f} - C_{Fe,\beta}} - \frac{C_{Si,f}\left(1-k_{Si,\alpha}\right)}{C_{Si,f} - C_{Si,\beta}}\right]^{-1} \quad (3.24)$$

$$f_\beta = \left[\frac{C_{Si} - C_{Si,f}}{C_{Si,f}\left(1-k_{Si,\alpha}\right)} - \frac{C_{Fe} - C_{Fe,f}}{C_{Fe,f}\left(1-k_{Fe,\alpha}\right)}\right]\left[\frac{C_{Fe,f} - C_{Fe,\beta}}{C_{Fe,f}\left(1-k_{Fe,\alpha}\right)} - \frac{C_{Si,f} - C_{Si,\beta}}{C_{Si,f}\left(1-k_{Si,\alpha}\right)}\right]^{-1} \quad (3.25)$$

The solid phase is a sum of the two fractions:

$$f_s = f_\alpha + f_\beta \quad (3.26)$$

3.1.4. Macroscopic equations for a ternary alloy coupled with an equilibrium solidification

Momentum equation:

$$\rho_0 \frac{\partial \vec{V}}{\partial t} + \frac{\rho_0}{f_l}\left(\vec{V}.\nabla\right)\vec{V} = \nabla\left(\mu_l \nabla \vec{V}\right) - f_l \nabla p - \frac{\mu_l f_l}{K}\vec{V} + f_l \tilde{\rho}\vec{g} + f_l \vec{F}_{em} \quad (3.27)$$

where $\vec{F}_{em}$ is the density of the effective electromagnetic force calculated elsewhere or approximated analytically and K is a permeability given above by eq.(3.5).

Heat equation:

$$\rho_0 \frac{\partial T}{\partial t} + \rho_0 c_p \vec{V}.\nabla T = k\nabla^2 T + \rho_0 L \frac{\partial f_s}{\partial t} \quad (3.28)$$

Solute transport of the two component:

$$\frac{\partial \langle C_{Si} \rangle}{\partial t} + \vec{V}.\nabla C_{Si,f} = 0 \qquad \text{and} \qquad \frac{\partial \langle C_{Fe} \rangle}{\partial t} + \vec{V}.\nabla C_{Fe,f} = 0 \quad (3.29)$$

Boussinesque approximation:

$$\tilde{\rho} = \rho_0\left(1 - \beta_T\left(T - T_0\right) - \beta_{C,Si}\left(C_{Si,f} - C_{Si,0}\right) - \beta_{C,Fei}\left(C_{Fe,f} - C_{Fe,0}\right)\right) \quad (3.30)$$

A linearized phase diagram is presented with the lever rule:

If $C_{Si,f} < qC_{Fe,f} + r$ (one solid phase in dendrites's form is presented):

$$f_s = f_\alpha = \frac{-B + \sqrt{B^2 - 4AE}}{2A}, \qquad A, B \text{ and } E \text{ are defined by eqs. (3.18)-(320)}$$

$$C_{Si,f} = \frac{C_{Si}}{1 + f_\alpha (k_{Si,\alpha} - 1)} \qquad \text{and} \qquad C_{Fe,f} = \frac{C_{Fe}}{1 + f_\alpha (k_{Fe,\alpha} - 1)}$$

If $C_{Si,f} = qC_{Fe,f} + r$ (solidification along the eutectic line):

$$C_{Si,f} = q_1 T + r_1 \qquad \text{and} \qquad C_{Fe,f} = q_2 T + r_1$$

$$f_\alpha = \left[\frac{C_{Si} - C_{Si,f}}{C_{Si,f} - C_{Si,\beta}} - \frac{C_{Fe} - C_{Fe,f}}{C_{Fe,f} - C_{Fe,\beta}} \right] \left[\frac{C_{Fe,f}(1 - k_{Fe,\alpha})}{C_{Fe,f} - C_{Fe,\beta}} - \frac{C_{Si,f}(1 - k_{Si,\alpha})}{C_{Si,f} - C_{Si,\beta}} \right]^{-1}$$

$$f_\beta = \left[\frac{C_{Si} - C_{Si,f}}{C_{Si,f}(1 - k_{Si,\alpha})} - \frac{C_{Fe} - C_{Fe,f}}{C_{Fe,f}(1 - k_{Fe,\alpha})} \right] \left[\frac{C_{Fe,f} - C_{Fe,\beta}}{C_{Fe,f}(1 - k_{Fe,\alpha})} - \frac{C_{Si,f} - C_{Si,\beta}}{C_{Si,f}(1 - k_{Si,\alpha})} \right]^{-1}$$

$$f_s = f_\alpha + f_\beta$$

3.2. Conclusions on the numerical models

The numerical solutions used in the thesis project were presented. The solutions can be rather similar, but the simulations can lead into very different results since the approaches are numerically distinct. The Lever rule model can be solved analytically, on the other hand the Envelope cases need the ensemble averaging method.

The performance of the lever rule and the Envelope model regarding solute distribution compared with measurement is presented in chapter 4. The results on ternary simulations are presented in the same chapter.

4. Chapter:
Numerical and experimental results

4.1. Introduction on solidification modeling

This chapter presents the results on the solidification simulation. First, the binary RMF cases are presented for binary Al-7wt.%Si alloy. Two sets of models are kept separately – Lever rule and Envelope models and 2D + 3D for each – but comparison of the results is done together on the four models. Performance of the solute conservation of Lever rule and Envelope method is also discussed.

In case of TMF simulations, preparation work had to be done numerically, since the Lorenz force field of the inductor cannot be described analytically. Comsol Multiphysics was used for electromagnetic simulations to obtain the Lorenz force field. The thermal effect presented in chapter 2.3.2.1 was simulated to quasi-validate the Comsol results, which was later used in solidification simulations on Al-7wt.%Si-1wt.%Fe ternary alloy. Two simulations are presented. One with bidirectional and another one with upward Lorenz force field. In the case of bidirectional force field, comparison is done with texture images of cross section of the sample. Only numerical results are presented for the upward force field case.

4.2. Material properties

The material properties used in the models are presented in Table 4.3.

Table 4.1 Material properties used in the solidification models

Envelope- and Lever rule-based models		Ternary models	
$\boldsymbol{\rho_{liquid}, \rho_{solid}}$	2452 kg/m^3	*	
$\boldsymbol{c_{p,liquid}}$	1140 J/kgK	$c_{p,liquid}$	1140 J/kgK
$\boldsymbol{\lambda_{liquid}, \lambda_{solid}}$	100 W/mK	$\lambda_{liquid}, \lambda_{solid}$	100 W/mK
$\boldsymbol{D_l}$	3e-9 m^2/s	$D_{l,Si}$	5e-9 m^2/s
-	-	$D_{l,Fe}$	2,5e-9 m^2/s
$\boldsymbol{D_s}$	0 m^2/s	D_s	0 m^2/s
$\boldsymbol{\mu_{liquid}}$	0,00252 Pa•s	μ_{liquid}	0,00252 Pa•s
$\boldsymbol{\beta_T}$	1,2e3 1/K	*	
$\boldsymbol{\beta_C}$	-2,5e-4 1/wt.%	*	
$\boldsymbol{k_p}$	0,13	$k_{p,Si}$	0,115
-	-	$k_{p,Si}$	0,01
$\boldsymbol{m_l}$	-6,62	$m_{l,Si(plane)}$	-7,049
-	-	$m_{l,Fe(straight\_line)}$	-0,1776
		$Eutectic\ shift$	2,7499
$\boldsymbol{L}$	400000 J/kg	L	400000 J/kg
$\boldsymbol{\Gamma}$	2,41e-7	Γ	2,41e-7
$\boldsymbol{C_0}$	7 wt.%	$C_{0,Si}$	6,5 wt.%
-	-	$C_{0,Fe}$	0,93 wt.%
$\boldsymbol{T_{melt,Al}}$	993,5 K	$T_{melt,Al}$	939,17049 K
$\boldsymbol{T_{Eut}}$	850 K	-	-
$\boldsymbol{C_E}$	12,2 wt.%	-	-
$\boldsymbol{n\ (for\ Envelope)}$	1e9	-	-
$\boldsymbol{r_{nucl}\ (for\ Envelope)}$	1e-6 m	-	-
$\boldsymbol{\lambda_1}$	400 µm	λ_1	400 µm
$\boldsymbol{\lambda_2}$	65 µm	λ_2	65 µm
$\boldsymbol{\omega_0}$	314 rad/s	**	
$\boldsymbol{\sigma}$	3,74e6 S/m	σ	3,74e6 S/m
$\boldsymbol{B_0}$	20 mT	**	

*The density and the Buoyancy flow was based on the equations of Kaptay provided in a personal document based on articles: [60]-[62].

**The Lorenz force field is described in chapter 4.5.2.

4.3. RMF simulations

The following chapter will present numerical results on the experiment presented in chapter 2.3.1. The main technical parameters important for simulation are the magnetic induction, frequency and the temperature field dataset. Using the data of temperature field has great advantages for the models. The thermal gradient, sample movement velocity, thermal fluctuations are stored in the dataset. If the field is applied on all the walls of the crucible, no special treatment is needed for the boundary conditions and no effort is needed for the simulation of several experimental parameters. Four models were provided for the same experiment with comparison reasons. These were:

- 2D axisymmertical system using Envelope method for solidification modeling
- 3D model using Envelope method for solidification modeling
- 2D model using Lever rule for solidification modeling
- 3D model using Lever rule for solidification modeling

The application of solidification modeling into Fluent is done at SIMaP/EPM Laboratory (Grenoble, France) since approximately 2007 by Ciobanas, Noeppel, Fautrelle, Budenkova and Du Terrail. For Envelope method an averaging structure must be applied since the model itself is written for the growth of a single grain, but one mesh cell can contain arbitrary number of growing dendrites and every cell can have different temperature, concentration, etc.

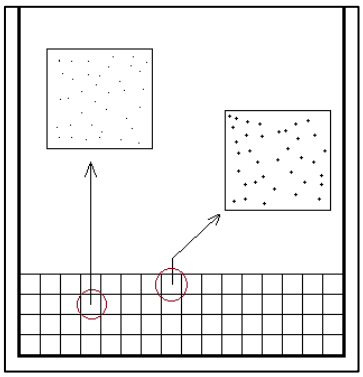

Figure 4.1 Difference between cells

The solution is called ensemble averaging and was designed by Ciobanas et al [8]. The system of equations is rebuilt in an averaged form and modified to compute on phase ratios instead of radii of solid, interdendritic liquid and extradendritic liquid phases [4][8]. The model itself is written in a user defined scalar in Fluent. When the scalar, which contains the solidification model is computed, the iterations of it are performed. Using such approach every time step has sub time-steps with sub-iterations resulting in a "dual-layer" model. Ansys Fluent was chosen to be the main environment for the calculations due to its strength in complex heat and mass transfer solutions. The flow model was used as it is included in the program with momentum sources for the above described Lorenz force field.

4.4. 2D & 3D Envelope

Two models were prepared for two purposes. First is to see results on the experiments of Miskolc using Envelope method, and second, to see if the 3D modeling has any advantage compared to 2D axisymmetrical. 2D models were already published by Budenkova et al. [28] in collaboration with MTA-ME Materials Research Group. The model was using Lever rule in a 2D axisymmetrical case.

Both cases were transient using Eulerian-Eulerian model for the multiphase problem. The two phases were solid and liquid. The solid is modeled as a liquid phase with ultrahigh viscosity – 1 Pa·s. It helps the convergence of the models.

One can observe that one more liquid phase is needed for the usage of Envelope approach. The Eulerian liquid phase is the sum of inter- and extradendritic liquid. The two phases share the same temperature field and have the same flow parameters. The concentration is also treated in a shared and averaged form. For the diffusion problem between the phases, Ciobanas [8] developed his own approach, which was used in the current work.

The growth model including the diffusion and concentration conservation law is calculated in a user defined scalar. The calculation is done iteratively with a self-written code provided by the French Laboratory.

The original energy model of Fluent is not used, but a self-written system is provided to be able to better treat heat fluxes, latent heat, eutectic reaction and the effect of the flow. The temperature data of the 13 thermocouples is interpolated (in time and space) on the walls as fixed values for every time step.

The 2D case was modeled in a rectangle of 4x100 mm meshed with 40000 quad cells (100x100 µm cells). For 3D, a cylinder of Ø8x100 mm was used meshed with 605000 hexahedron cells.

4.4.1. Flow field

Regarding the flow, the four models show very similar results – as was expected from the setup. The form of the flow is identical, and the magnitude is very close to each other – Figure 4.2 & Figure 4.3.

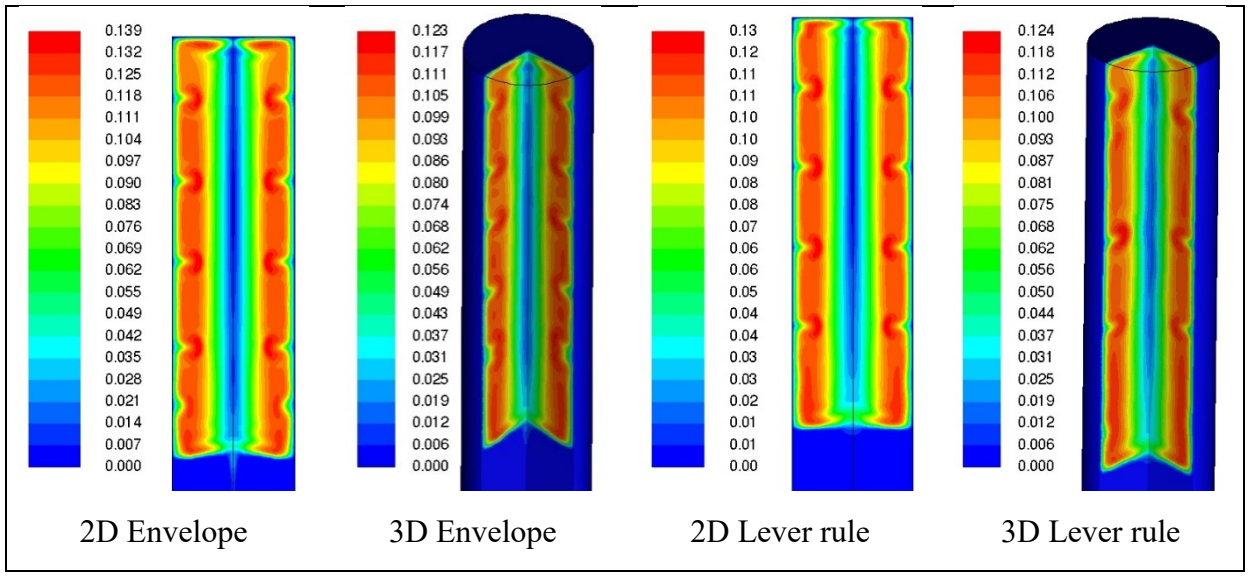

Figure 4.2 Flow filed of each model – contours of velocity [m/s]

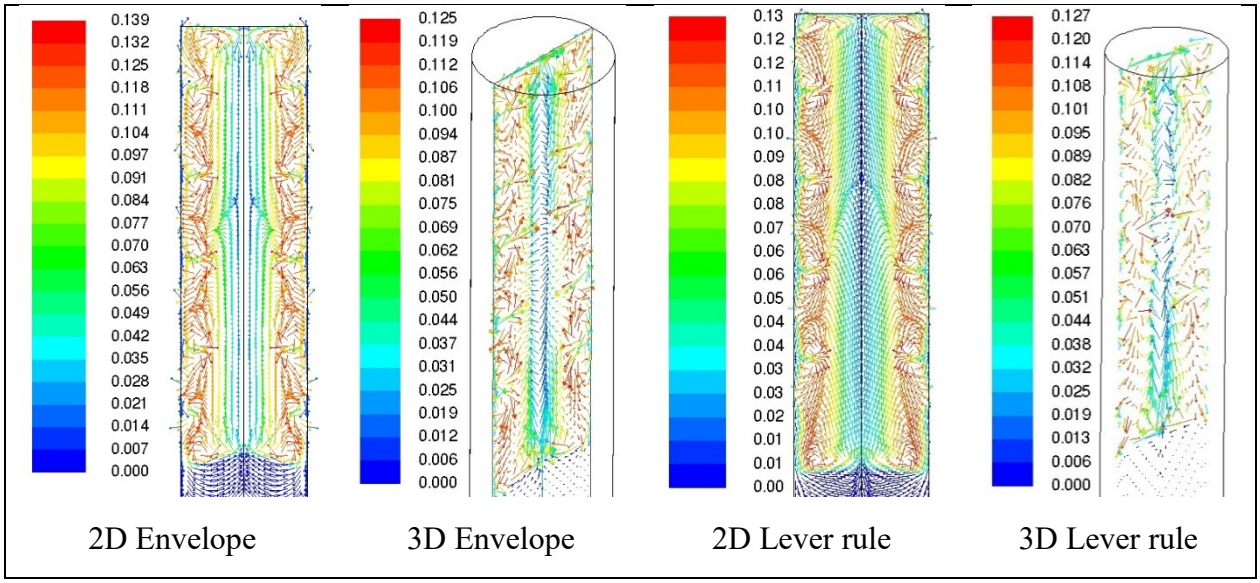

Figure 4.3 Flow filed – vectors of velocity colored by velocity magnitude [m/s]

The maximal velocity can differ which is the result of the difference in the 2D and 3D approach. These results prove that no difference should be considered due to the flow. One can also see on the vector images, that the same dual-level secondary flow is developed in all the 4 models. Along the axis, about half of the molten media is flowing upwards and the other half downwards. Figure 4.4 shows the vectors of velocity magnitude colored by solute concentration (wt.% Si). Based on the distribution of silicon, the dual direction flow is clear.

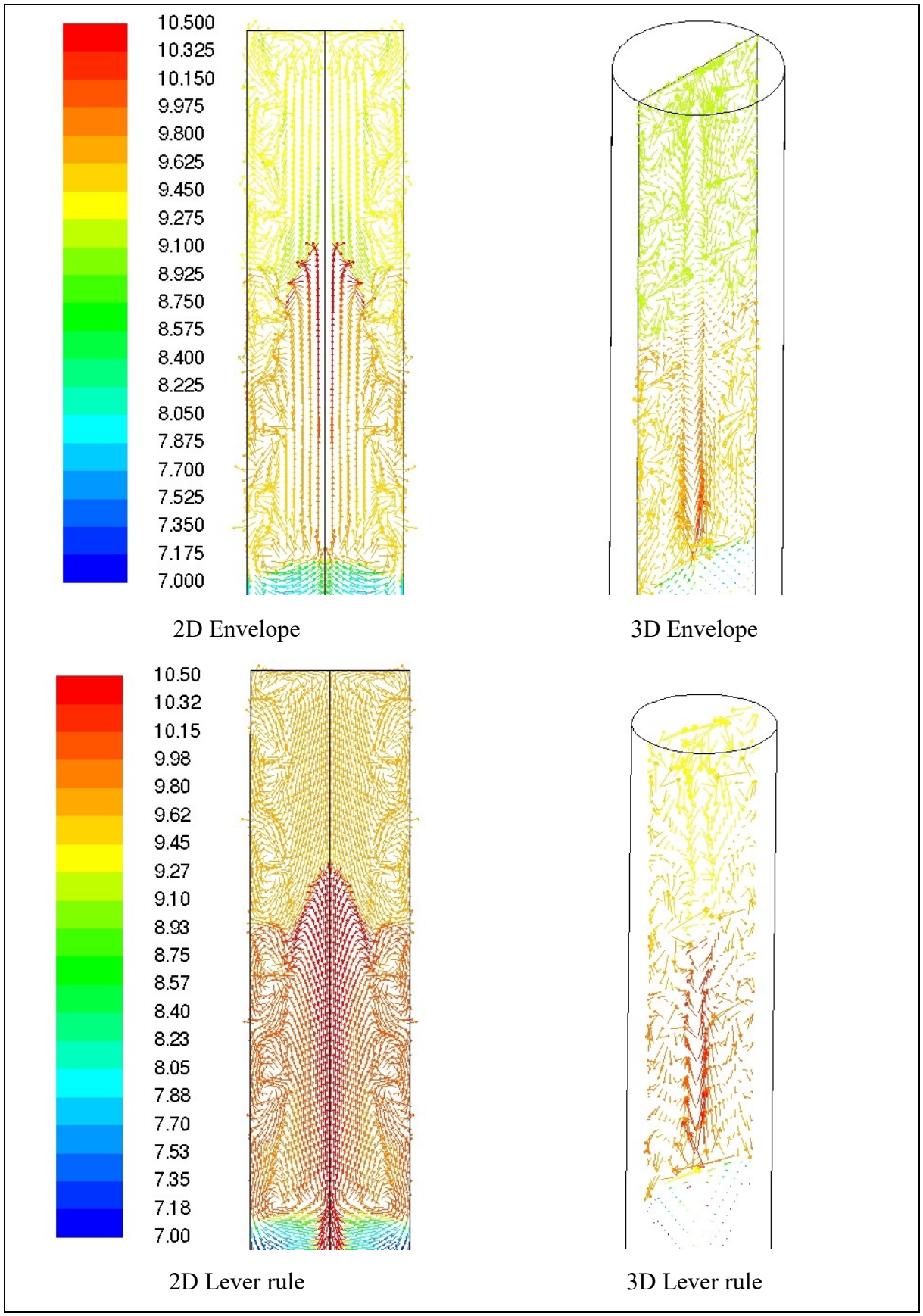

Figure 4.4 Vectors of velocity colored by average Si concentration [wt.%]

4.4.2. Form of the mushy zone

The mushy zone can be interesting since its form and height or thickness are depending on thermal and solidification parameters. The thickness is depending on the thermal gradient, which is identical and fix in all models, therefore the height of the mushy zone is also identical – Figure 4.5. The main difference in the shape is coming from the solute rejection in the solid phase during crystal growth.

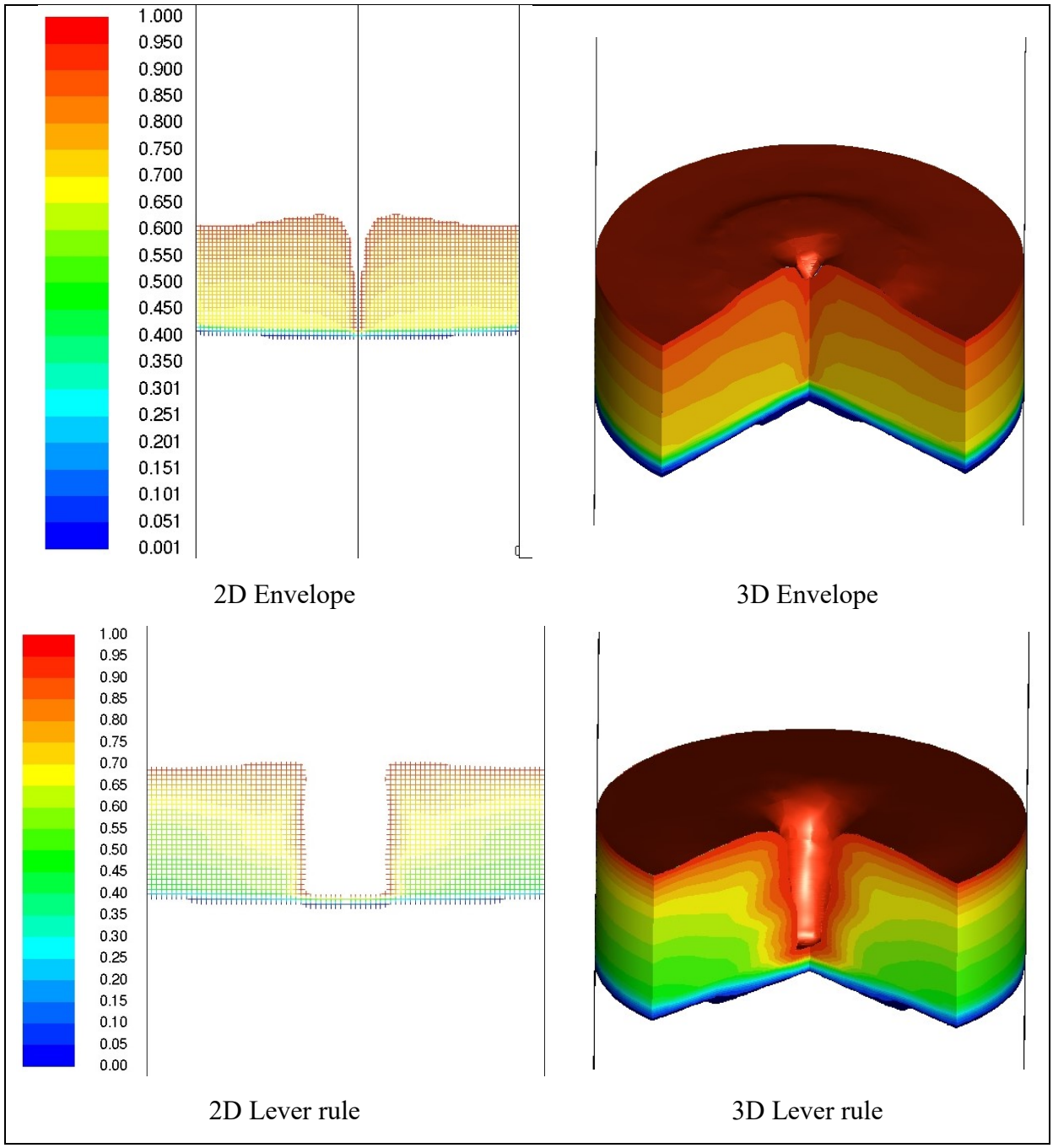

Figure 4.5 Form of the mushy zone colored by volume fraction of liquid

If the average concentration has different distribution in the mushy zone for Lever and Envelope cases. The central overdiluted zone – which is not part of the mushy zone – is much wider in case of Lever rule.

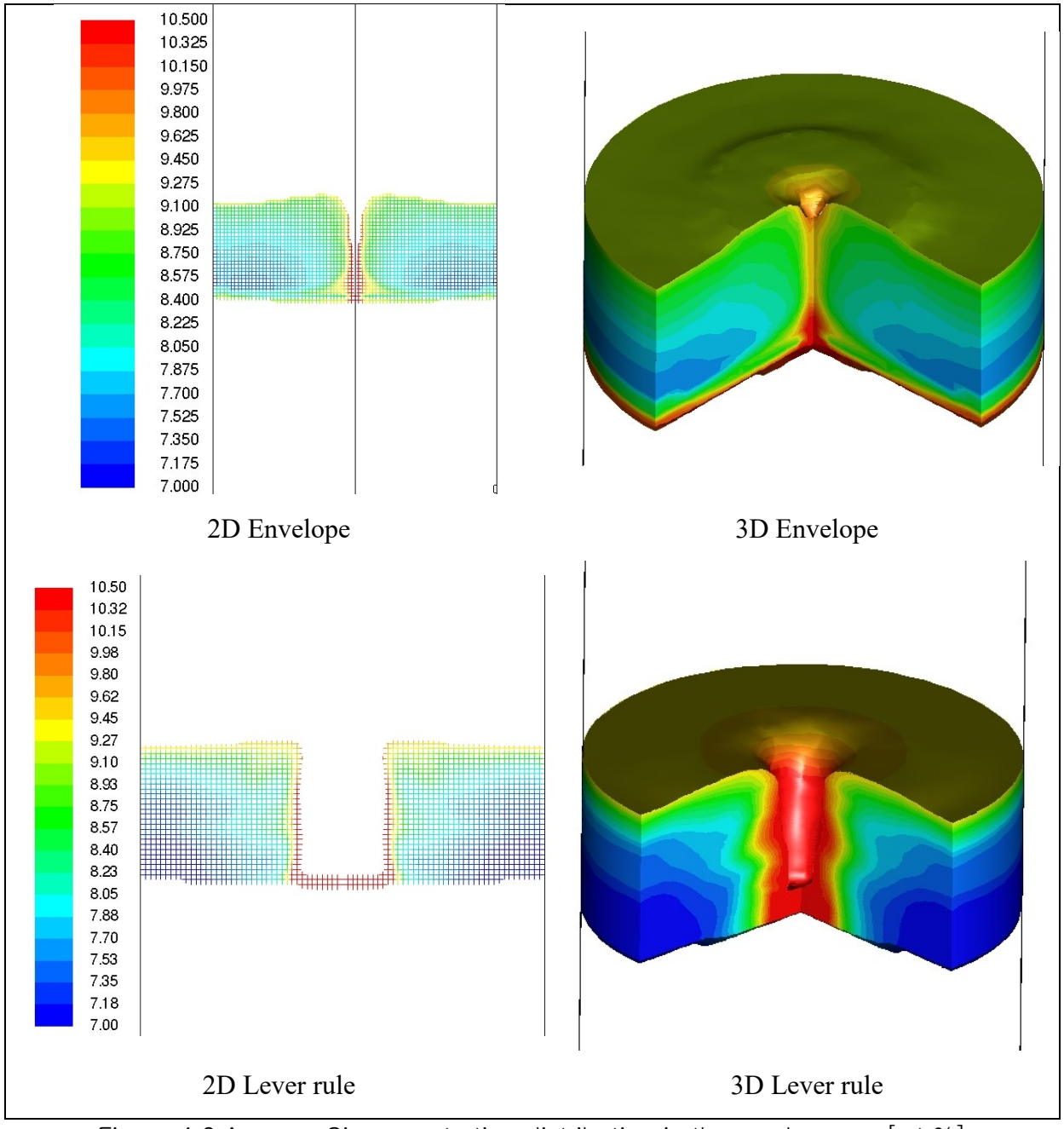

Figure 4.6 Average Si concentration distribution in the mushy zone [wt.%]

The flow coming out of the mushy zone is presented on Figure 4.7 with pathlines colored by average concentration of Si. It can be observed that the central upward flow region is wider in case of the lever rule. This effect suggests different results on the solute distribution.

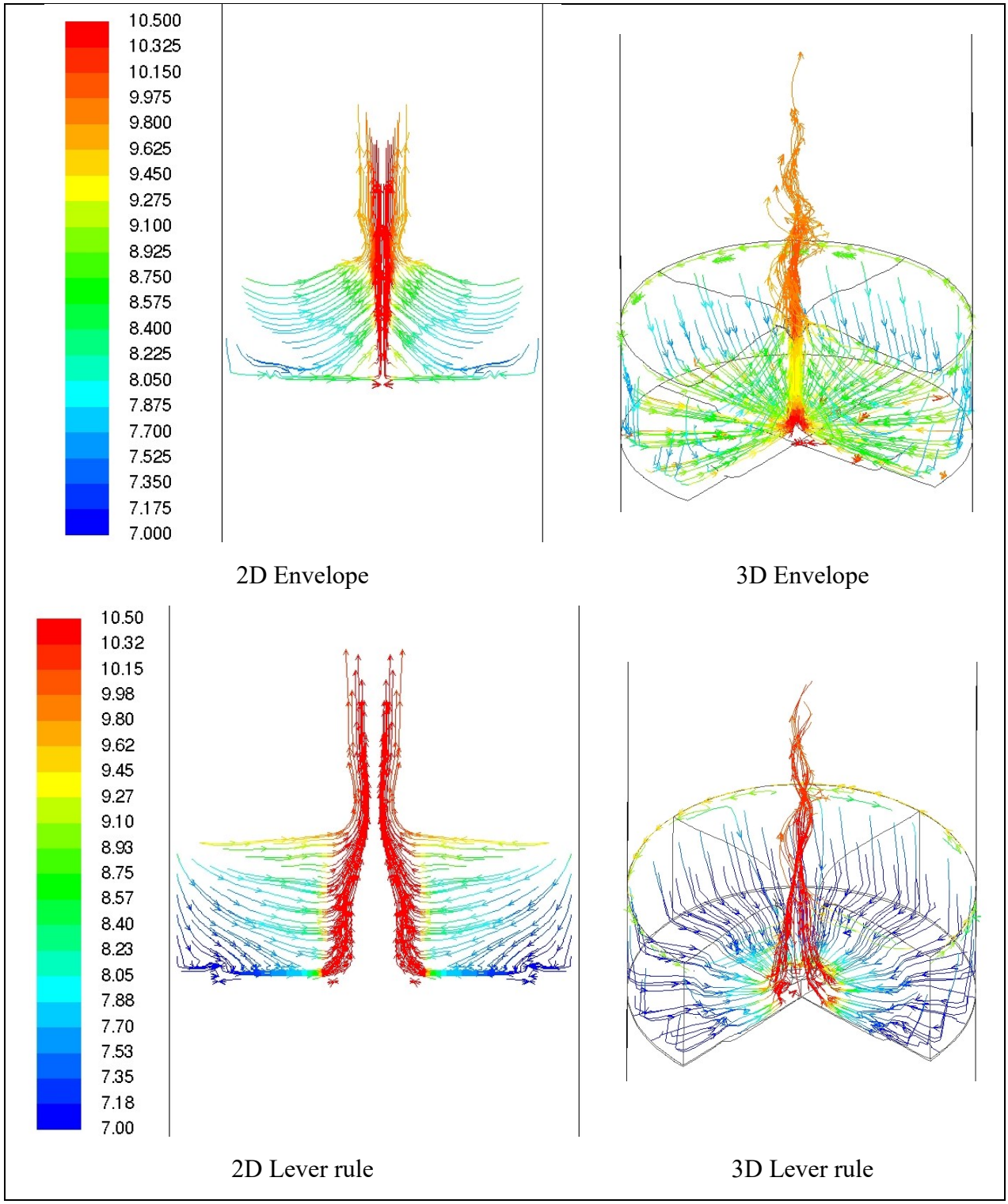

Figure 4.7 Pathlines of velocity magnitude starting from the mushy zone – colored by average Si concentration [wt.%]

4.4.3. Solute distribution

The Si concentration in each case is presented on Figure 4.8. All cases providing central segregation just as the experiment, however the distribution of the solute is different. The ranges of the concentration and the form of the segregation is slightly different.

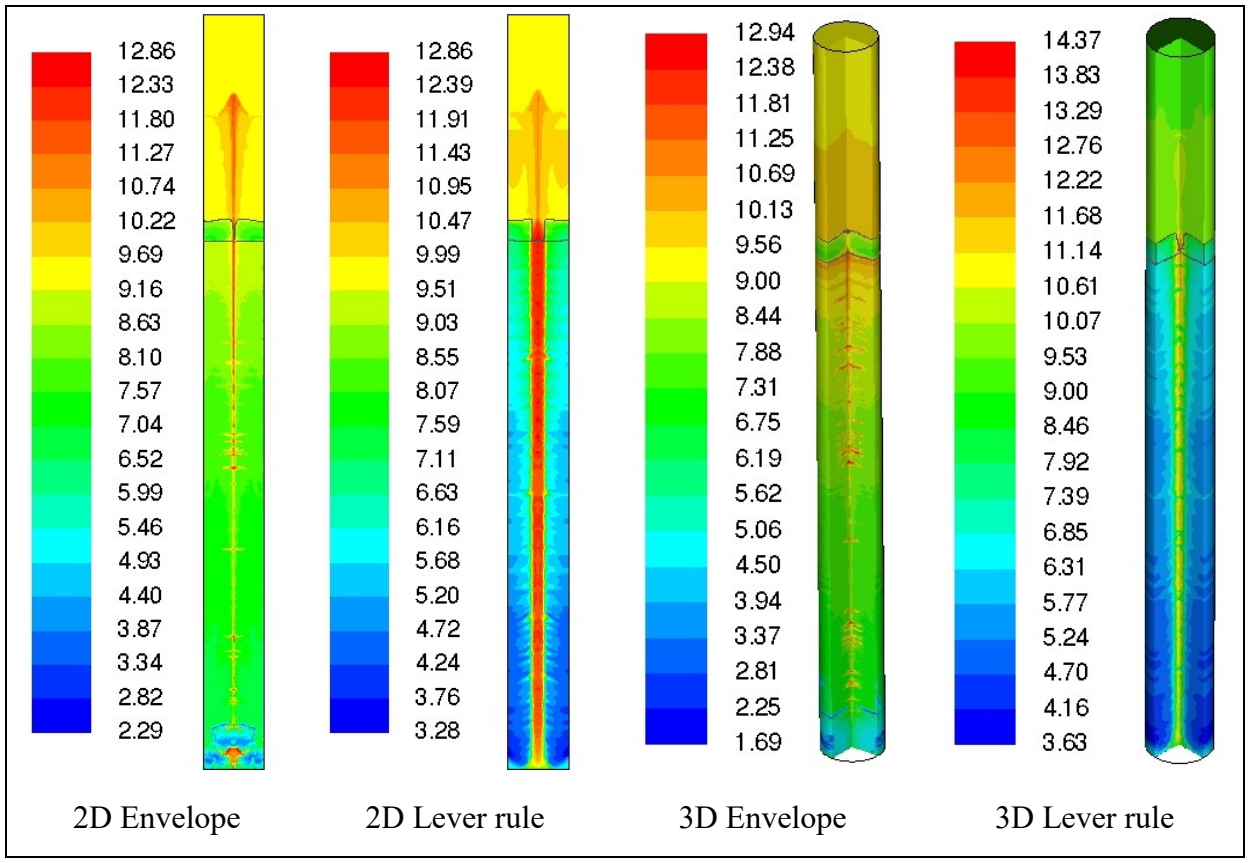

Figure 4.8 Solute distribution [wt.% Si] at 840 seconds of flow time – auto range

To catch more differences, identical colormap ranges were set on Figure 4.9 and Figure 4.10. Different levels are showing more and less details for Envelope model and Lever rule cases, which is a proof for different results.

Such difference can be proven if the comparison is done with the measurement using concentration mapping. The same surfaces were made in Fluent for all cases and the same averaged values were collected as described in chapter 2.3.1. 3 sample sections were available, and the same sections were checked in Fluent. The average values were exported, and the data matrices were visualized using Matlab 2013b. The results are presented on Figure 4.11 to Figure 4.13. Lever rule is correlating better based on visual inspection of the contour images.

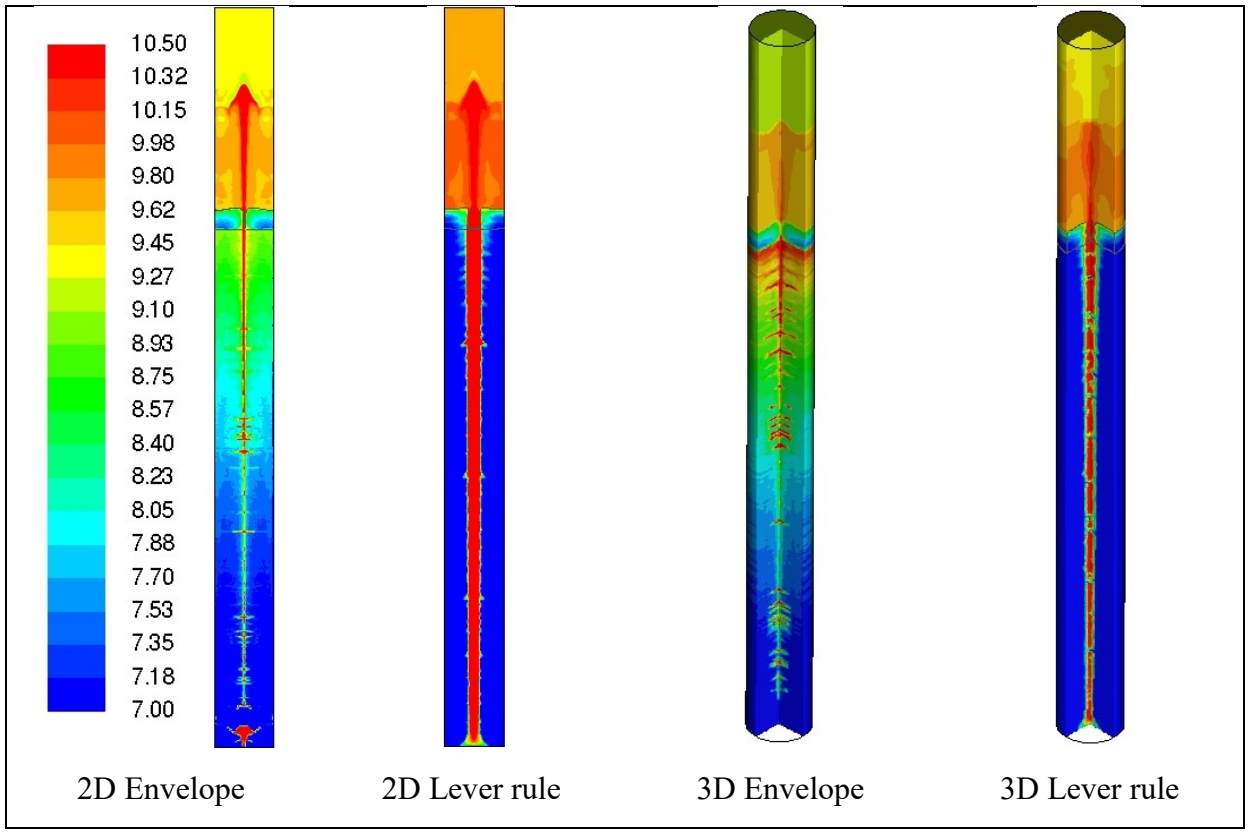

Figure 4.9 Solute distribution [wt.% Si] at 840 seconds of flow time
Colormap range: 7-10,5 wt.%

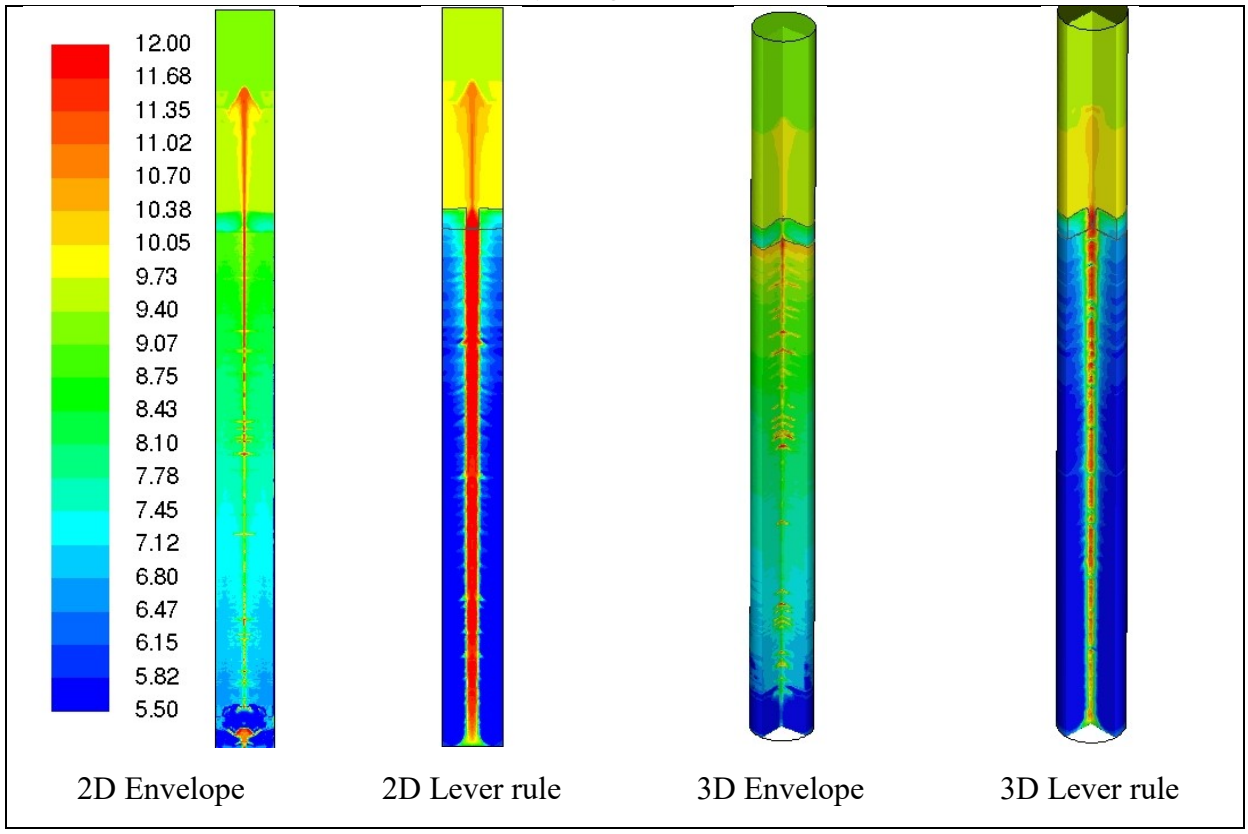

Figure 4.10 Solute distribution [wt.% Si] at 840 seconds of flow time
Colormap range: 5,5-12 wt.%

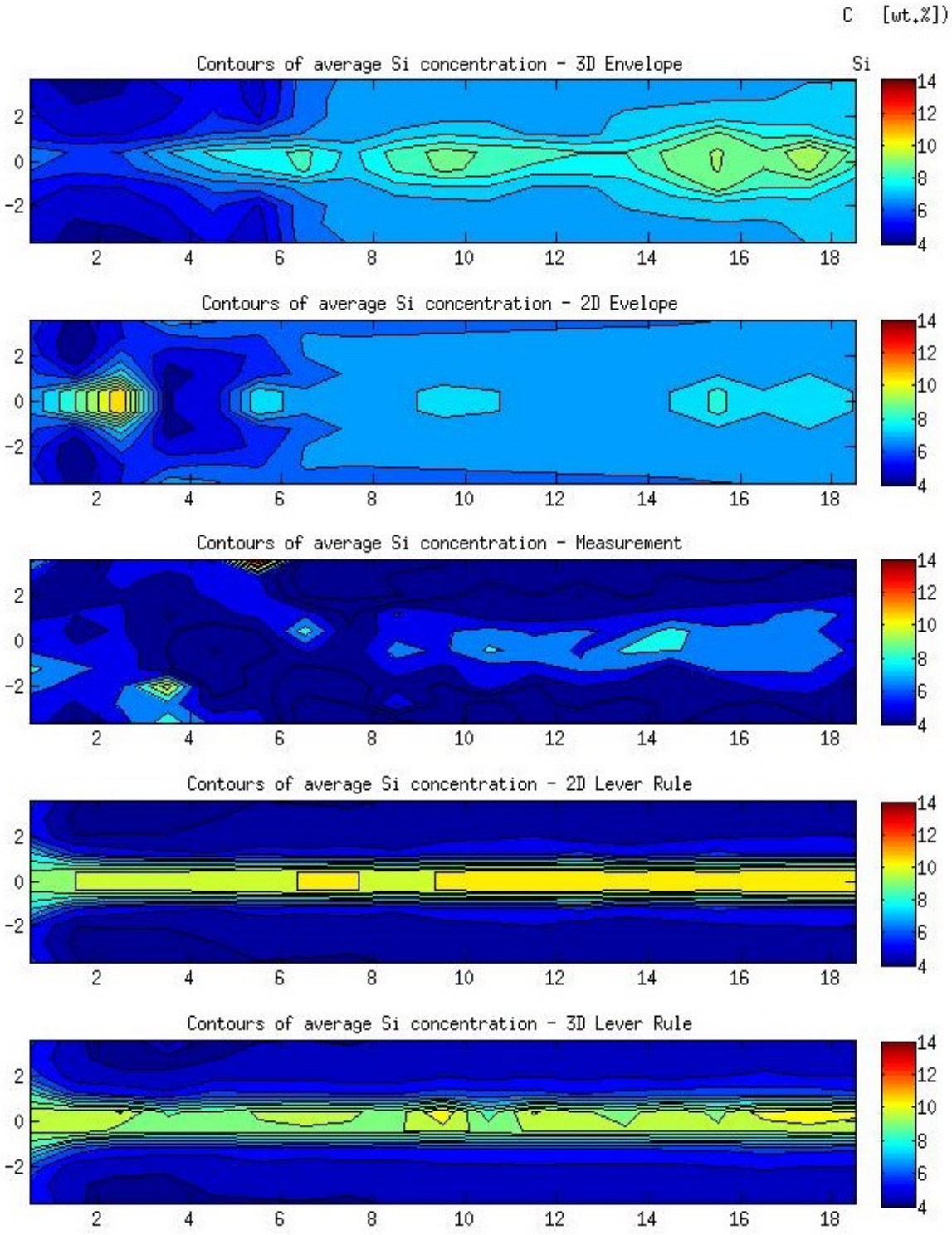

Figure 4.11 Solute distribution comparison – section 1

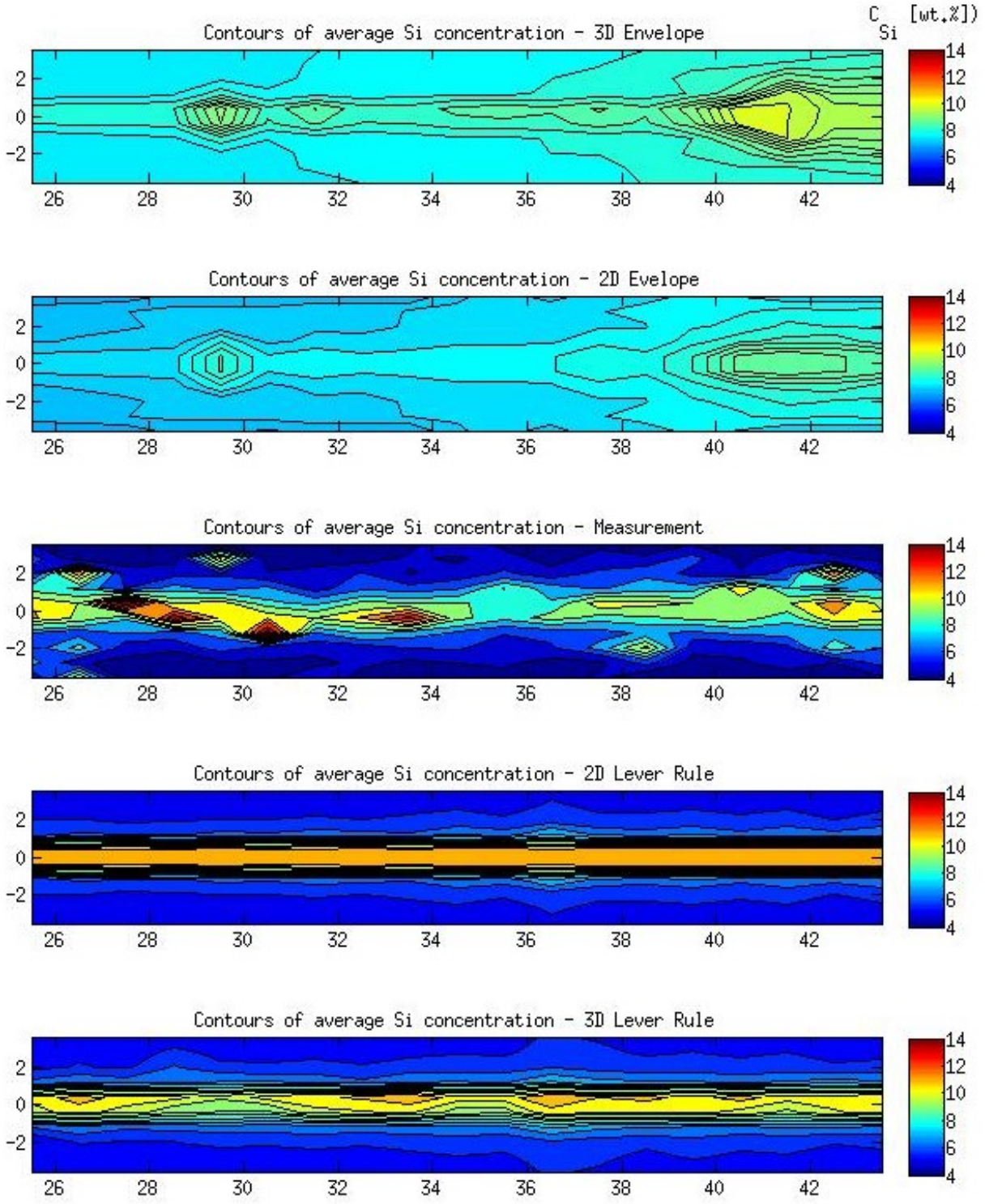

Figure 4.12 Solute distribution comparison – section 2

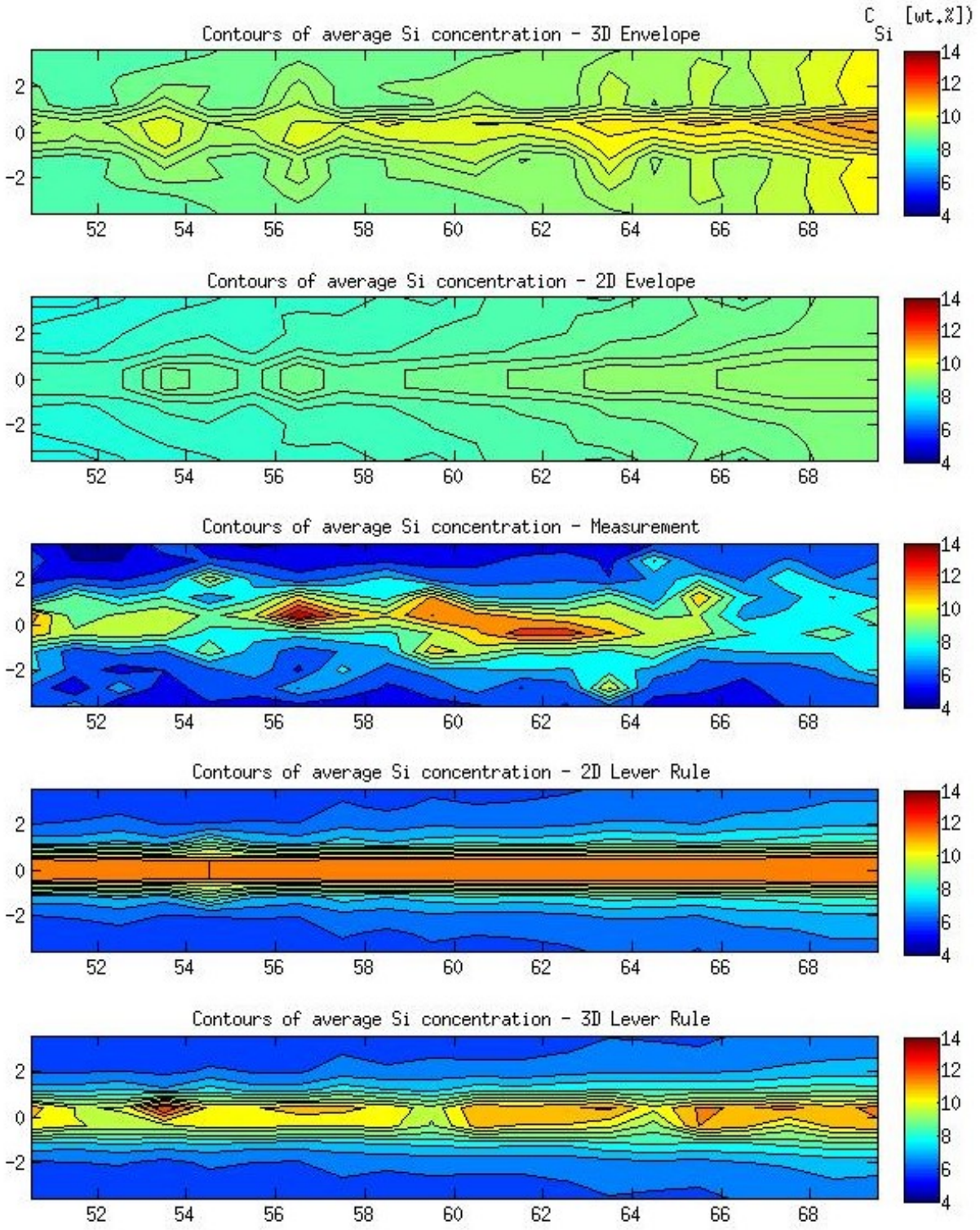

Figure 4.13 Solute distribution comparison – section 3

If real validation needs to be done, quantitative comparison must be performed. Figure 4.15 presents plotted result of the areas. 3,6 mm represents the average values plotted one after another from the measuring windows close to the wall. 0,4 mm is related for the inner section – Figure 4.14. Since the measurement show rather high fluctuation, the trends are presented separately. Accumulation of the solute towards the top of the sample is visible on all the cases, like in the measurement results, but both Envelope models suggest different radial distribution of Si.

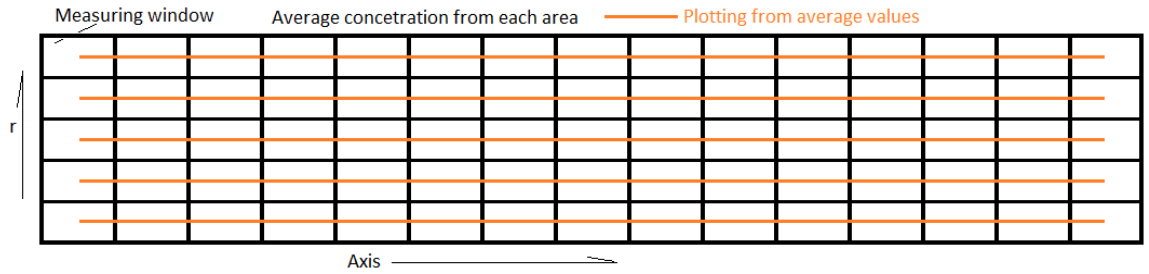

Figure 4.14 Plotting explanation

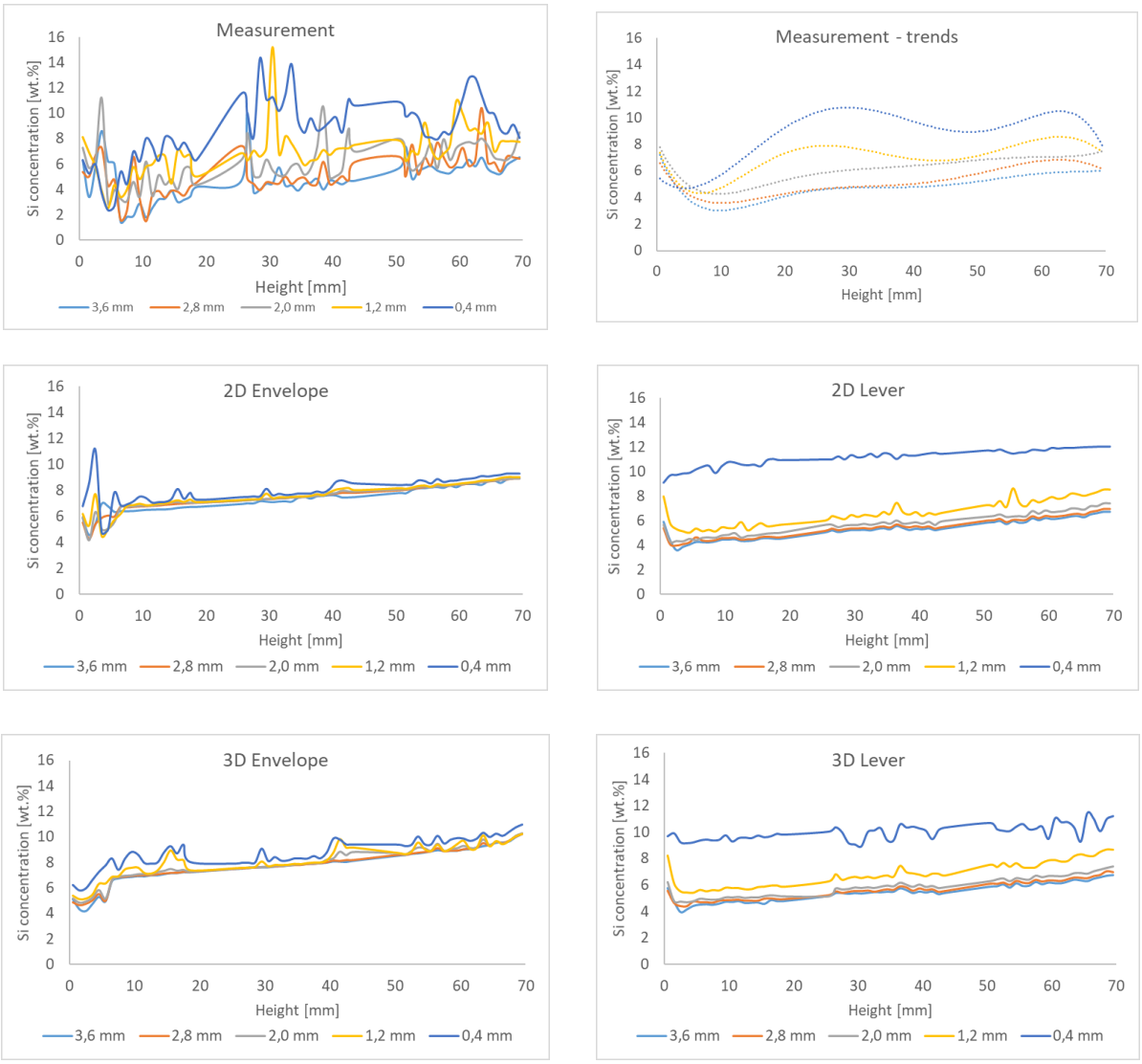

Figure 4.15 Si concentration plots based on the area avg. of the measuring windows

Radial Si distribution in all cases are presented on Figure 4.16. Lever rule models are correlating better with the measurements; however, Envelope models are hardly showing central accumulation. The difference can be proven with Figure 4.17.

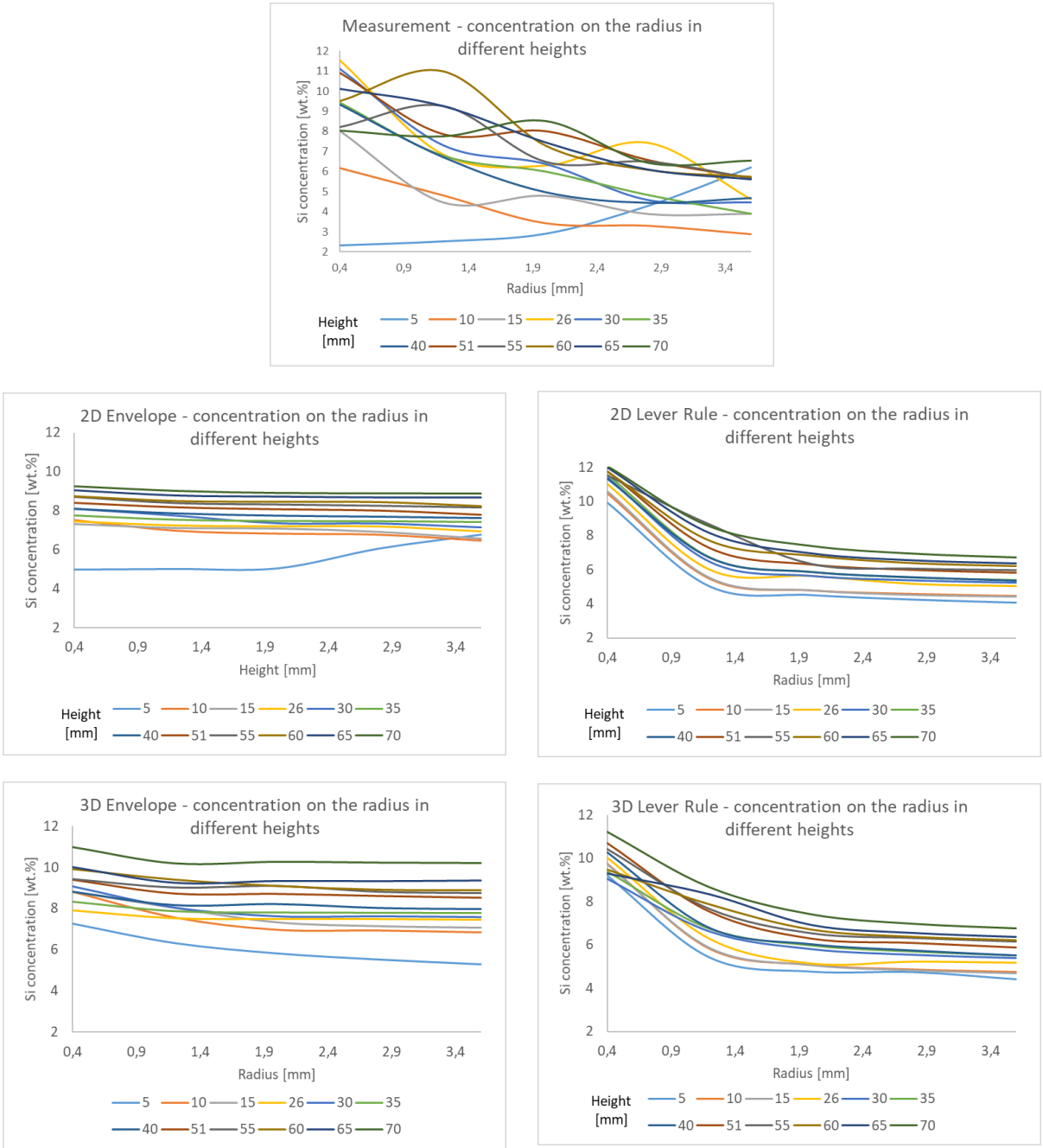

Figure 4.16 Si concentration distribution along the radius in different heights

Lever rule models are clearly close to the measurement results. In cases like 2,8 mm or 2,0 mm, the simulation data of lever rule models could be treated as trendlines; however, Envelope models provide higher concentration values in all positions.

Figure 4.17 Si concentration distribution in different radial positions for all models and measurement

Before summarizing the RMF simulations, the resulting volume average Si concentration should be inspected – Figure 4.18. the initial concentration was 7 wt.% which can change if the models have calculation problems. The conservation of the solute is instable in case of Envelope models, despite the results of Envelope, where the average concentration is rather perfect.

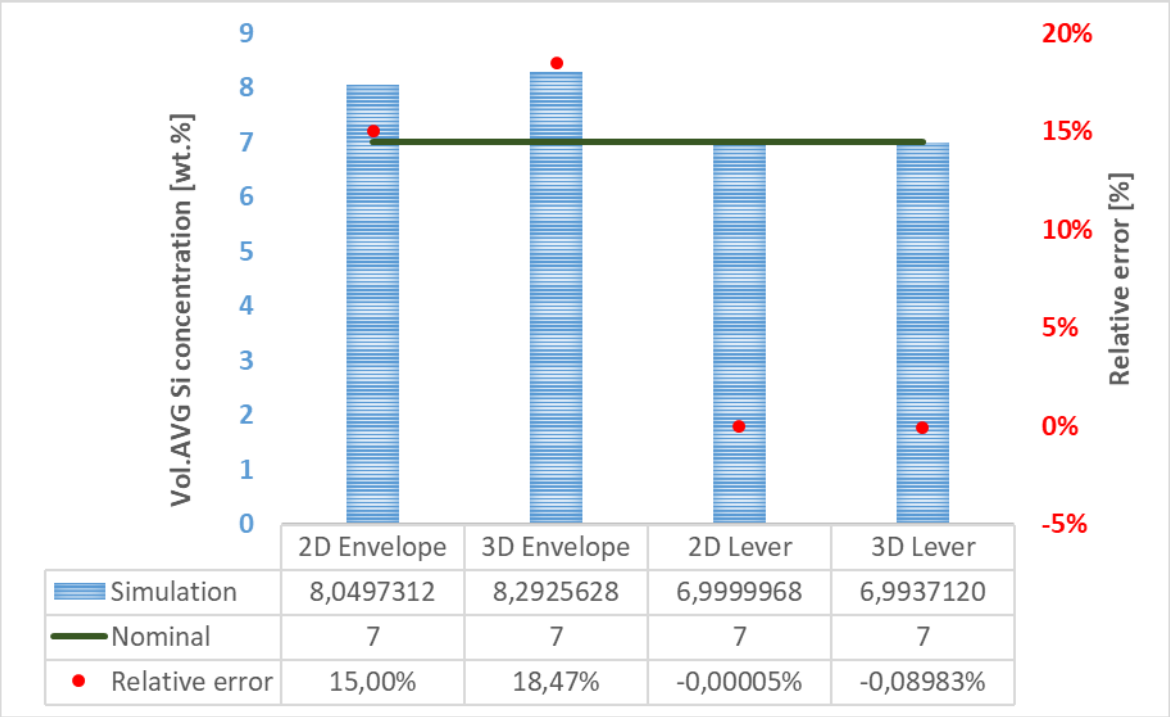

	2D Envelope	3D Envelope	2D Lever	3D Lever
Simulation	8,0497312	8,2925628	6,9999968	6,9937120
Nominal	7	7	7	7
Relative error	15,00%	18,47%	-0,00005%	-0,08983%

Figure 4.18 Final volume average Si concertation for all the 4 cases

4.4.4. Conclusions on RMF simulations

Regarding the four presented simulations the following statements can be done:

- In point of view of 2D vs. 3D cases, no significant difference appears. Since the flow field is quasi-axisymmetric, there is no real advantage of building up a more robust case which requires higher calculation resources and longer time.
- In point of view of solute distribution, the Lever rule is more stable and realistic since:
  - The concentration distribution has clearly better results in the Lever rule based model. The fish scale / Christmas tree macrosegregation is reached in all cases, but the higher central Si content is hardly appearing in the comparisons with Envelope models.
  - The solute accumulation is natural in the experiments, although the Envelope model has higher rejection into the liquid. The final conservation of the solute is incorrect. On the other hand, Lever rule is conserving concentration very well.

4.5. TMF simulations

4.5.1. Preparation for solidification simulation

4.5.1.1 Lorenz Force Filed – RMF

The induced Lorenz force field is an essential part of the system which needs to be simulated. In case of RMF, one simple equation and some technical parameters are needed. The already mentioned equation is used:

$$F_L = \frac{1}{2}\sigma B_0^2 r(\omega_0 - \omega)$$

Where:

- σ is the electrical conductivity of the melt
- B is the magnetic induction
- r is the actual radius (or distance from the axis)
- ω_0 is the synchronous angular velocity of the inductor
- ω is the actual angular velocity of the melt

Using such a simple equation and correct data behind, a well-known flow field can be achieved (see result above).

4.5.2. Simulation series for the TMF Lorenz force field

4.5.2.1 Electromagnetic

If we turn to TMF, the case changes significantly. The unique system is very complicated, and no direct parametric equation is accessible right now. To be able to do proper flow and solidification simulations, electromagnetic calculations had to be done. Comsol Multiphysics 4.4 was used. Limited geometrical and technical parameters were available about the inductor:

• Height of the inductor	h	580 mm
• Air gap between the two heads	d	130 mm
• Number of coils	Ncoil	2x12
• Sample bottom – inductor bottom distance	ysample	302 mm
• Height of the sample	hsample	116 mm
• Diameter of the sample	dsample	8 mm
• Pole pitch	τ	290 mm
• Frequency	f	50 Hz
• Synchronous velocity of the TMF	vSB	29 m/s

The polynomic functions for the components- and resultant value of the induction and sketch of the magnetic fluxes were also shared, which were used for validation purposes.

A very simplified geometry was made including:

- Sample: Ø8*100 mm cylinder
- 2x12 coils: 20x30x100 mm (H x W x L)
- 2 yokes: 100 mm wide
- Air around the system

The geometry can be found on fig…. Based on the electro technical data, a 6-phase alimentation has been applied – Figure 4.19. J0*2pi/6 means:

$$J = J_0 * (cos\, 2\pi/6 + i * sin\, 2\pi/6)$$

Where J0 is the maximal current and i is the imaginary part. The wall of the outer domain was set for complete insulation.

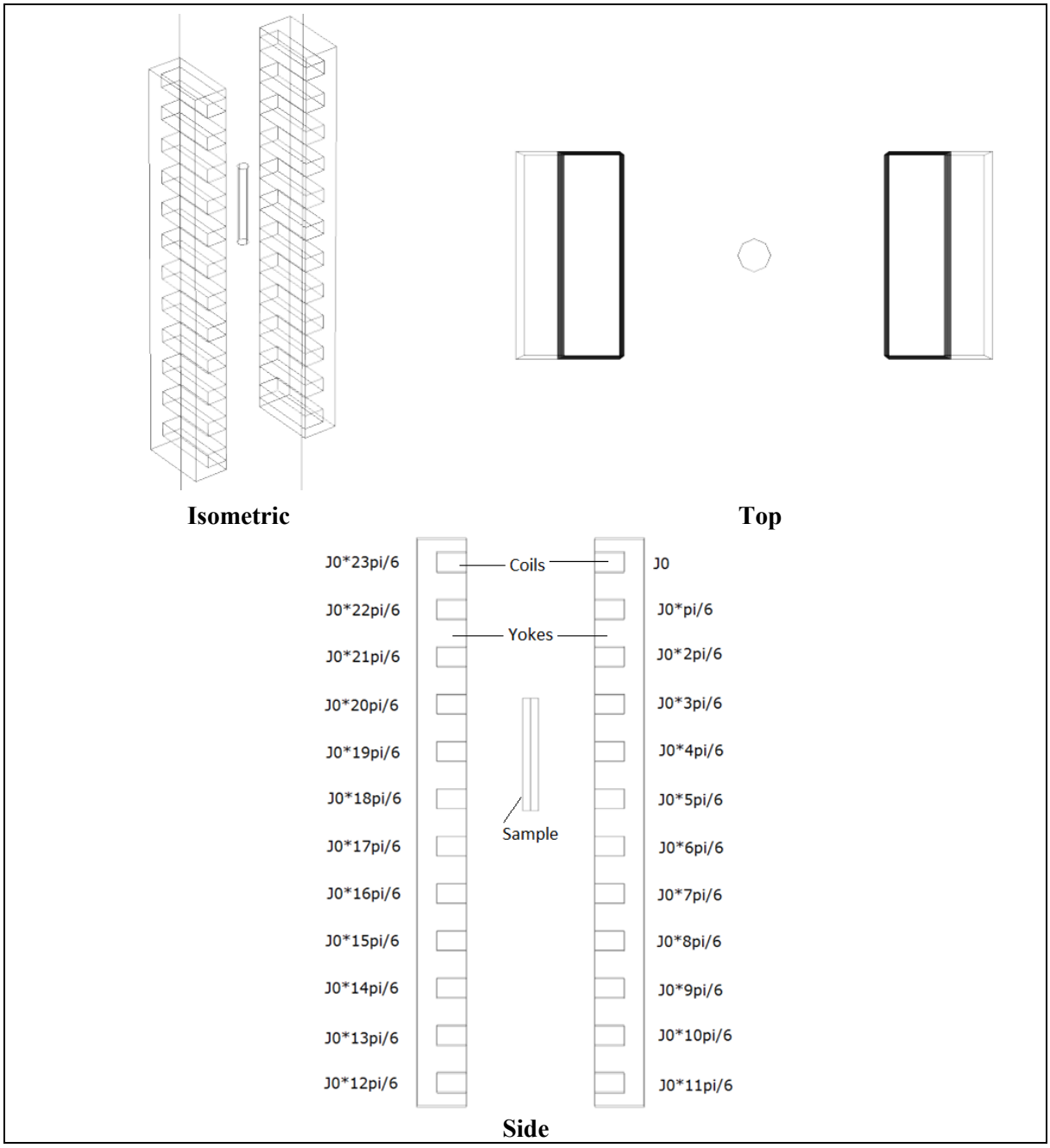

Figure 4.19 The geometry of the electromagnetic simulations on TMF including the phases of alimentation

Table 4.2 Properties of the used materials

	Air	Copper	Steel	Al melt
Electrical conductivity [S/m]	5e-15	5,96e7	2,97e6	2,95e6
Relative permeability [-]	1	0.999994	4000	1
Relative permittivity [-]	1	1	1	1

The properties were set from Comsol's own library, except the electrical conductivity of Al melt, which is coming from [1]. The Copper was used for the coils, steel was for the yokes, Al melt was the sample and air was the environment.

Automatic fine mesh was used – constructed by Comsol and steady state calculations were done self-iteratively for reaching 5, 10, 20, 40 mT resultant induction.

4.5.2.2 Results of the electromagnetic simulations

The fluxes of magnetic field can be seen on Figure 4.20.

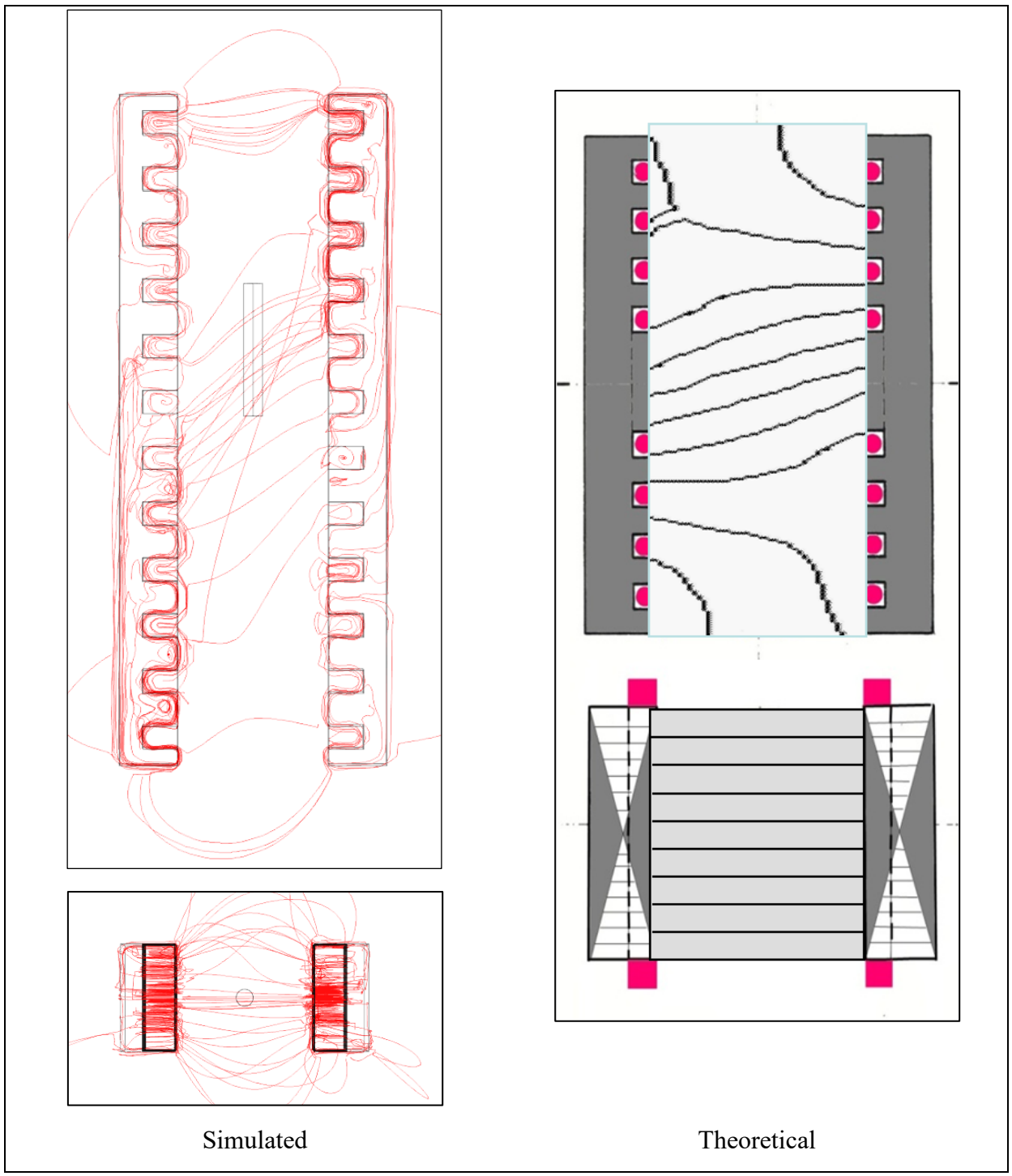

Figure 4.20 Fluxes of magnetic field – simulated and theoretical

Qualitatively the results are acceptable. The simulated magnetic induction on a vertical (from 160 to 420 mm height at the center) line is presented in Figure 4.21 and Figure 4.22.

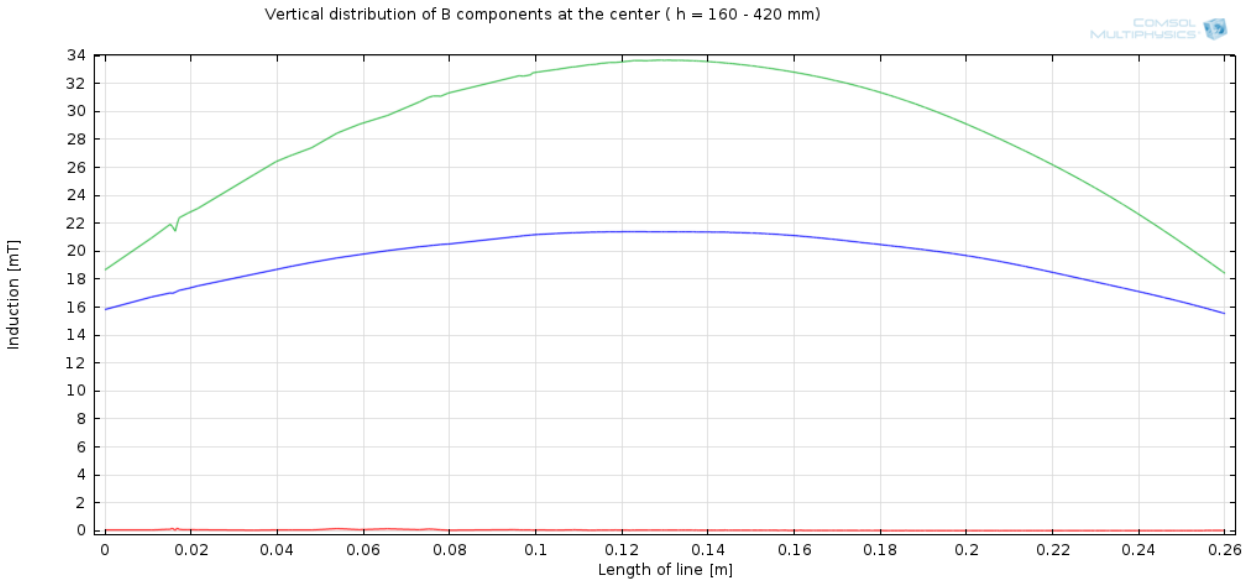

Figure 4.21 Vertical distribution of the magnetic field components at the center of the inductor (red: z, green: x, blue: y coordinate)

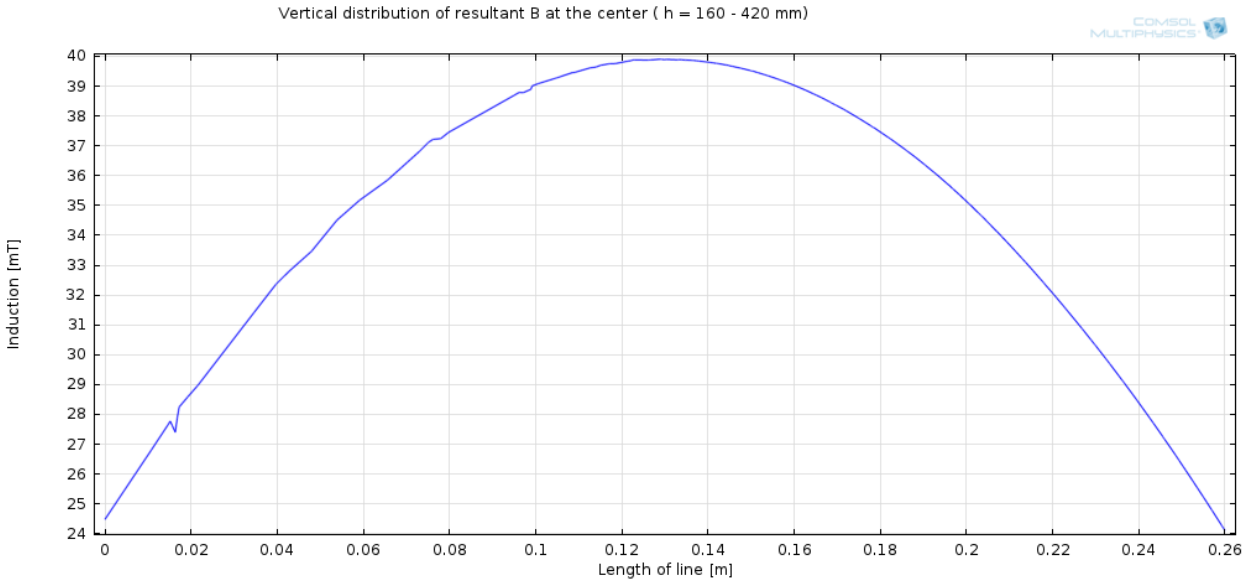

Figure 4.22 Vertical distribution of the resultant B at the center of the inductor

The distribution of the magnetic induction is not completely the same as in the measurements. The maximum and its position are identical, but the minimum values are higher. Regarding such case, the Lorenz force is stronger than the real, since the induction is stronger and as a result, a stronger flow will be reached.

The Lorenz force field for 40 mT case is presented on Figure 4.23 using vectors and contour plot also.

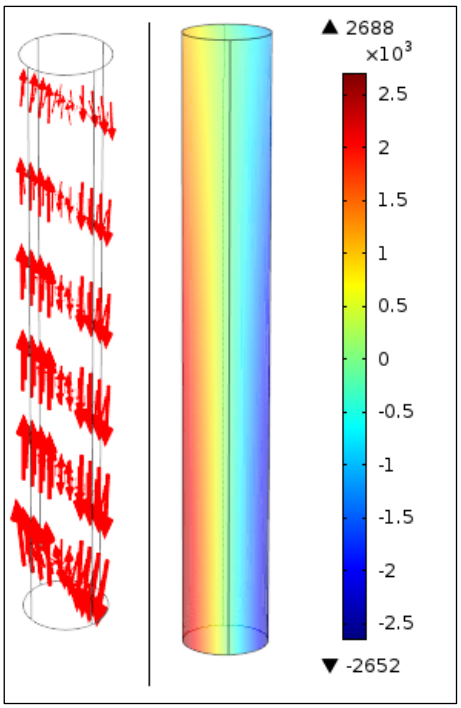

Figure 4.23 The Lorenz force field of 40 mT case – Vectors and contour plot [N/m^3]

The form of the field is identical in all cases – just like the induction – but the magnitude changes. The relation between the induction and the Lorenz force is presented on Figure 4.24.

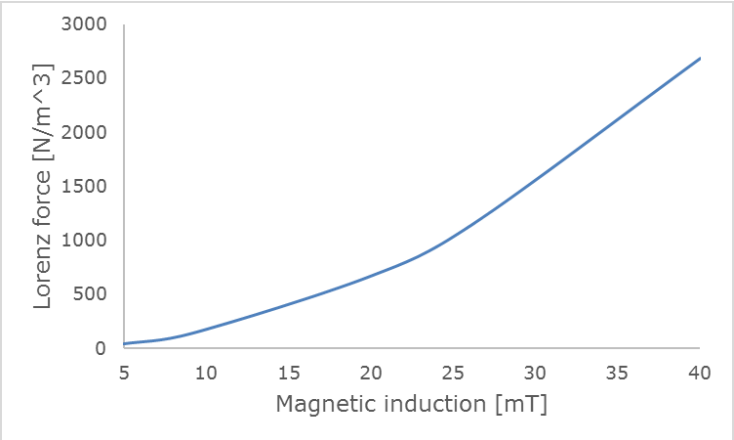

Figure 4.24 Maximal Lorenz force as a function of maximal magnetic induction

Since not enough information was available for the true validation of the electromagnetic simulation, the above-mentioned thermal effect (Chapter 2.3.2) was used in Fluent.

4.5.3. Validation of the Lorenz force field in the TMF system using the thermal effect

The thermal effect occurring at the moment of switching the stirring on or off can be a really good point of validation. The effect is simple, as was described before. The stirring can mix the relatively cool liquid with the hotter as strong, as it can be recorded using the thermocouples on the sample holder assembly. One can find that the effect is depending on the strength of the magnetic mixing. If the correct thermal system is built up for the non-stirred case, the shift in the gradient can be simulated and likewise, the flow behavior can be validated – which is driven by the Lorenz force field exported from Comsol.

For such a study, two simulations had to be done in Fluent. The first was related to calculate the heat flux coming from the furnace wall to apply the stationary thermal equilibrium. In other simulations, the temperature dataset of the thermocouples is applied on the crucible wall as fixed boundary condition, but now the temperature shift needs to be measured on the same wall – then a workaround is needed. This model can be set up and validated with the stationary case's dataset (Figure 2.15 in chapter 2.3.2.1). The measured and calculated temperature is applied on the furnace wall (for visual explanation see Figure 4.27 in chapter 4.5.3.1) and the heat flux developing on the sample holder's inner wall is exported for future calculations. The validation is done via the measured temperature of the 13 thermocouples.

The second model can have a simplified geometry with only a cylinder as the sample. The heat flux can be imported on the walls just like the Lorenz force field in the volume.

4.5.3.1 Global thermal model for the heat flux

The geometry is presented on figure… The mesh has 31833 mixed mostly quad cells.

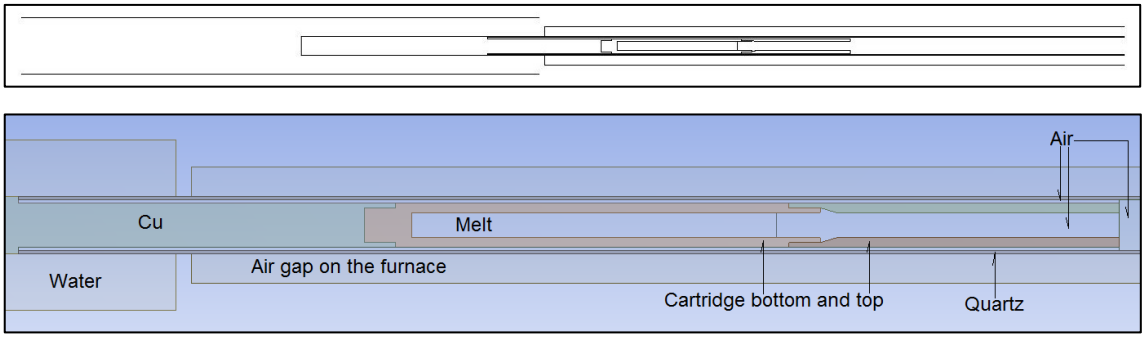

Figure 4.25 The geometry of the global thermal model

The used material properties can be found in Table 4.3.

The same ceramic material was used for the furnace wall and the sample holder, since the exact material of the furnace was unknown. The connection between the copper tusk and the sample cartridge was modified on the walls with 2 mm layer of thermal conductive/contact paste as it happens in the experiments.

The model was steady-state 2D axisymmetric using laminar flow solver, energy equation and Surface to Surface radiation model.

Zero velocity was set for the air everywhere in the geometry. The water was entering at the bottom and leaving at the top of the container. The inlet velocity was set to 0,2 m/s to reach a velocity around 0,313 m/s at the top. The value was computed from Bernoulli equation using 5 mm height of fountain on the top of the water container.

Table 4.3 Material properties in the global thermal model

	Al melt	Al_2O_3 ceramic	Cu	Water	SiO_2 glass	Air	Thermal paste
ρ [kg/m³]	2452	3690	8978	998,2	2200	1,225	2254
c_p [J/kgK]	1140	880	381	4182	700	1006,43	1000
Λ [W/mK]	100	15	350	0,6	1,38	0,0242	1,4
ν [Pa-s]	0,00252	-	-	0,001003	-	1,79e-5	-
ε [-]	-	0,9 (0,97)**	0,5	-	0,8*	-	Not needed

*due to the high level of smoke on the surface

**for furnace wall

The temperature on the furnace wall was modeled using a user defined function (UDF) temperature profile macro. Four different equations were used to get close to the measured temperature distribution – Figure 4.26.

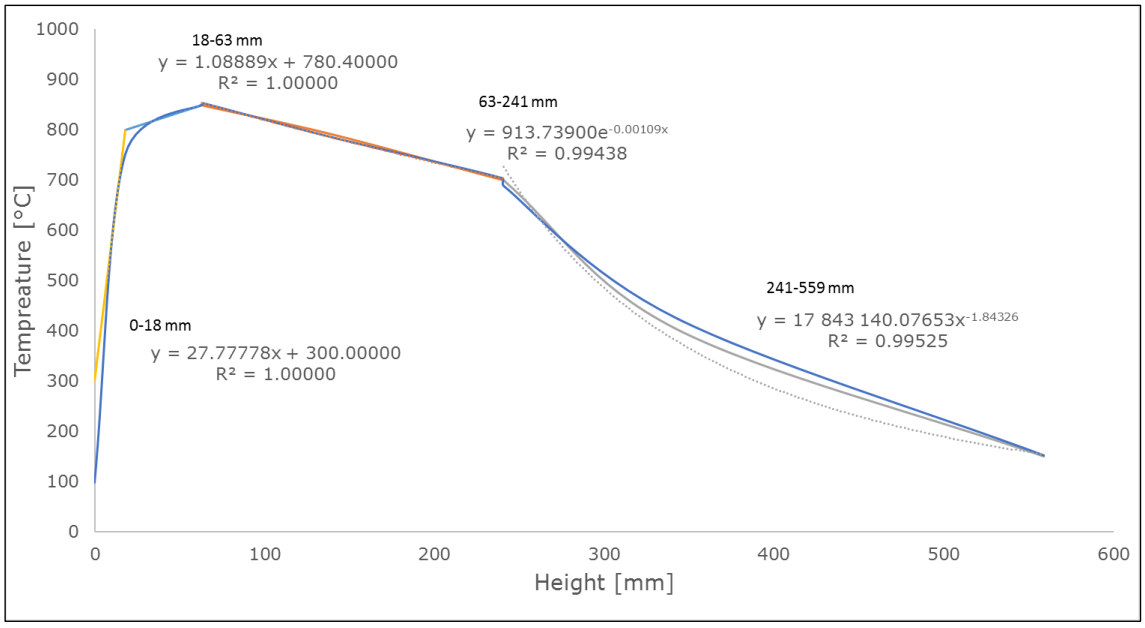

Figure 4.26 Parametric temperature equations for the UDF profile

The temperature distribution is monitored on the wall on the sample crucible, where we can find the 13 thermocouples – Figure 4.27.

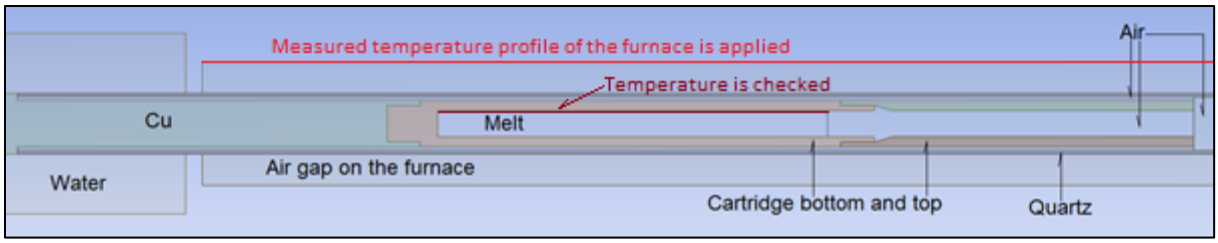

Figure 4.27 Temperature application and measurement in the system

4.5.3.2 Results of the global thermal model

The contours of temperature can be seen in Figure 4.28.

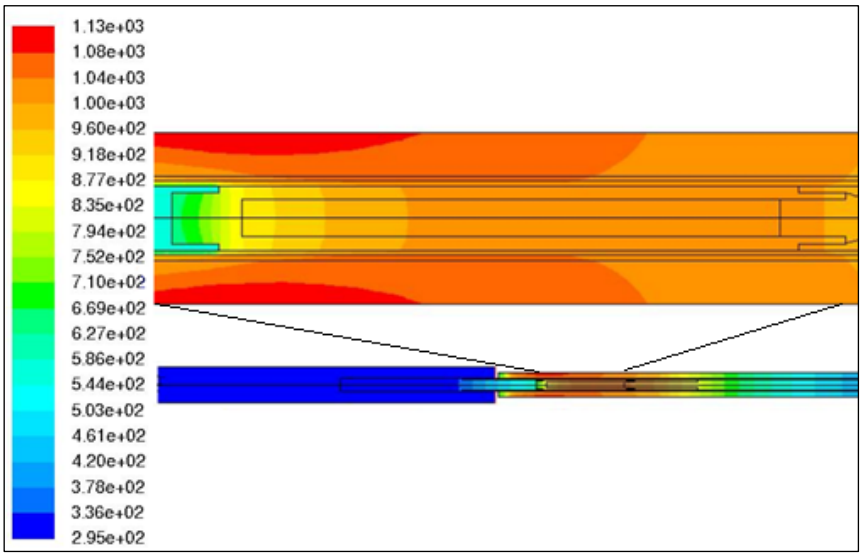

Figure 4.28 Contours of temperature in the global thermal model

The results with relative errors can be seen in Figure 4.29.

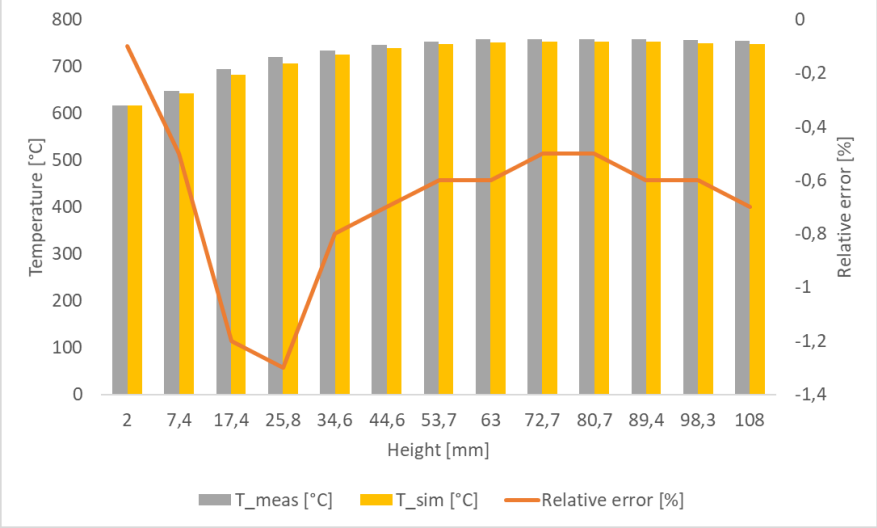

Figure 4.29 Results of the Global thermal model

Some points have a bit high difference from the measurements, but it is still acceptable for later complex simulations, since the flux appearing on the inner wall of the crucible is used.

The input temperature distribution and the resulting can also be compared visually which gives a great result. The thermocouple lying on the highest point has equal temperature as the furnace. The simulation has same results – Figure 4.30.

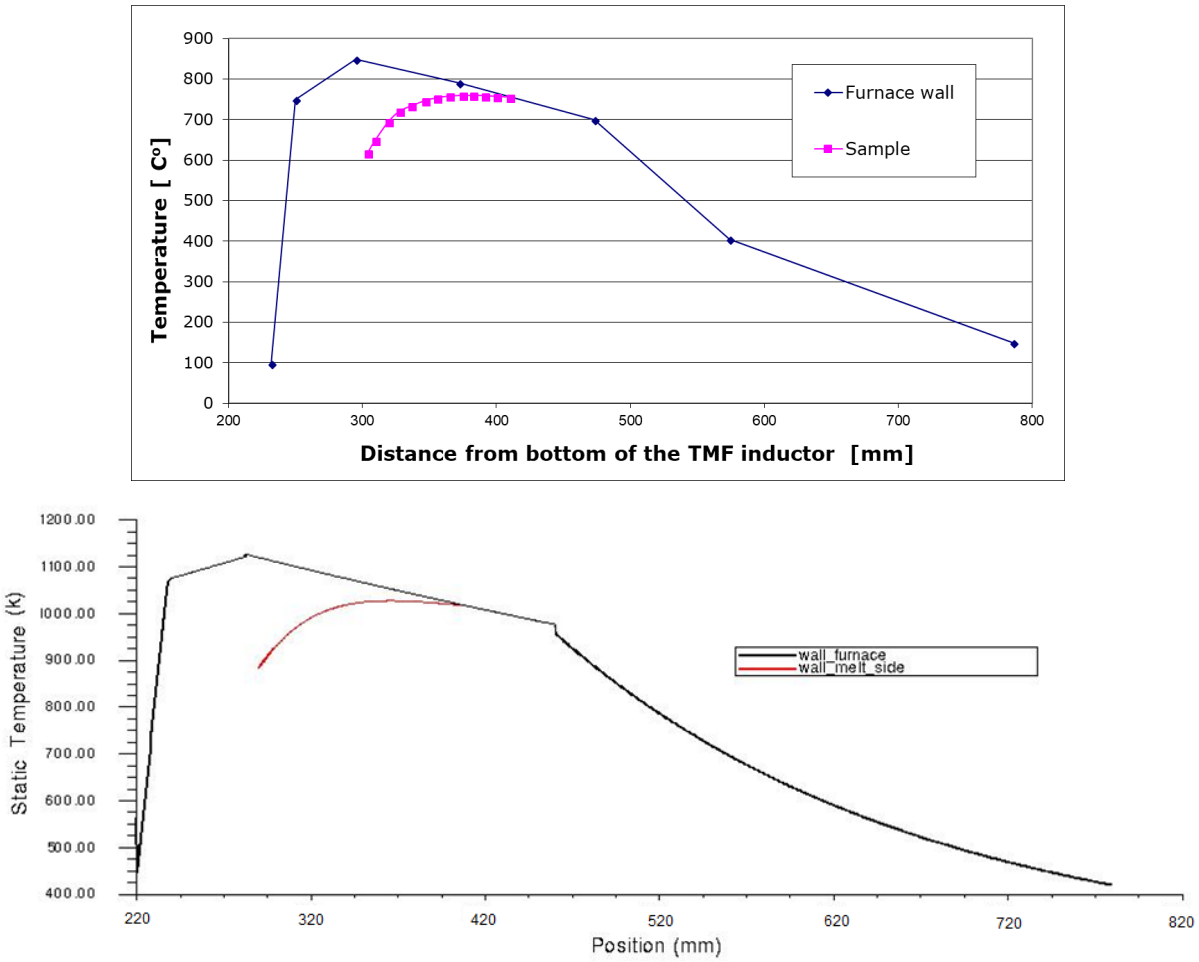

Figure 4.30. Measured (top) and simulated (bottom) temperature distribution

4.5.3.3 Thermal flow model for validating the Lorenz force field

Due to the nature of the flow, 3D model was prepared. A single cylinder was used – Ø8x116 mm. Full hexahedron mesh with 608600 cells was provided. The ceramic wall and the aluminum melt had the same material properties as in the global thermal model. Since the experiment was performed with pure Al, the simulation was did with the same unalloyed material.

The model was transient with laminar flow solver and energy equation. No radiation was used. The heat flux of the walls of the sample holder crucible in the global model was interpolated on the wall of the crucible in the current system to achieve the same thermal system.

The momentum source for the TMF Lorenz force field is added with some more steps. The coordinates and shape of the cells are very different in Comsol and Fluent. To be able to get the best values for the force field, the mesh cell centroids were exported in a data file which was used in Comsol to interpolate, then export the correct force field values for every cell. The time average of the Lorenz force is used in all cases (considering x, y and z coordinates separately).

The temperature data of the 13 thermocouples were monitored during the calculation to see if the gradient shift occurs properly or not.

The contours and vectors of the 40 mT case can be seen below – Figure 4.31.

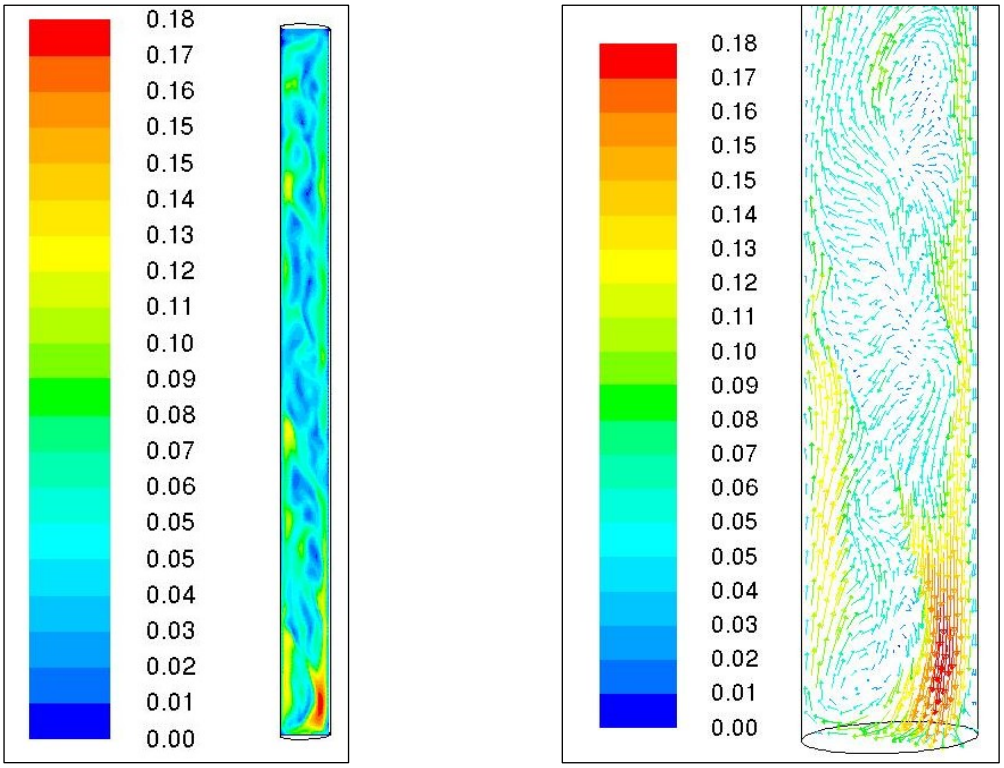

Figure 4.31 Contours and vectors of velocity magnitude – 40 mT, bidirectional stirring

Several trials had to be done to be able to reach sum. 0 W/m^2 heat flux of the crucible – otherwise the thermal equilibrium is not present. More trials were ran to achieve an acceptable result of the thermal effect. The results on Figure 4.31 show much faster flow than should appear, which can be stated based on the first gradient shift result presented on Figure 4.32.

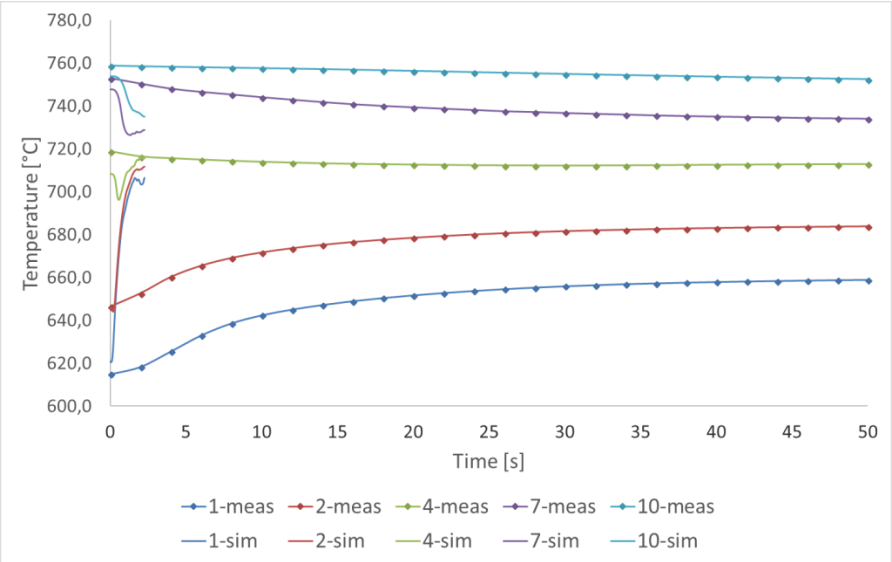

Figure 4.32 First gradient shift result – 40 mT

After adjusting the Lorenz force field with a scaling factor of 0.1, a more accurate result could be achieved – Figure 4.33. The flow turned to a stable laminar form and the maximal velocity changed to 0.04 m/s from 0.18 – as compared to Figure 4.31.

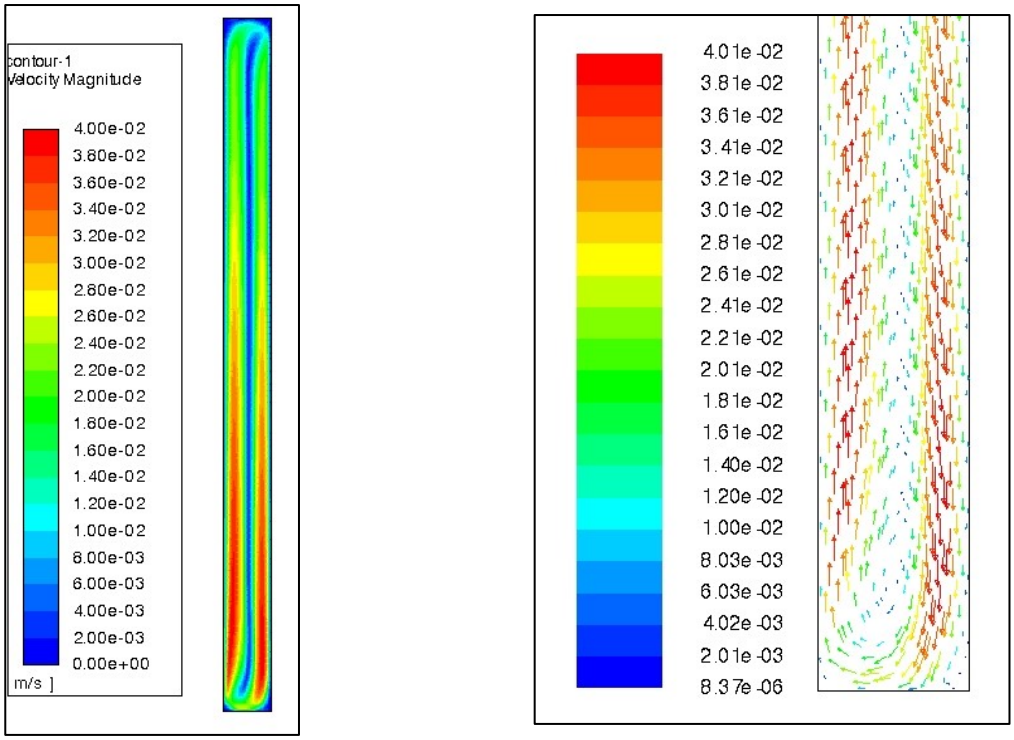

Figure 4.33 Contours and vectors of the flow colored by velocity magnitude

The slower flow has driven us to more accurate results, which can be observed on Figure 4.34. The equilibrium state of the flow arrives much earlier than the thermal steady state. This is related to the slower heat transfer. The current result shows us that the Lorenz Force field and the electromagnetic system can be used if the correct reduction factor is set up. Further adjustments could be done on the 3 recently presented models like:

- Choosing the perfect material properties
  - Heat transfer coefficient, electrical conductivity, density, surface properties, etc.
- Adjusting the dimensions and alimentation of the inductor modeling
- Fine tuning of all the three models separately

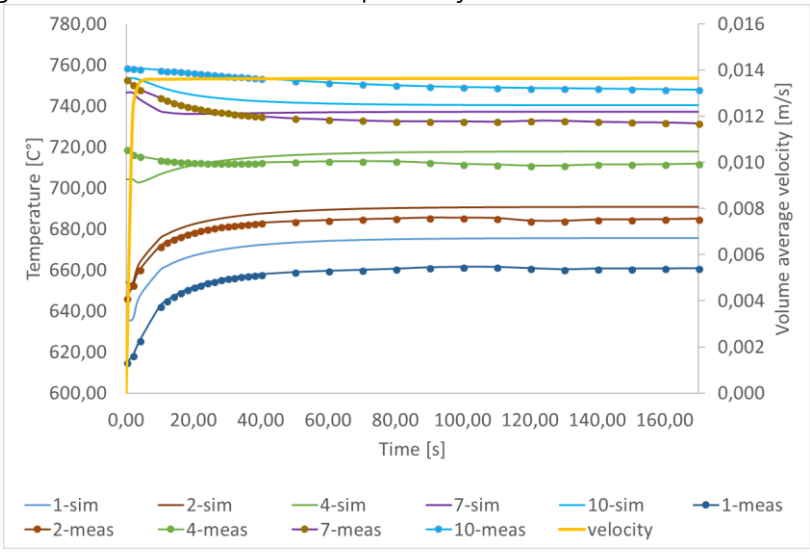

Figure 4.34 Gradient shift after the adjustment of the flow field and settlement of the flow (maximal velocity)

The 20 mT case shows even better correlation with the measurement which can be related to the slower flow – totally laminar case (Figure 4.35).

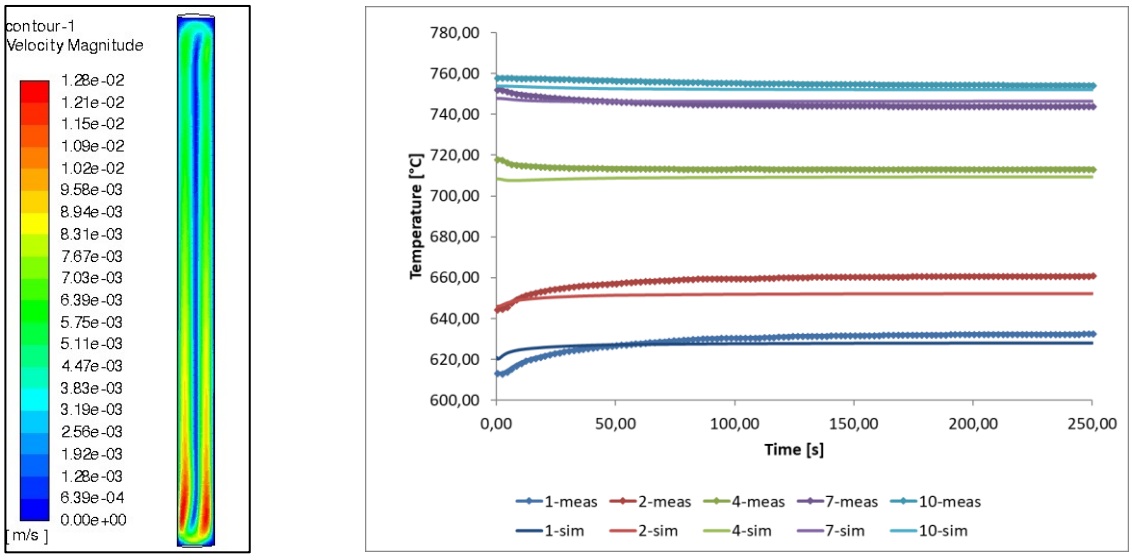

Figure 4.35 Contours of velocity magnitude and gradient shift results in the 20 mT case

4.5.3.4 Summary of the simulation series on TMF Lorentz force field

A simulation series was performed to achieve the Lorenz force field of the TMF inductor, since it cannot be described analytically, and the detailed properties of the system was unavailable.

First, electromagnetic simulation was prepared to achieve the Lorenz force field itself. Since only qualitative comparison was possible with theoretical data, two more simulations were done to validate the electromagnetic results.

The global thermal model of the complete inductor was provided with stationary melt to gather the heat fluxes of the crucible walls.

Finally, the results of the two latter models were combined in a thermal-flow model to reach the thermal gradient shift effect. After the application of the scaling factor, qualitatively and quantitatively correct results were achieved and the usability of the Force field was proven.

4.5.4. Solidification simulation – bidirectional Lorenz force field

4.5.4.1 Setup

One 3D simulation was provided based on the experiment presented in chapter 2.3.2.2 using the Lorenz force field imported from Comsol and the method presented in chapter 3.1.

The model was 3D transient in an Ø8x70 mm cylindric media meshed with 1019110 hexahedron cells. Till the writing of this thesis, the simulation could run till 999 seconds – roughly the half of the sample was solidified.

4.5.5. Flow field

The flow is presented on Figure 4.36 from different angles. The bidirectional mixing appears well, but the flow itself is slow: the maximal velocity is 0.01 m/s.

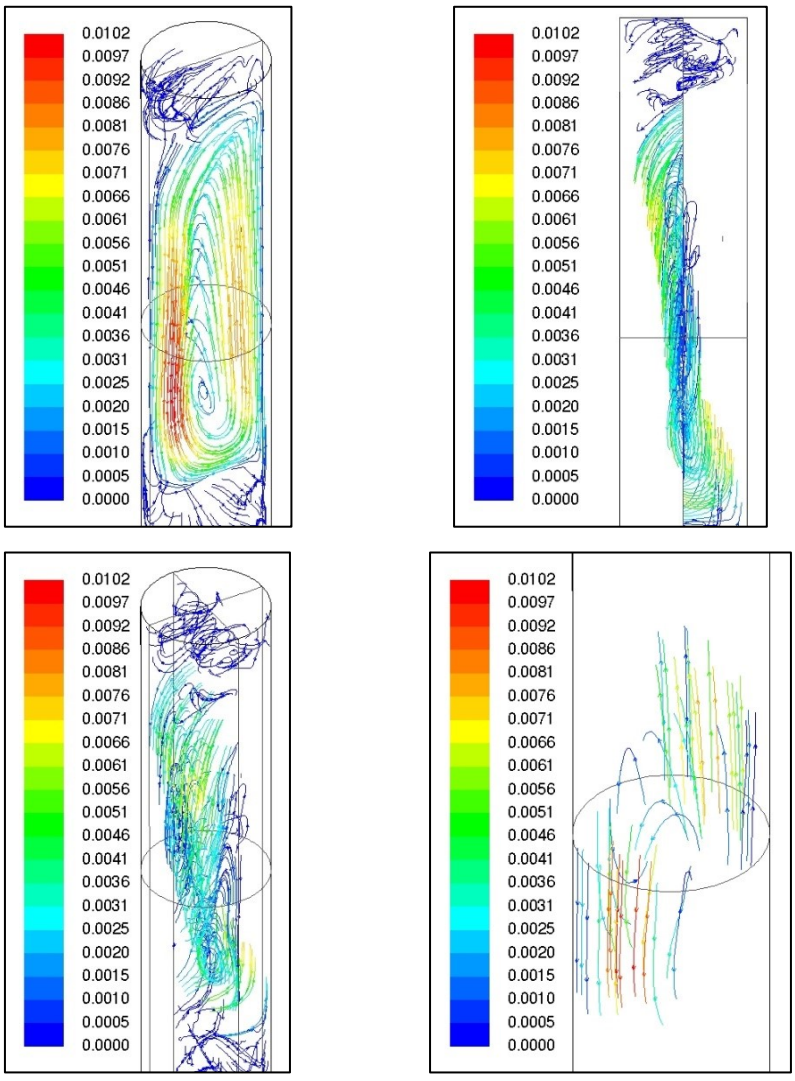

Figure 4.36 Flow field of the bidirectional TMF model – 20 mT, 50 Hz – when 50% of the part is solidified

4.5.5.1 Solute distribution

The distribution of Si on various surfaces is presented on Figure 4.37.

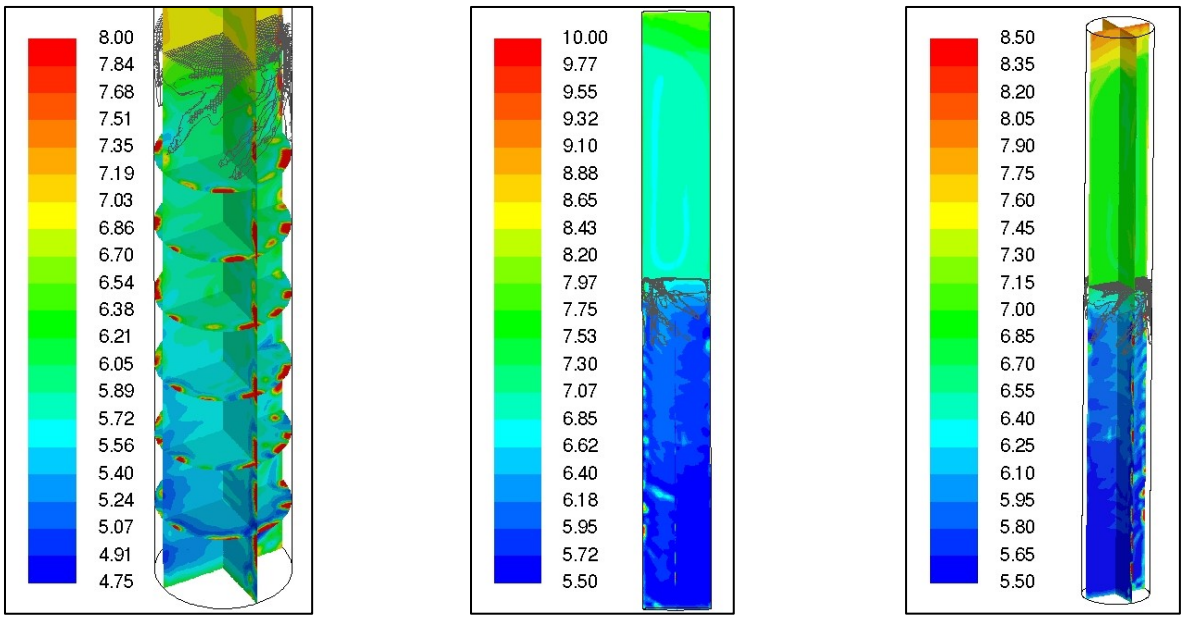

Figure 4.37 Si concentration distribution

Since the measurement contains one cross section and one parallel section, and due to the nature of the flow field, cross sections are compared for Si and Fe distribution. The reference for the up- and downward flow is presented on Figure 4.38.

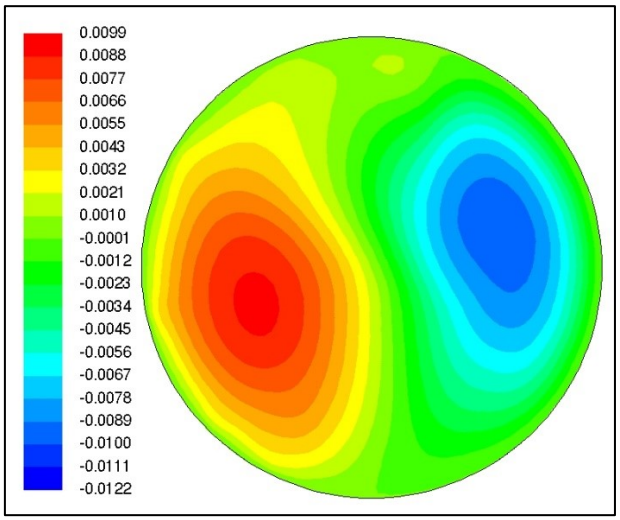

Figure 4.38 Contours of axial velocity [m/s] in an arbitrary cross section
Provided for comparison purposes only

Figure 4.39 and Figure 4.40 present solute distribution (Si and Fe) on cross sections at 5, 10, 15, 20, 25 and 30 mm height. The concentration distribution is similar as it was seen in the texture image – the effect of the flow appears in this model also.

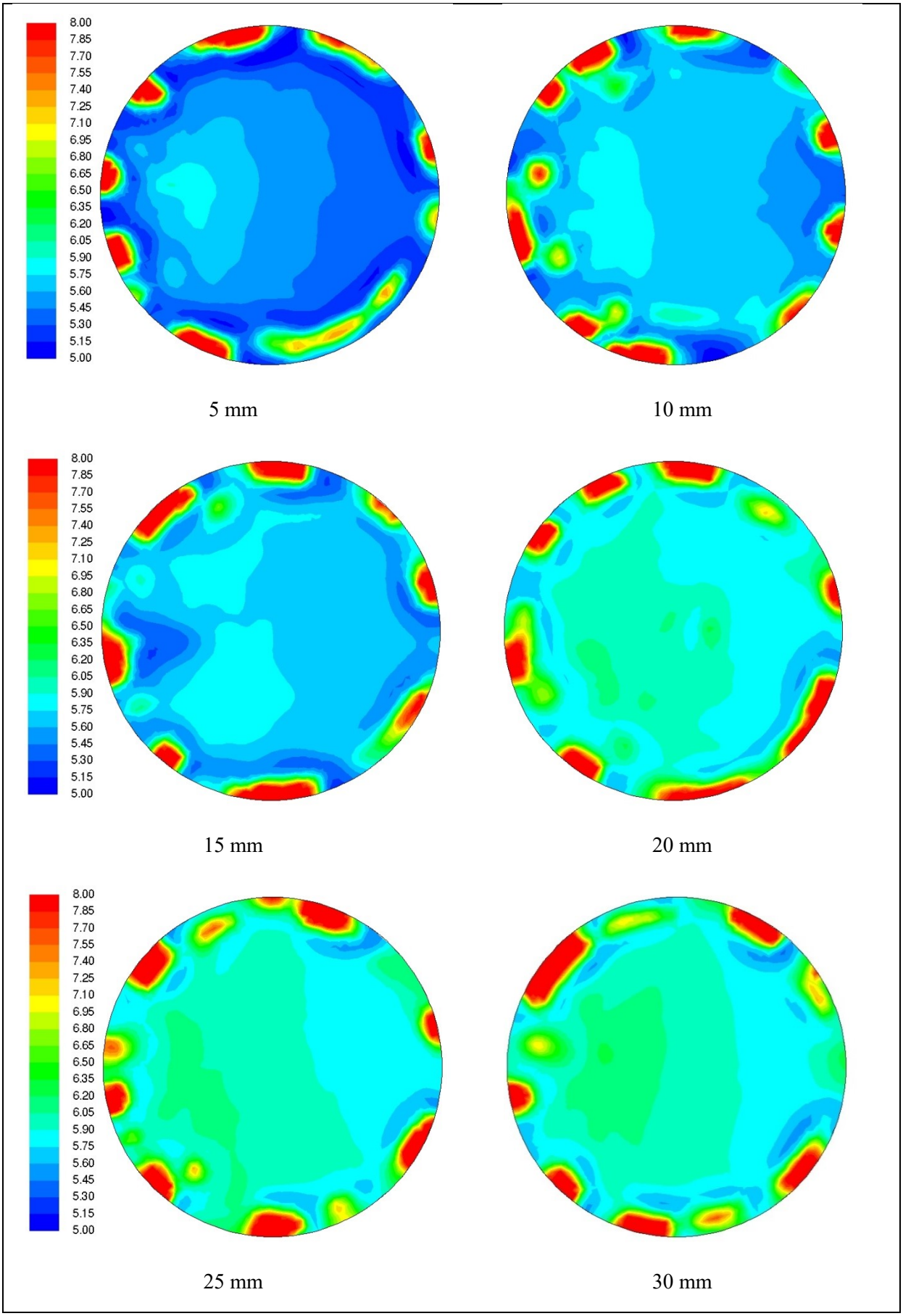

Figure 4.39 Si concentration distribution in different cross sections

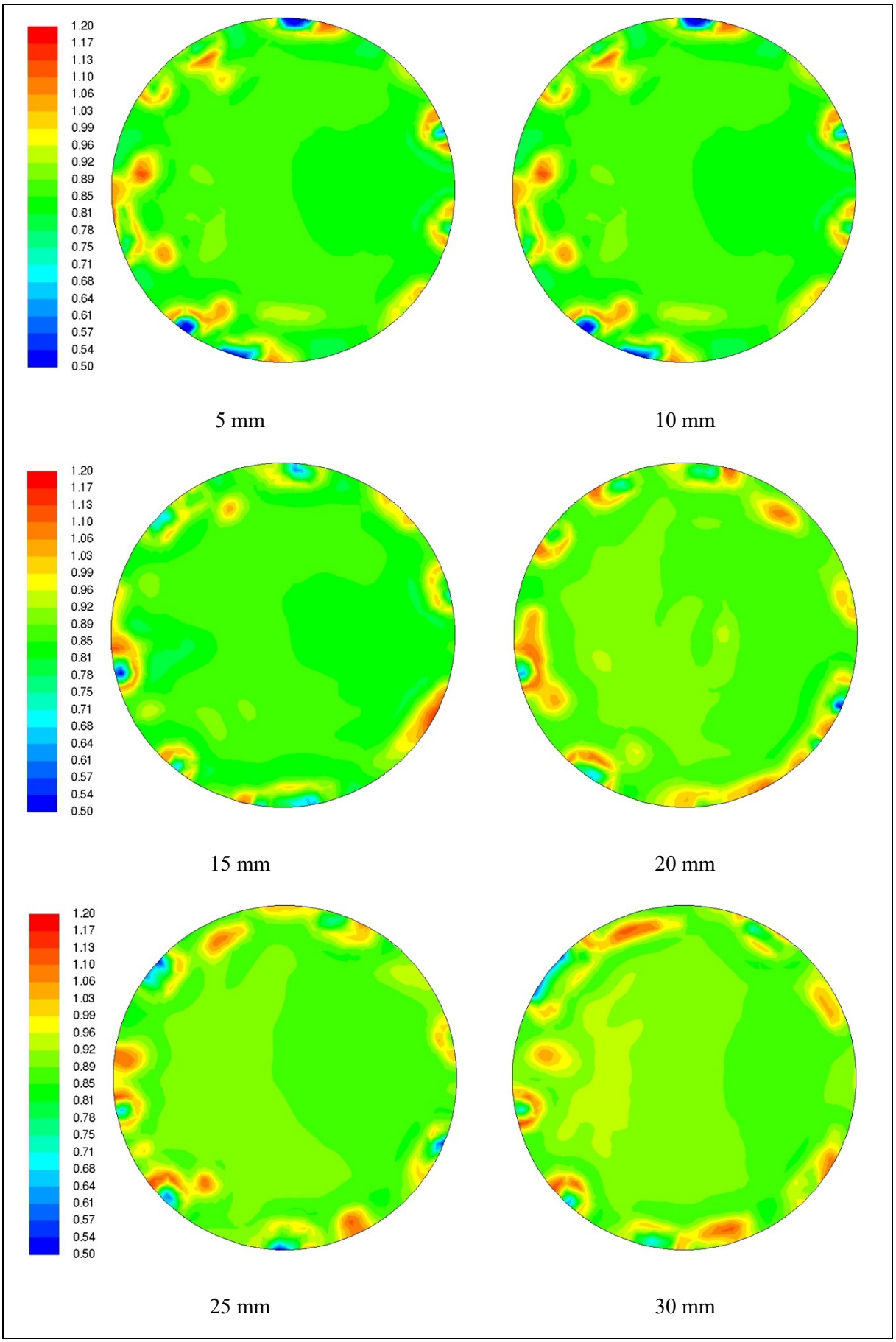

Figure 4.40 Fe concentration distribution in different cross sections

On Figure 4.41 the Si concentration distribution (on 30 mm) is compared with the texture image of the measurement (actually from 90 mm height). The simulation could not be finished to reach the 90 mm height, therefore qualitative comparison was possible only – and the results are promising, since the qualitative correlation is clear. The effect of primary and secondary flow is visible.

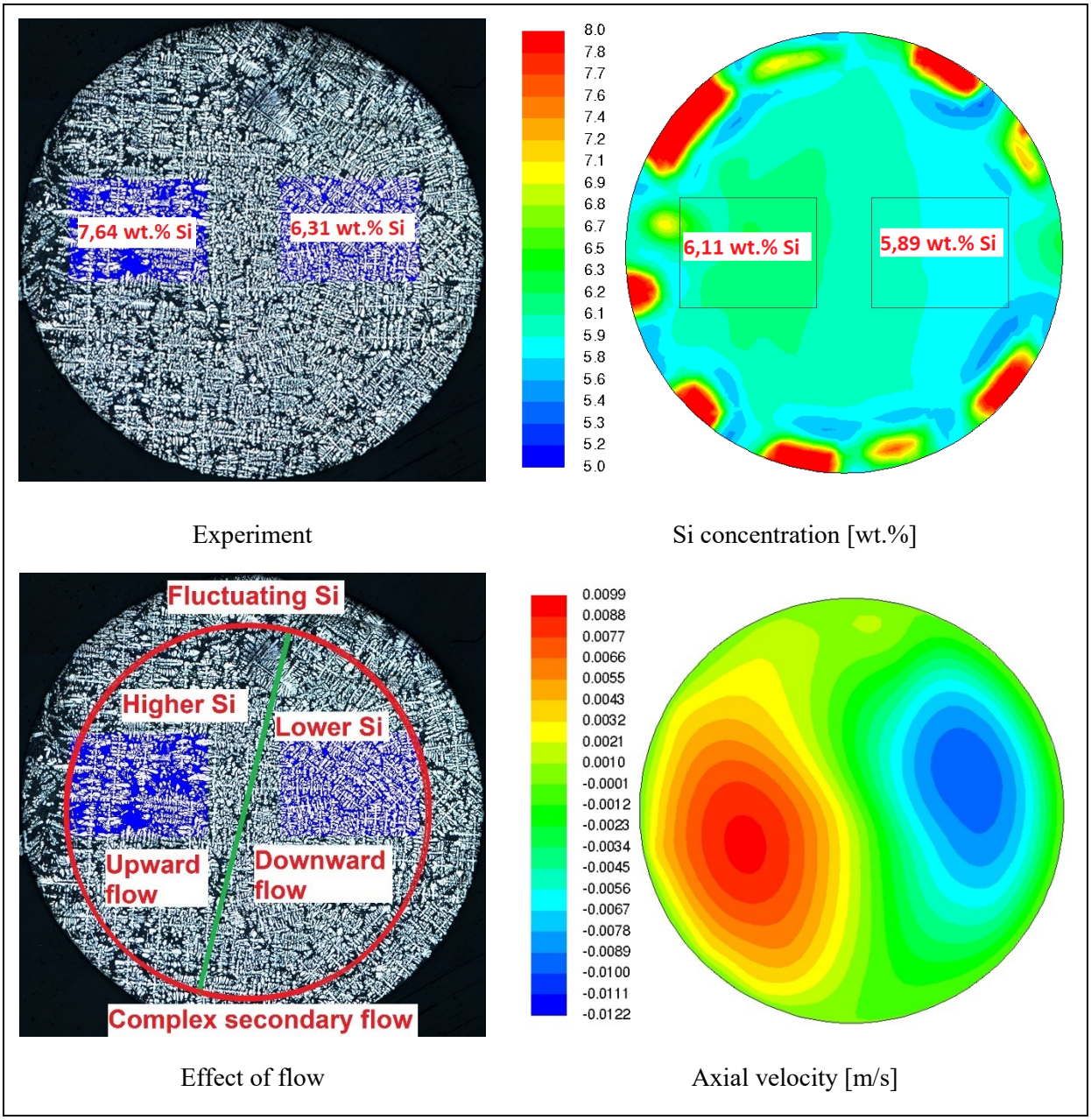

Figure 4.41 Effect of the flow field on the Si concentration distribution and comparison with the measurement

The flow is driving the solute away from the solidification front to higher regions and is squeezing the solute away also from the other side of the melt – Figure 4.42. If the solidification is fast enough (like in the current case), the segregation can be frozen.

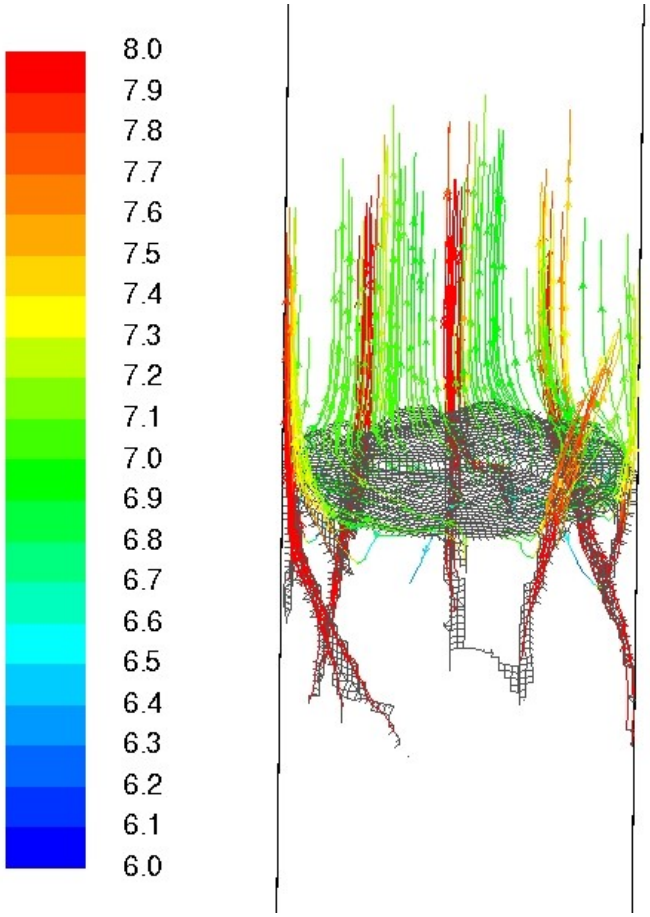

Figure 4.42 .Pathlines of the flow colored by Si concentration [wt.%]

The region of upward-, downward- and secondary flow is not completely clear yet (the primary flow is the one induced by the magnetic field directly and the secondary is the natural flows appearing in all other directions). Further work is needed on the system to investigate the details.

4.5.6. Solidification simulation – upward Lorenz force field

4.5.6.1 Setup

The setup of this model was identical to the bidirectional case except the Lorenz force field, which is directed upwards (40 mT, 50 Hz) in the whole media. Experimental results were not available so far, but the result will be presented in this chapter.

4.5.6.2 Flow field

The flow field can be inspected on Figure 4.43. The maximal value is only 0.003 m/s, which is one order of magnitude lower than the 20 mT bidirectional case. Here, in the upward case, the complete liquid media is pushed upwards against the gravity. The melt is primarily flowing upwards, but it must come back down, and the downward flow is slowed down by the upward Lorenz force. Bigger eddies can appear in such a system even in a slowly flowing media. The flow field becomes much more complex.

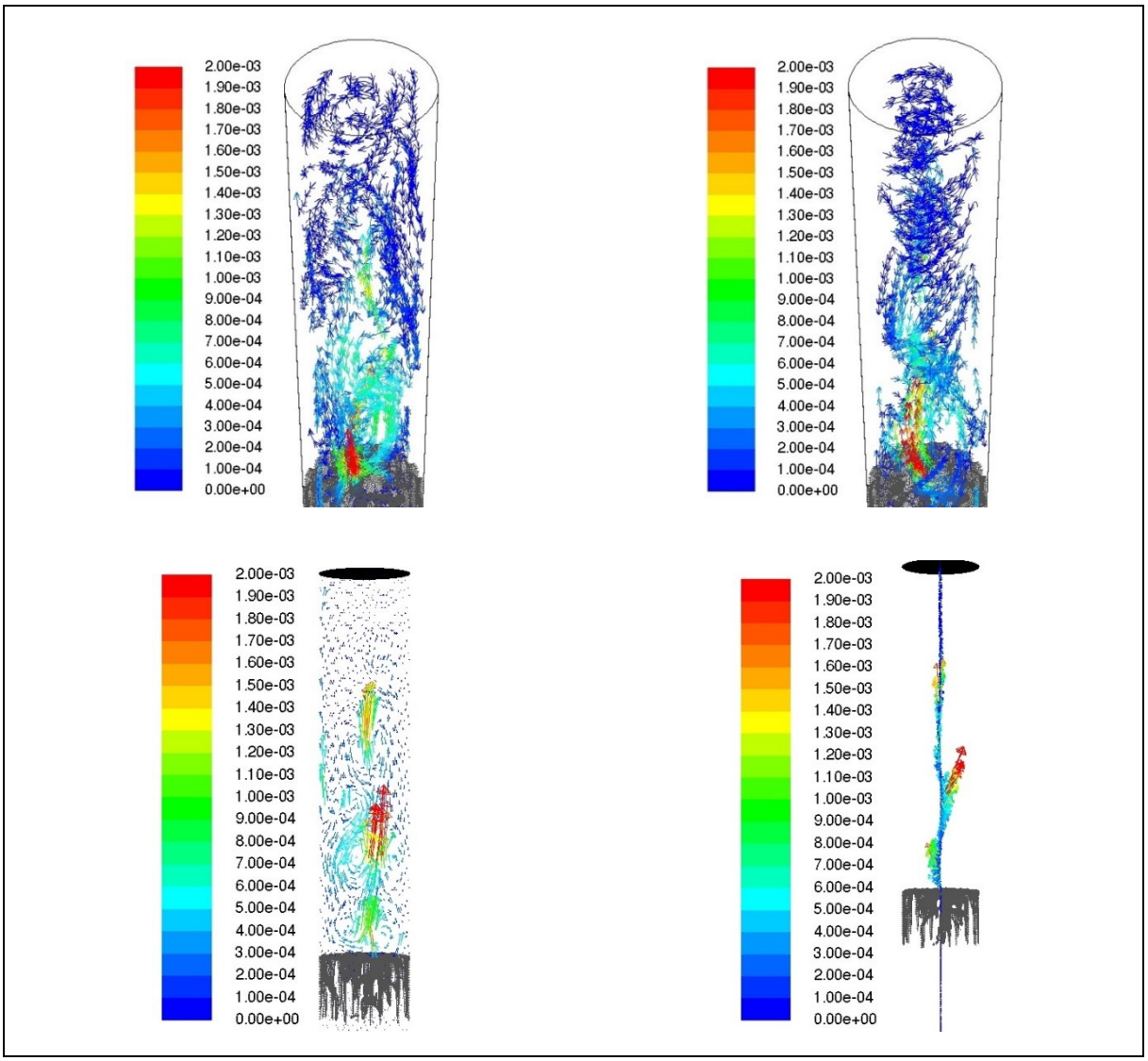

Figure 4.43 Pathlines (up) and vectors (down) of the flow field colored by velocity magnitude [m/s]

4.5.6.3 Solute distribution

The resulting solute distribution is presented on Figure 4.44. Since no measurement result is available, no comparison can be done. However, one can observe that surprisingly similar segregation profile appears as in the case of RMF mixing: fish scale / Christmas tree.

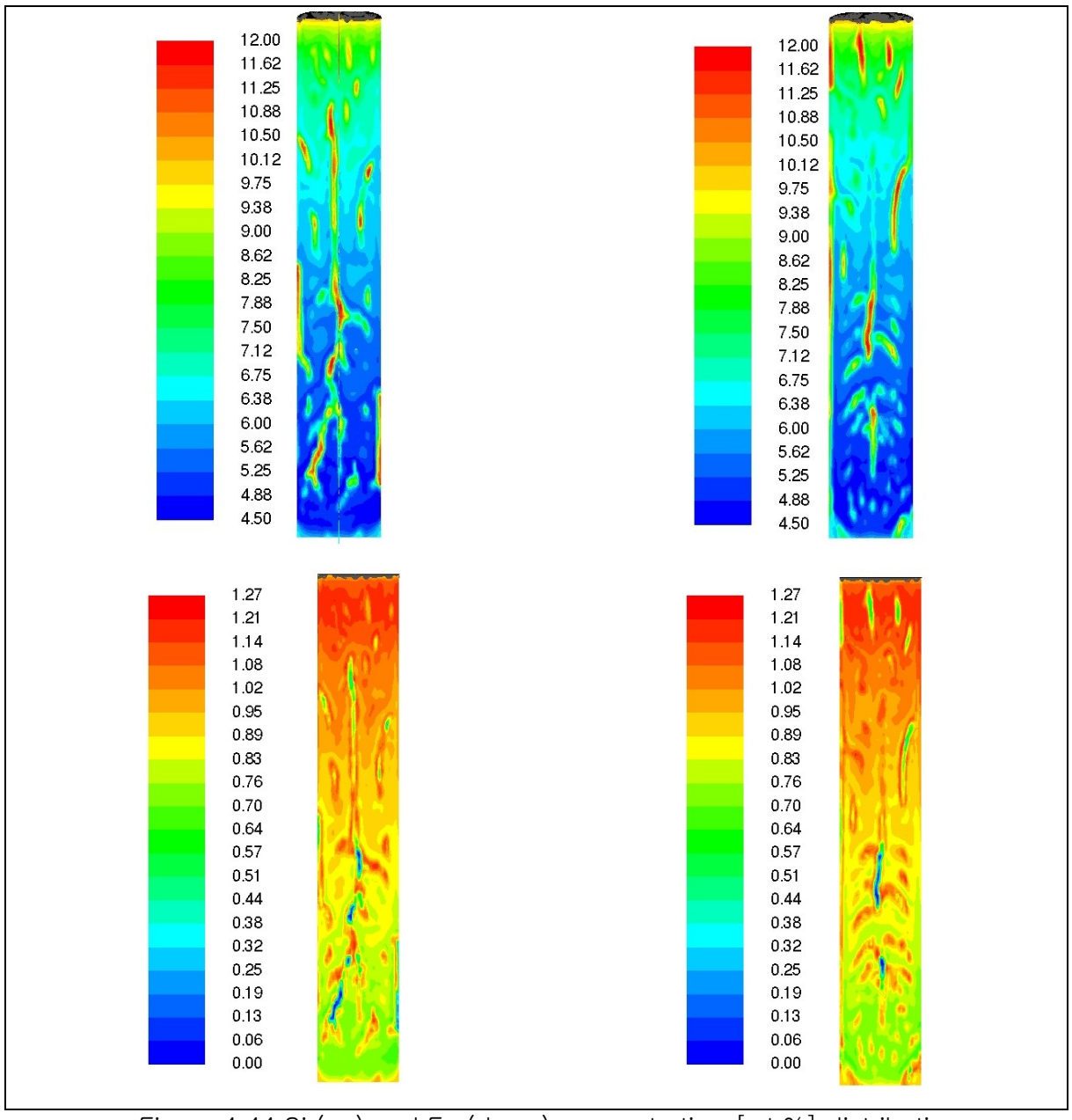

Figure 4.44 Si (up) and Fe (down) concentration [wt.%] distribution in perpendicular sections

4.5.7. Conclusion of TMF models

Based on the current results, the TMF simulation can be performed with rather good accuracy if we consider the results presented in chapter 4.5.3 too. The solute distribution of the bidirectional case is promising. Further work including more measurements should be done.

5. Chapter:
Conclusions and scientific results

5.1. Conclusions

The current industrial needs for high quality aluminum require detailed knowledge of the phenomena arising during the processing of the materials. Without gathering information about the solidification conditions of a complex casting part, or a pre-product, like a billet for rolling, unexpected and unwanted failures can appear. To have a clearer picture on solidification processes, the work on the simulation of aluminum solidification under forced magnetic induction was presented in the thesis work.

The experimental work of other scientific groups was mentioned including the possibilities for numerical investigations. The numerical models were presented in more details, since those were used as basis of this project including magnetohydrodynamic background.

The results on RMF and TMF experiments performed on the special facilities of Miskolc were discussed. Those results were the validation keys of the project.

In case of RMF field, enormous amount of experimental data is available including the thermal dataset of each experiment. The macrostructural images, concentration maps and temperature datasets were used as validation points or boundary conditions. The temperature field monitoring during the experiments provided a great advantage to simulate a thermal system accurately with the smallest effort possible so far. The qualitative accuracy of the models is surprisingly great. Moreover, in case of Lever rule approach, the quantitative conformity is really promising.

More complex simulation system had to be built up for the TMF facility due to its innovative design. Since the Lorenz force field cannot be directly described with any parametric equation, electromagnetic simulations were performed using Comsol Multiphysics. The results of the simulations were directly validated using the measurement results of the magnetic induction vector components close to the inductor heads, but it is not directly connected to the induced Lorenz force field.

To be able to validate the magnetohydrodynamic effects, the thermal gradient shift phenomen was used. The global thermal system of the complete facility was simulated for the heat fluxes on the crucible wall, which was interpolated in a thermal-flow model. The latter simulation was performed to quasi-validate the results of the MHD system. After several adjustments and introduction of the reduction factor for the Lorenz force field, the gradient shift effect could be simulated with great accuracy.

Solidification simulations were also performed for the TMF field using a ternary approach. Two models were presented: using bidirectional and upward Lorenz force field. Qualitative comparison was possible only for the bidirectional case, since the preparation of the samples were not possible in time for the upward case. The solute distribution conforms well with the resulting macrostructure.

5.2. Scientific results of the project

My results in the project, which are new for the state of the art are the following:

Thesis 1:

Coupled multiphysics CFD RANS k-ε and magnetic force 3D simulation of solidification under rotating magnetic field in a cylindrical medium has no advantage and additional information compared to 2D-axisymmetrical cases. The flow field is quas-iaxisymmetric, and the solute distribution has no major difference, but the computational time longer or requirements are much higher in 3D case. The computation time of 3D is approximately 5-10x on a same hardware. For such simulations, 2D axisymmetric computations are recommended.

Thesis 2:

Coupled multiphysics CFD and magnetic force simulation of solidification under rotating magnetic field in a cylindrical medium, the Envelope method of solidification compared to Lever rule has weaknesses for higher volume of solidifying metal. The solute distribution shows qualitative correspondence with the measurements, but quantitatively there are either large differences. On the other hand this problem did not occur with Lever rule. The Lever rule is an explicit analytical computation which fulfill the necessary conservation rules itself. In contrary, the Envelope model is an iterative computation, which incorporate an accuracy to, or on other hand a deviation from the conservation phenomena. The comparison of measured and calculated concentration fields suggests the application of Lever rule.

Thesis 3:

The directly unmeasurable flow patterns appearing inside the TMF Solidification facility designed and constructed by MTA-ME Materials Science Research Group at Miskolc, Hungary can be simulated and validated with the same multiphysics simulation as presented at RMF case. A thermal gradient shift effect was measured by 13 thermocouples of the facility. The geometry and the model were exceeded with the whole facility, and the measured temperature distribution was calculated too. Based on the comparison of the measured and calculated temperatures the validation of the flow is possible due to the strong connection between the different phenomena. The validation can be continued via the solute distribution resulting in the solidification modeling. Qualitatively the computed concentration field fits to the microstructure of the experimentally crystallized sample. This proves that this method of validation of such a complex multiphysics simulation gives the scientifically desired result. The same computation facility gives the same quality of computation either a TMF or RMF simulations.

6. References

[1] Lorenz Ratke, Sonja Steinbach, Georg Müller, Marc Hainke, András Roósz, Yves Fautrelle, M.D. Dupouy, Gerhard Zimmermann, A. Weiß, Hermann-Josef Diepers, Jacques Lacaze, R. Valdes, G.U. Grün, H.-P. Nicolai, H. Gerke-Cantow: MICAST – Microstructure Formation in Casting of Technical Alloys under Diffusive and Magnetically Controlled Convective Conditions. Mat. Sci. Forum, 2006, 508: 131.

[2] J.N. DuPONT, Mathematical Modeling of Solidification Paths in Ternary Alloys: Limiting Cases of Solute Redistribution, Metallurgical Materials Transaction, 37A (2006), 1937 – 1947

[3] X.Dore, H.Combeau, M.Rappaz, Microsegregation in ternary alloys: application to the solidification of Al-Mg-Si, Acta mater. 48 (2000) 3951–3962

[4] M. Rappaz and Ph. Thevoz, Solid diffusion model for equiaxed grozth, Acta metall. Vol. 35, No. 7, pp. 1487-1497, 1987

[5] M.Rappaz and W.J.Boettinger, On dendritic solidification of the multicomponent alloys with unequal liquid diffusion coefficients, Acta mater. Vol. 47 (1999), No. 11, pp. 3205-3219,

[6] C.Y.Wang and C.Beckermann, A unified solute diffusion model for columnar and equiaxed dendritic alloy solidification, Materials Science and Engineering, A171 (1993), 199-211

[7] C.Y.Wang and C.Beckermann, A multiphase solute diffusion model for dendritic alloy solidification macroscopic models, Metall. Trans A, 1993, 24A, 2787-2802

[8] A.I. Ciobanas and Y. Fautrelle, Ensemble averaged multiphase Eulerian model for columnar / equiaxed solidification of a binary alloy: I. The mathematical model, J. Phys. D: Appl. Phys. 40 (2007) 3733–3762

[9] D. A. Drew and S.L. Passman. Theory of Multicomponent Fluids. Springer, 1999

[10] M. Wu, Y. Zheng, A. Kharicha, A. Ludwig, Numerical analysis of macrosegregation in vertically solidified Pb-Sn test castings – Part I: Columnar solidification, Computational Materials Science, 124 (2016) 444-455

[11] Ch.-A. GANDIN, J.-L. DESBIOLLES, M. RAPPAZ, and Ph. THEVOZ: A Three-Dimensional Cellular Automaton–Finite Element Model for the Prediction of Solidification Grain Structures Met Mat trans VOLUME 30A, DECEMBER 1999—3153

[12] Youssef Souhar, Valerio F. De Felice, Christoph Beckermann, Hervé Combeau, Miha Zaloznik, Three-dimensional mesoscopic modeling of equiaxed dendritic solidification of a binary alloy, Computational Materials Science 112 (2016) 304–317

[13] W.D. Bennon, F.P. Incropera, A continuum model for momentum, heat and species transport in binary solid-liquid phase change systems-I. Model formulation, International Journal of Heat Mass Transfer 30 (1987) 2161-2170.

[14] W.D. Bennon, F.P. Incropera, A continuum model for momentum, heat and species transport in binary solid-liquid phase change systems- II. Application to solidification in a rectangular cavity, International Journal of Heat Mass Transfer 30 (1987) 2171-2187

[15] S.D. FELICELLI, J.C. HEINRICH, D.R. POIRIER , Metallurgical and Materials Transactions B, 22B, 1991, 847 – 859

[16] N. Ahmad, H. Combeau, J.L. Desbiolles, T. Jalanti, G. Lesoult, J. Rappaz, J, M. Rappaz, C. Stomp, Numerical simulation of macrosegregation: a comparison between finite volume method and finite element method predictions and a confrontation with experiments, Metallurgical and Materials Transactions A, (1998) 29A, 617-630, doi 10.1016/S1359-6454(00)00177-4

[17] https://benchmark-solidification.ijl.univ-lorraine.fr/

[18] M. Bellet, H. Combeau, Y. Fautrelle, D. Gobin, M. Rady, E. Arquis, O. Budenkova, B. Dussoubs, Y. Duterrail, A. Kumar, C.A. Gandin, B. Goyeau, S. Mosbah, M. Zaloznik, Call for contributions to a numerical benchmark problem for 2D columnar solidification of binary alloys, International Journal of Thermal Sciences 48 (2009) 2013–2016

[19] H. Combeau, M. Bellet, Y. Fautrelle, D. Gobin, E. Arquis, O. Budenkova, B. Dussoubs, Y. Du Terrail, A. Kumar, Ch.-A. Gandin, B. Goyeau, S. Mosbah, T. Quatravaux, M. Rady, M. Zaloznik, Analysis of a numerical benchmark for columnar solidification of binary alloys, IOP Conference Series-Materials Science and Engineering (2012), V33, UNSP 012086, doi 10.1088/1757-899X/33/1/012086

[20] Ni, J., and Beckermann, C., "A Volume-Averaged Two-Phase Model for Solidification Transport Phenomena," Metall. Trans. B, Vol. 22B, 1991, pp. 349-361.

[21] R. Boussaa, L. Hachani, O. Budenkova, V. Botton, D. Henry, K. Zaidat, H. Ben Hadid, Y. Fautrelle, Macrosegregations in Sn-3wt%Pb alloy solidification: Experimental and 3D numerical simulation investigations, International Journal of Heat and Mass Transfer (2016), V100, 680-690

[22] M.J.M. Krane, F.P. Incropera, D.R.Gaskell, Solidification of ternary metal alloys - 1. Model development, International Journal of Heat and Mass Transfer (1997), V40, 3827-3835

[23] M.J.M. Krane, F.P. Incropera, Solidification of ternary metal alloys .2. Predictions of convective phenomena and solidification behavior in Pb-Sb-Sn alloys, International Journal of Heat and Mass Transfer (1997), V40, 3837-3847

[24] S.D. FELICELLI, D.R. POIRIER, J.C. HEINRICH, Modeling freckle formation in three dimensions during solidification of multicomponent alloys, Metallurgical and Materials Transactions B, 29B, DECEMBER 1998, 847 – 855

[25] M. Medina, Ségrégation par solidification en présence de convection naturelle ou forcée. Thèse d'état, Institut National Polytechnique de Grenoble 2000

[26] M. Medina, Y. Du Terrail, F. Durand and Y. Fautrelle, Channel segregation during solidification and the effects of an alternating travelling magnetic field. Metallurgical and Materials Transactions B 2004, 35B : 743 - 754

[27] P.A. Nikrityuk, K. Eckert, R. Grundmann, A numerical study of unidirectional solidification of a binary metal alloy under influence of a rotating magnetic field, International Journal of Heat and Mass Transfer 49 (2006) 1501–1515

[28] O.Budenkova, F.Baltaretu, S.Steinbach, L.Ratke, A Roósz, A Rónaföldi, J Kovács, A-M Bianchi and Y. Fautrelle, Modeling of Al-7wt%Si-1wt%Fe ternary alloy: application to space experiments with a rotating magnetic fields, Materials Science Forum, Vol.790-791 (2014) pp 46-51

[29] G.M.Poole, Mathematical modeling of solidification phenomena in electromagnetically stirred melts, PhD Thesis, Department of Metallurgical and Materials Engineering in the Graduate School of The University of Alabama, 2014

[30] K. Zaidat: Influence d'un champ magnétique glissant sur la solidification dirigée des alliages métalliques binaires, 2005, PhD Thesis, Grenoble, France

[31] [Mullins and Sekerka] W.W. Mullins, R.F.Sekerka; Stability of a Planar Interface During Solidification of Dilute Binary Alloy, J. Appl. Phys., 35 (1964), 444-451

[32] Trivedi, Interdendritic Spacing: Part II. A Comparison of Theory and Experiment Met. Trans. A, 15A (1984), p. 977-982

[33] J.D. Hunt, Steady-State Columnar and Equiaxed Growth of Dendrites and Eutectic, Mater. Sci. Eng., 65 (1984), p. 75-83.

[34] W. Kurtz, D. J. Fisher: Fundamentals of Solidification, Trans Tech Publications 1986

[35] A.I.Ciobanas, A.Bejan and Y.Fautrelle, Dendritic solidification morphology viewed from the perspective of constructal theory, J.Phys. D: Appl. Phys. 39 (2006), 5252-5266

[36] N. Shevchenko, S. Boden, G. Gerbeth, and S. Eckert, "Chimney Formation in Solidifying Ga -25wt pct In Alloys Under the Influence of Thermosolutal Melt Convection," Metall. Mater. Trans. A, v44 (2013), no. 8, pp. 3797-3808

[37] A Kao, N Shevchenko, O Roshchupinka, S Eckert, Koulis Pericleous. Thin Sample Alloy Solidification in Electromagnetic Driven Convection. 8th International Conference on Electromagnetic Processing of Materials, Oct 2015, Cannes, France. EPM2015. <hal-01331836>

[38] C.Y.Wang and C.Beckermann, Equiaxed Dendritic Solidification with Convection: Part I. Multiscale/Multiphase Modeling, Metal.Mat.Trans., 27A 1996, 2754 - 2765

[39] C.Y.Wang and C.Beckermann, Equiaxed Dendritic Solidification with Convection: Part II. Numerical Simulations for an Al-4 Wt Pct Cu Alloy, Metal.Mat.Trans., 27A 1996, 2765 - 2783

[40] C.Y.Wang and C.Beckermann, Equiaxed Dendritic Solidification with Convection,

[41] Part III. Comparisons with NH4CI-H20 Experiments, Metal.Mat.Trans., 27A 1996, 2784 – 2795

[42] YZheng, M. Wu, E. Karimi-Sibaki, A. Kharicha, A. Ludwig, Use of a mixed columnar-equiaxed solidification model to analyse the formation of as-cast structure and macrosegregation in a Sn-10 wt% Pb benchmark experiment

[43] YZheng, M. Wu, E. Karimi-Sibaki, A. Kharicha, A. Ludwig, Use of a mixed columnar-equiaxed solidification model to analyse the formation of as-cast structure and macrosegregation in a Sn-10 wt% Pb benchmark experiment

[44] O. Budenkova, A. Noeppel, J. Kovács, A. Rónaföldi, A. Roósz, A-M. Bianchi, F. Baltaretu, M. Medina, and Y. Fautrelle. Comparison of the simulation and experimental results of the effect of RMF on directional solidification of Al-7wt% Si, Proc. 5th Int. Conf. on Solidification and Gravity, September 2008, in Materials Science Forum 2010, V649, 269-275

[45] J. Kovacs, A. Ronafo ldi, G. Gergely, Z. Gacsi, and A. Roosz, Proc. 5th Decennial Int. Conf. on Solidification Processing, H. Jones, ed., University of Sheffield, Sheffield, United Kingdom, 2007, pp. 405–10.

[46] A. Noeppel, A. Ciobanas, X. D. Wang, K. Zaidat, N. Mangelinck, O. Budenkova, A. Weiss, G. Zimmermann, Y. Fautrelle, Influence of Forced/Natural Convection on Segregation During the Directional Solidification of Al-Based Binary Alloys, Metallurgical and Materials Transactions B (2010), V41, 193–208

[47] J. Kozeny, "Ueber kapillare Leitung des Wassers im Boden." Sitzungsber Akad. Wiss., Wien, 136(2a): 271-306, 1927.

[48] P.C. Carman, "Fluid flow through granular beds." Transactions, Institution of Chemical Engineers, London, 15: 150-166, 1937.

[49] Ivantsov G.P.: Temperature field around a spheroidal, cylindrical and acicular crystal growing in a supercooled melt. Dynamics of curved fronts, pages 243-245. Academinc Press Boston. Translation from Russian by Protrans, 1988

[50] Alexandru Ciobanas, PhD Thesis, Modélisation statistique de la solidification colonnaire/équiaxe des alliages binaires, Grenoble INP 2006

[51] A. Rónaföldi; Forgó mágneses mezős magneto-hidrodinamikai keverővel ellátott kristályosító berendezés kifejlesztése és vizsgálata. PhD thesis. Miskolc. 2008

[52] Z. Yan, X. Li, Z. Cao, X. Zhang, Tingju Li: Grain refinement of horizontal continuous casting of the CuNi10Fe1Mn alloy hollow billets by rotating magnetic field (RMF). Materials Letters, vol. 62, p. 4389-4392. 2008

[53] K. Stransky, F. Kavicka, B. Sekanina, J Stetina, V. Gontarev, J. Dobrovska: The effect of electromagnetic stirring ont he crystallization of concast billets. Materials and technology 45, p. 163-165. 2011

[54] S. Steinbach, L. Ratke: The effect of rotating magnetic field ont he microstructure of directionally solidified Al-Si-Mg alloys. Materials Science And Engineering A 413-414, p. 200-204. 2005

[55] S. Eckert, B. Willers, P.A. Nikirtyuk, K. Eckert, U. Michel, G. Zouhar: Application of a rotating magnetic field during solidification of Pb-Sn alloys: Consequences of CET. Materials Science And Engineering A 413-414, p. 211-216. 2005

[56] J. Kovács, A. Rónaföldi, A. Roósz: Unidirectional Solidification of Binary and Ternary Aluminium Alloys in a Rotating Magnetic Field. 6th International Conference on Electromagnetic Processing of Materials (EPM), Forschungszentrum Dresden-Rossendorf, ISBN978-3-936104-65-3, p. 664-667. Dresden, Germany. 2009. october 19-23.

[57] L. Hachani: Etude de l'influence de la convection naturelle et forcée sur le processus de la solidification : cas d'un alliage métallique binaire. PhD thesis, Grenoble, 2013

[58] Roósz, A. Rónaföldi, J. Kovács and M. Svéda: Effect of Low Rotating Magnetic Field (RMF) linduced Melt Flow on the Microstructure of Unidirectionally Solidified Al-7wt.%Si-1wt.%Fe Alloy, Proceedings of the 6th Decennial International Conference on Solidification Processing (SP17), Old Windsor, England, 2017. Július 25-28., edited by Z. Fan, pp. 308-311.C

[59] Kader Zaidat. Influence d'un champ magnétique glissant sur la solidification dirigée des alliages métalliques binaires. Electromagnétisme. INSTITUT NATIONAL POLYTECHNIQUE DE GRENOBLE, 2005. Français. <tel-01339002>

[60] G. Kaptay: Approximated equations for molar volumes of pure solid fcc metals and their liquids from zero Kelvin to above their melting points at standard pressure. J. Mater. Sci., 2015, vol.50, pp.678-687. See J174 attached.

[61] Y. Plevachuk, I. Egry, J. Brillo, D. Holland-Moritz, I. Kaban: Density and atomic volume in liquid Al-Fe and Al-Ni binary alloys. Int. J Mater Res, 2007, vol.98, pp.107-111.

[62] D. R. Poirier: Density, viscosity and diffusion coefficients in hypoeutectic Al-Si liquid alloys: an assessment of available data. Metall Mater Trans A, 2014, vol.45B, pp.1345-1354.

7. Annex

The articles published on the simulation of RMF stirred liquid metal flows can be found in this chapter.

Comparison of measured and numerically simulated angular velocity of magnetically stirred liquid Ga-In alloy

Cs. Nagy[1, a], A. Rónaföldi[2, b], A. Roósz[3, c]

[1, 2, 3]MTA-ME Materials Science Research Group, Miskolc-Egyetemváros, Hungary

[a]ntsart@gmail.com, [b]elkronar@uni-miskolc.hu, [c]femroosz@uni-miskolc.hu

Keywords: gallium, indium, magnetic, MHD, stirring, simulation, angular velocity, revolution number, melt flow

Abstract. A measurement of the angular velocity/revolution number of magnetically stirred liquid gallium-indium alloy was realized with newly developed angular velocity measuring equipment. To get additional information about the flow of the melt, a numerical simulation model was performed with ANSYS FLUENT 13.0 with a single phase 2D k-ε turbulence solver. The aim was to reproduce the flow as accurate as possible, so the measured and computed angular velocity data was compared, to see if the system can be modeled fairly well.

Introduction

During the solidification of metals and alloys – under Earth circumstances – there are flows inside [1-3]. The trait and intensity of these flows are strongly affecting the structure of the solidified metals and alloys and by this, the properties too. This affect can be quite significant, so the investigation of the phenomena is really important.

The inspection is in a way that externally induced flows – with different intensity and direction – are made in the metal- or alloy-melt (collectively designated as molten metal) for solidification. These streams induced from outside, have to be more intense than those inside, namely the effect of the outer stimulation should be dominant. We can draw conclusions on the flows without outer stimulation as well according to examinations achieved this way.

This paper runs on flows induced by MHD rotating magnetic field (RMF). The used experimental MHD stirrer can produce significantly higher inductions (~90 mT) than other equipment in the literature.

To get a clear view of the properties of the flow, the revolution number/angular velocity of 75,5%Ga-24,5%In alloy-melt was measured with newly developed “pressure compensating” equipment [4]. The data is useful, but additional flow parameters are needed, so a numerical model was prepared with ANSYS FLUENT 13.0. Simulations of magnetically stirred melts were also developed by Budenkova et al. [5,6]. Our model was produced as simple as possible – two dimensional axis symmetrical k-ε turbulent model with the inducing force filed. The measured and computed angular velocity data was compared to see the accuracy and possibilities of the model.

The MHD system

The operation of the facility is based on the Maxwell equations. If the conducting fluid is put into the rotating magnetic field, an eddy current is induced in it. By the law of Lenz, the melt is trying to obstruct the inducing field, so it stars rotating. The force – which makes the stirring – is the Lorenz force – see Fig 1. and Eq. 1.

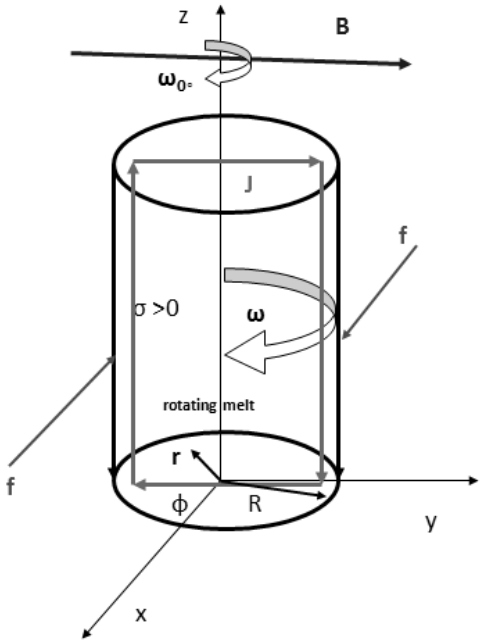

Figure 1. The MHD system

$$F_{Lorenz} = 0{,}5\ \sigma\ B_0^2\ r\ [\omega_0-\omega] \qquad (1)$$

Where:

- σ is the electrical conductivity of the melt – $3{,}58*10^6$ S/m,
- B_0 is the magnetic induction – strength of the magnetic field – T,
- r is the distance from the axis - m,
- ω_0 is the synchronous angular velocity of the MHD stirrer – rad/s,
- ω is the angular velocity of the fluid (molten metal/alloy) – rad/s.

The measuring method [4]

The metallostatic pressure belonging to the "h" height is in equilibrium with the "Δp" pressure difference developing between the pressure along the "R" radius and the pressure being on the axis. The pressure difference depends on the height of liquid column (h), the density of melt (ρ_{melt}) as well as on the gravitation constant (g):

$$\Delta p = h\ \rho_{melt}\ g \qquad (2)$$

The height of the magnetically stirred liquid alloy, with stable tank:

$$h = \omega^2 R^2 / 2g \quad (3)$$

From Eq. 2 and Eq. 3:

$$\Delta p = \rho_{melt}\, g\, [\, \omega^2 R^2 / 2g \,] \quad (4)$$

The angular velocity can be determined on the basis of Eq. 4:

$$\omega = [1/ R]\, [\, 2\, \Delta p / \rho_{melt} \,]\, 0.5 \quad (5)$$

The average revolution number is:

$$n = [60/2\, \pi]\, \omega \quad (6)$$

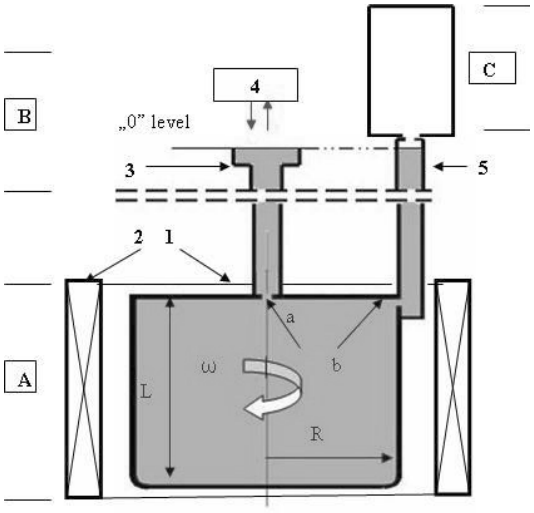

Figure 2. The measuring equipment

It is difficult to measure the pressure developing in the melt without disturbing the melt flow; therefore instead of measuring directly the developed metallostatic pressure, by which it could be compensated, was measured. The sketch of equipment – using a pressure compensation method for the average revolution number measurement – assembled with the MHD stirrer is shown in Fig. 2. The equipment consists of the following three main units:

A. MHD unit, where the stable ceramic (non-conducting) measuring cell /1/ is placed in the MHD inductor /2/
B. Measuring unit, where the measuring tank /3/, the distance meter /4/ and the compensation chamber /5/ can be found
C. "Overpressure" unit, where the compensation pressure develops and it is measured

The measuring cell is a closed tank that is connected to the distance meter and to the compensation chamber through a small hole indicated by "a" and "b" in Fig. 2. The result of the measurement is a volume average of the revolution number/angular velocity. The measured data can be seen in Table 2. and Table 3.

The setup of the numerical model

The aim of the work was to build a model as simple as possible and reproduce the main flow of the melt. By this, a two dimensional axis symmetrical single phase model was created. This choice makes the work faster and lowers the computational requirements. The geometry is a simple 60 mm high and 5 mm wide rectangle. This produces the 10mm inner diameter and 60mm high crucible from the measurements [4]. This crucible was filled fully with the molten alloy. The mesh was a simple hexa mesh with size = 0,1 μm. The turbulence solver was Realizable k-ε model with Enhanced Wall Treatment.

The Lorenz force filed had to be modeled via a **U**ser **D**efined **F**unction (UDF). The coordinate and velocity dependent force was programmed with a C source code. Every cell had a different amount of tangential momentum source at every time step – like it happens in reality.

Two different model series were set to have clear view of the possibilities of simulating the flow with FLUENT. The first was with 50 Hz of inductor frequency; the second was with 150 Hz. The higher frequency makes stronger force, and by this, faster flows. 5 – 5 different inductions were used in each simulation series – see Table 1.

Table 1. The used inductions in the two simulation series – 50 Hz and 150 Hz inductor frequency

50 Hz	150 Hz
Induction [mT]	
22,6	16,8
37,4	26,2
51,5	37,2
68,5	48,2
89,1	65,0

The simulated flow field

It is good to see the properties of the flow pattern first. Fig. 3a-d show the contours of tangential velocity, Fig. 4a-d show the contours of axial velocity and Fig. 5a-d show the contours of radial velocity of models with two inductions and with two frequencies.

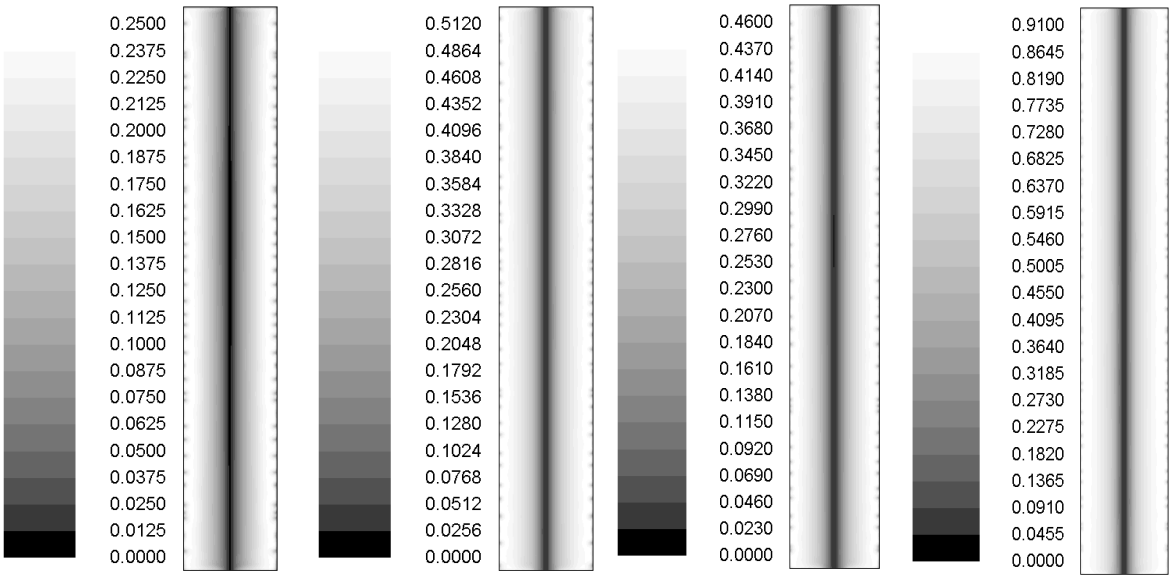

Figure 3. Contours of the tangential velocity [m/s] inside the melt with a) 37 mT induction and 50 Hz inductor frequency, b) 37 mT induction and 150 Hz inductor frequency, c) 69 mT induction and 50 Hz inductor frequency and d) 65 mT induction and 150 Hz inductor frequency

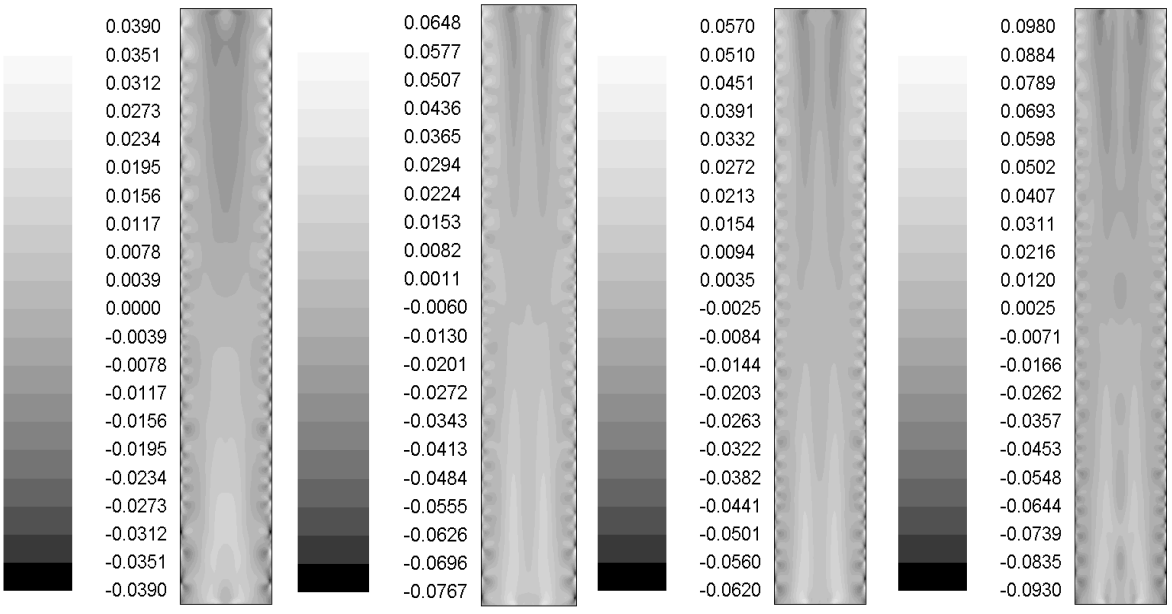

Figure 4. Contours of the axial velocity [m/s] inside the melt with a) 37 mT induction and 50 Hz inductor frequency, b) 37 mT induction and 150 Hz inductor frequency, c) 69 mT induction and 50 Hz inductor frequency and d) 65 mT induction and 150 Hz inductor frequency

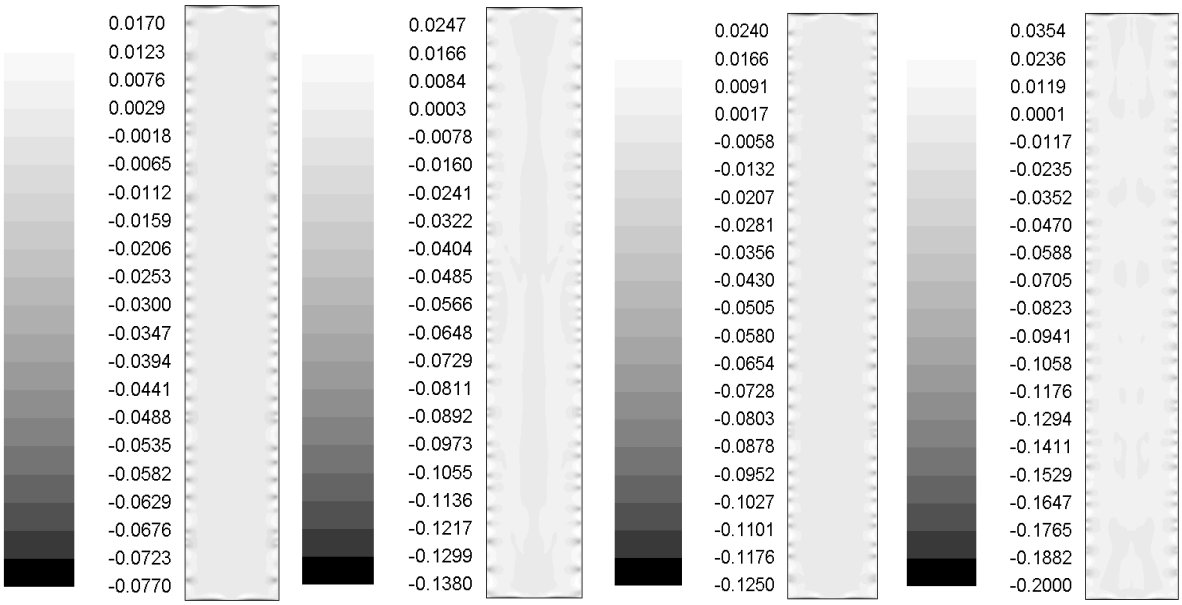

a) b) c) d)

Figure 5. Contours of the radial velocity [m/s] inside the melt with a) 37 mT induction and 50 Hz inductor frequency, b) 37 mT induction and 150 Hz inductor frequency, c) 69 mT induction and 50 Hz inductor frequency and d) 65 mT induction and 150 Hz inductor frequency

As visible, there is no major difference with different setups; just the velocity values are different. With same induction, but higher frequency, the velocities are also higher. It comes from the stronger magnetic field – see Eq. 1. The higher frequency provides higher ω_0, and stronger Lorenz force. To prove the similarity, it is better to see Fig. 5a-d. The path lines run identical.

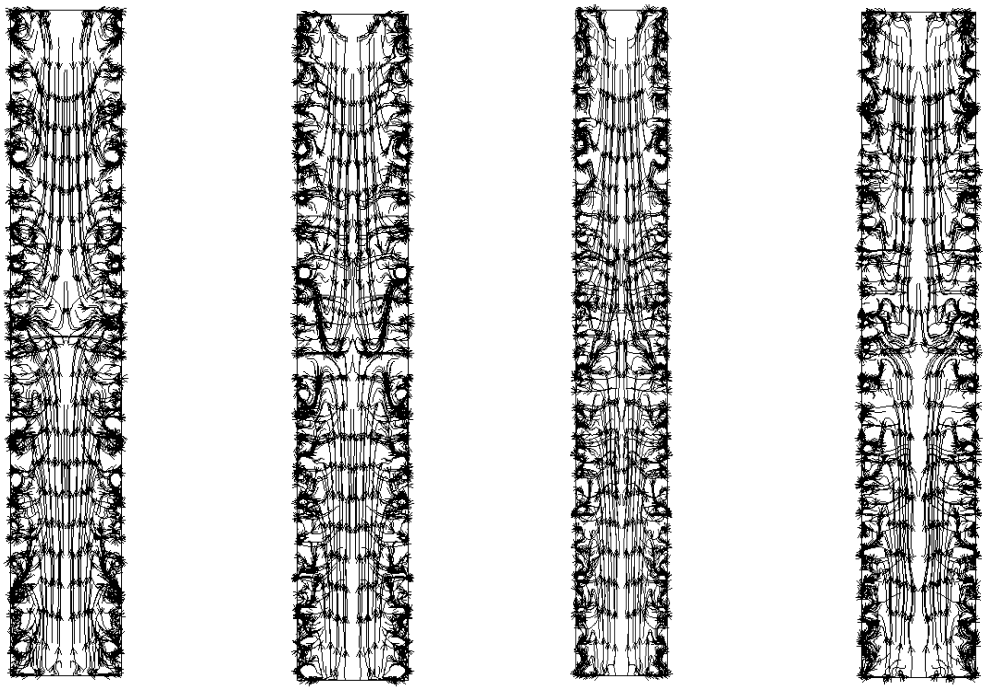

a) b) c) d)

Figure 6. Path lines of the flow inside the melt with a) 37 mT induction and 50 Hz inductor frequency, b) 37 mT induction and 150 Hz inductor frequency, c) 69 mT induction and 50 Hz inductor frequency and d) 65 mT induction and 150 Hz inductor frequency

The angular velocities – time dependence and radial distribution

Theoretically the melt can't reach the synchronous angular velocity of the inductor. It is because of the wall friction, the viscosity and the breaking effect of the melt – see (ω_0-ω) part of Eq. 1. First the melt accelerates constantly and then it starts to reach the possibly maximum with the current conditions – synchronous angular velocity of the inductor, melt material properties, magnetic induction, crucible radius, etc.

The curves of the simulated models can be seen in Fig. 7a for 50 Hz and in Fig. 7b for 150 Hz. The shapes of the curves are similar. The settle of the flow is slower with lower induction and lower frequencies, because of the weaker Lorenz force fields.

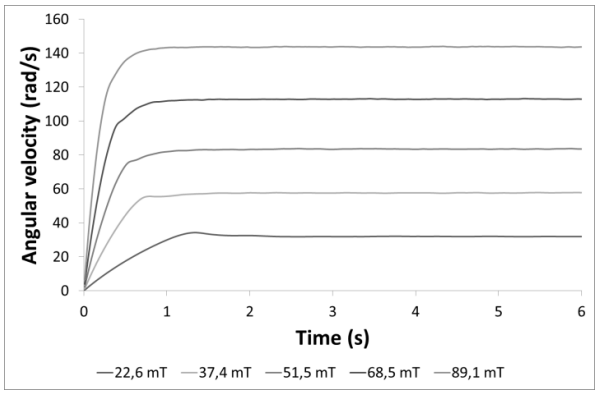

a) 50 Hz

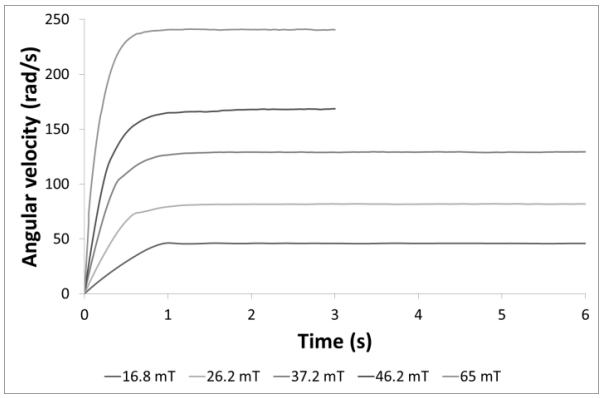

b) 150 Hz

Figure 7. Angular velocity as a function of time

These curves were used to check the model during the iterations. The data was gathered from the velocity field (as a volume weighted average) as in Eq. 7:

$$\omega_{vel.method} = v_t / r \quad (7)$$

The distribution of the angular velocity (computed from tangential velocity – Eq. 7) can be seen in Fig. 9. As the flow is getting faster, the distribution of the angular velocity is getting more anisotropic – the middle of the melt is getting faster. Nearby the axis, the flow is less disturbed with turbulence. In this region there is a pump effect, a laminar uplift or downdraft depending on the vertical coordinate – see Fig. 4 and 6. The wall friction is making small eddies, which slow down the primary flow.

The diagrams in Fig. 8. also can be used to see how the distribution is changing with time, because the flow is faster with bigger induction and slower with lower induction. The flow pattern is changing constantly – or morphing into each other. If we would 'stop' the flow at a time, it would be the same as a settled flow induced by a lower induction.

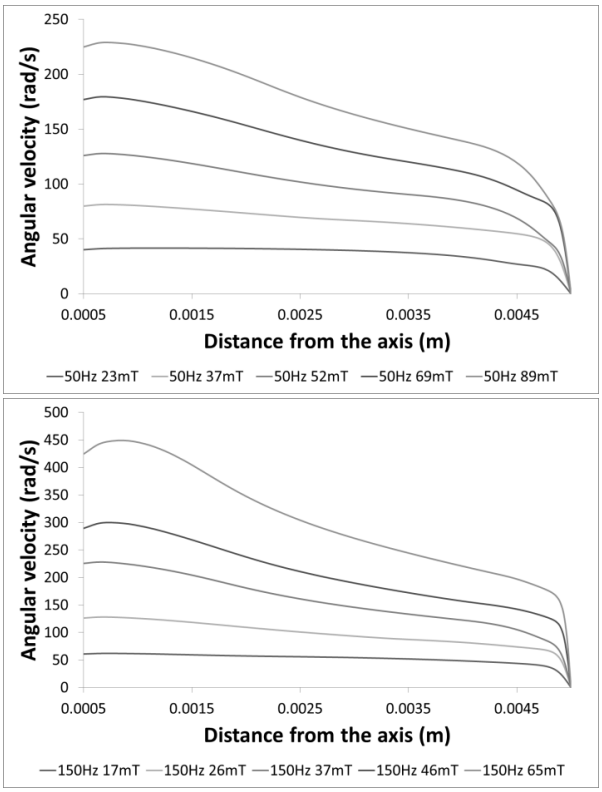

a) 50 Hz b) 150 Hz

Figure 8. Distribution of the angular velocity along the radius

Comparison with the measured data and error analysis.

The angular velocity was computed from the measured pressure difference, so we did the same in the case of the calculations. The pressure pattern inside the melt for two inductions with two frequencies can be seen in Fig. 9a-d.

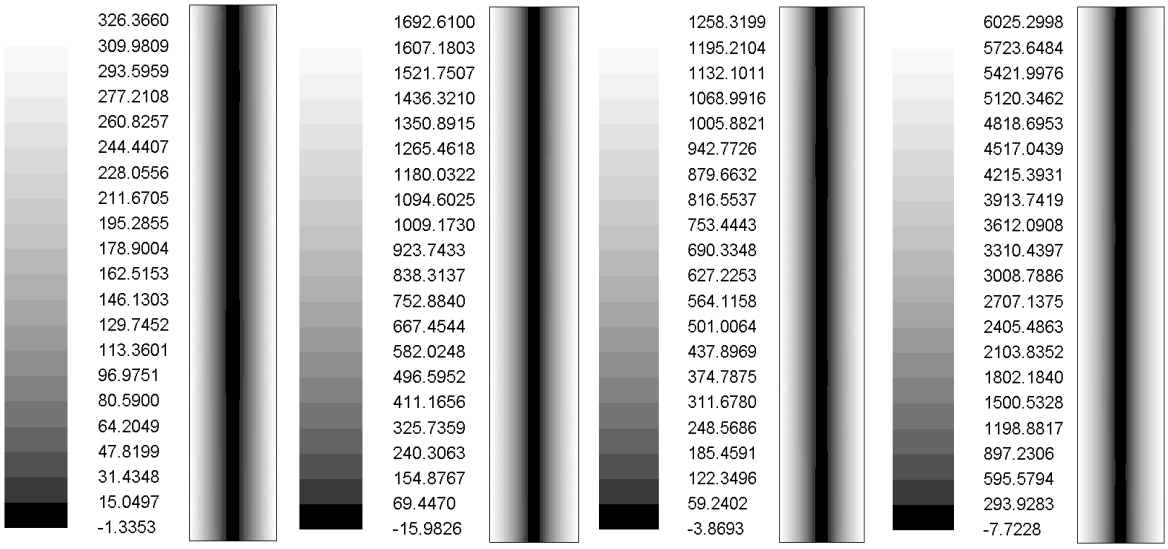

a) b) c) d)

Figure 9. Contours of the static pressure [Pa] inside the melt with a) 37 mT induction and 50 Hz inductor frequency, b) 37 mT induction and 150 Hz inductor frequency, c) 69 mT induction and 50 Hz inductor frequency and d) 65 mT induction and 150 Hz inductor frequency

Using the metallostatic pressure difference, the angular velocity of the melt can be computed with the following equation:

$$\omega_{\text{press. method}} = \sqrt{\frac{2\Delta p}{\rho\, r^2}} \tag{8}$$

Where

- Δp is the metallostatic pressure difference
- ρ is the density of the melt – 6350 kg/m^3
- r is the radius of the crucible – 0,005 m.

The computed and measured pressure differences and the compared angular velocities can be seen in Table 2. for 50 Hz and on Table 3. for 150 Hz.

Table 2. The measured and computed pressure differences, the calculated angular velocities from the data and the relative error of the simulated angular velocities – 50 Hz

50 Hz					
B_0 (mT)	Δp_{sim} (mbar)	Δp_{meas} (mbar)	ω_{sim} (rad/s)	ω_{meas} (rad/s)	Relative Error of ω_{sim} (%)
22.60	1.03	1.20	35.98	38.83	7.34
37.40	3.28	3.60	64.25	67.30	4.53
51.50	6.87	7.30	93.06	95.98	3.04
68.50	12.62	11.50	126.10	120.37	-4.76
89.10	20.37	19.80	160.19	156.69	-2.23
				Absolute average	4.38

Table 3. The measured and computed pressure differences, the calculated angular velocities from the data and the relative error of the simulated angular velocities – 150 Hz

150 Hz					
B_0 (mT)	Δp_{sim} (mbar)	Δp_{meas} (mbar)	ω_{sim} (rad/s)	ω_{meas} (rad/s)	Relative Error of ω_{sim} (%)
16.80	2.07	2.80	51.08	59.24	13.77
26.20	6.66	8.80	91.59	104.98	12.75
37.20	17.09	17.20	146.72	146.96	0.17
46.20	29.46	31.80	192.65	199.82	3.59
65.00	60.36	56.00	275.76	266.80	-3.36
				Absolute average	6.73

Fig. 10. shows the relative error of the models graphically.

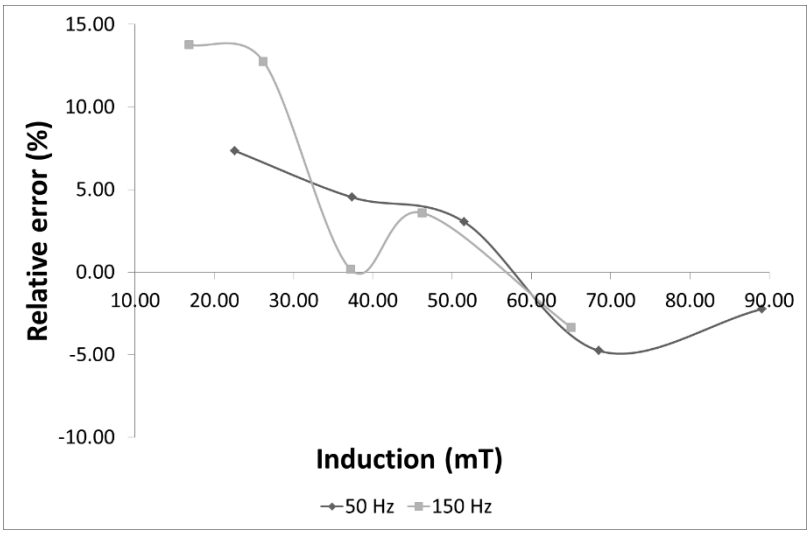

Figure 10. Relative error of the simulated angular velocities compared to the measured data

The error is visibly higher with lower inductions. It can be from the measuring difficulties of the lower pressures. There are other causes of the deviance between the measured and simulated data. The alloy – which was used for the measurements – was mixed by the research group. If the composition of the alloy is not exactly 75,5%Ga-24,5%In, the material properties are different. The digression of the electrical conductivity can make serious differences in the Lorenz force and by this, the angular velocity. There is another point with σ. The data was gathered from literature. We can't be sure if the data is 100% correct. On the other hand, the produced model is as simple as possible. The flow is simplified into an axis symmetrical system; however it is not completely axis symmetrical.

Conclusions

The properties of the flow of magnetically stirred liquid Ga-In alloy have been investigated via measurements and numerical simulations. It is clear, that the flow can be modeled with ANSYS FLUENT on a fairly accurate level. However a three dimensional model should be made to have a complete view of the flow pattern.

Acknowledgement

This work has been carried out as part of the TÁMOP-4.2.1.B-10/2/KONV-2010-0001 project within the framework of the New Hungarian Development Plan. The realization of this project is supported by the European Union, co-financed by the European Social Fund.

References

[1] K. Stransky, F. Kavicka, B. Sekanina, J. Stetina, V. Gontarev, J. Dobrovska: The effect of electromagnetic stirring on the crystallization of concast billets. Materials and technology 45, pp. 163–166. (2011)

[2] B. Yue-long, X. Jun, Z. Zhi-feng, S. Li-kai: Annulus electromagnetic stirring for preparing semisolid A357 aluminum alloy slurry. Trans. Nonferrous Met. Soc. China 19, pp. 1104−1109. (2009)

[3] S. Steinbach, L. Ratke: The effect of rotating magnetic fields on the microstructure of directionally solidified Al–Si–Mg alloys, Materials Science and Engineering A 413–414 pp. 200–204. (2005)

[4] A. Rónaföldi, J. Kovács, A. Roósz: Revolution number (RPM) measurement of molten alloy by pressure compensation method. Materials Science Forum 649 pp 275-280. (2010)

[5] O. Budenkova, A. Noppel, J Kovács, A. Rónaföldi, A. Roósz, A-M. Bianchi, F. Baltaretu, M. Medina, Y. Fautrelle: Comparison between simulation and experimental results of the effect of RMF on directional solidification of Al-7wt.%Si alloy. Materials Science Forum 649, pp 269-274. (2010)

[6] O. Budenkova, F. Baltaretu, J. Kovács, A. Roósz, A. Rónaföldi, A-M. Bianchi and Y. Fautrelle: Simulation of a directional solidification of a binary Al-7wt%Si and a ternary alloy Al-7wt%Si-1wt%Fe under the action of a rotating magnetic field. Modeling of Casting, Welding and Advanced Solidification Processes, Rolduc, Netherlands (2012)

Numerical simulation of the RMF stirring of molten Ga-In alloy using RANS k-ε and LES turbulence models

Csaba Nagy[1,a], Yves Fautrelle[2], Olga Budenkova[2], Arnold Rónaföldi[1], András Roósz[1]

[1]MTA-ME Materials Science Research Group, Miskolc, Hungary

[2]SIMAP/EPM Laboratory, Grenoble, France

[a]femtsabi@uni-miskolc.hu

Keywords: flow simulation, rans, les, mhd, magnetohydrodynamics, fluent, stirring, rmf

Abstract. A comparison of the results of RANS k-ε and LES turbulence models was done via the simulation of the electromagnetic stirring of liquid 75,5%Ga-24,5%In alloy (in a 10 mm diameter & 30 mm high crucible) using Ansys Fluent. Each velocity component, the distribution of eddies inside the melt and other flow parameters were compared respectively. The accuracy was checked with measured angular velocity data of A. Rónaföldi. The turbulent energy spectra were also produced to see the validity of the LES models.

Introduction

Electromagnetically driven flow are usually turbulent. Due to its complexity, simplifications are needed to account for turbulence. Several different turbulent models were developed to solve flow problems regarding to the needs of the user like computing-time or validity/accuracy. The flow simulations of stirring by means of rotating magnetic fields (RMF) of liquid Ga-In alloy were already made [1,2] with RANS k-ε models. However a more accurate model was needed to gather as much information about the magneto-hydrodynamic flow as possible, so the Large Eddy simulation was chosen to be compared with the results of the RANS k- ε model using commercial software, the Ansys Fluent™. The magnetically induced Lorenz force was simulated via a User Defined Function (*UDF*). Three different 3D LES models and a 2D axisymmetric (swirl) Realizable k-ε model with *Enhanced Wall Treatment* near wall function were compared. The three LES models were aimed at evaluating the differences coming from the mesh density and the value of the Smagorinsky constant (cut-off frequency). The accuracy of the models was compared with some measurement data performed by A. Rónaföldi [2,3].

Setup of the models

General setup. The simulated geometry was a cylinder in 3D and a 2D axisymmetric domain. The diameter was 10 mm and the height was 30 mm. The first dimension was chosen because of the measurement data which were obtained with 10 mm diameter. The 30 mm height was chosen due to computing time needs. The 3D geometry was meshed with $0{,}5\text{x}10^6$ and $2\text{x}10^6$ hexa cells; the 2D model was meshed with $3\text{x}10^4$. hexa cells. The induced Lorenz force field was programmed as a tangential force in all cases – via a user defined function. The detailed setup of the force field and the material properties can be found in [1,2]. As in experiment, the numerical model used a 22,6 mT induction magnetic field and 50 Hz inductor frequency. The properties of the liquid phase were:

- Density 6350 kg/m^3
- Viscosity 0,00217 Pa·s
- Electrical conductivity $3{,}65\times10^6$ S/m

All models were transient in order to see the velocity fluctuations (if any) and to be able to investigate the differences between the turbulent kinetic energies and its dissipations. The transient velocity data were also needed for the determination of turbulent energy spectra of turbulence. The spectra were also provided in order to be assess more accurately differences in each LES models.

Conception of LES models. Three different LES models were used to assess the effect of the *Smagorinsky constant* and accordingly, the *cutoff frequency* and the effect of mesh density. The three models were:

- *Cs05* half million cells and C_S = 0,5 Smagorinsky constant
- *Cs02* half million cells and C_S = 0,2 Smagorinsky constant
- *2M* 2 million cells and C_S = 0,2 Smagorinsky constant

The C_S constant determines where the border of direct computing and modeling with Subgrid Scale model is. A higher constant provides a coarser model, because of less direct computing. If a mesh contains less number of cells (which are larger), bigger eddies can be obtained, so a more coarse flow will be simulated. Regarding these facts, the 2M model should be the most accurate.

Results

Primary and secondary flow patterns. The RANS model is very different from all of the LES calculations since it predicts a steady flow. No eddies appear all around the media, except near the wall. The *Enhanced Wall Treatment* is clearly visible. The inner part of the melt is just rotating without any disturbance. However the LES models show more eddies in the cross-section, also near the axis (see Fig. 1). The Cs05 model is in fact a transitional model between the RANS models and the more accurate LES models.

From the observations of the contours from the RANS models to the 2M, a more and more complicated flow pattern is being obtained. The maximum velocities are getting higher too. General averaging methods in the RANS model filters out all eddies inside. The effect of the cut-off frequency (C_s constant) and the mesh density seem to be strong as well on the filtering process.

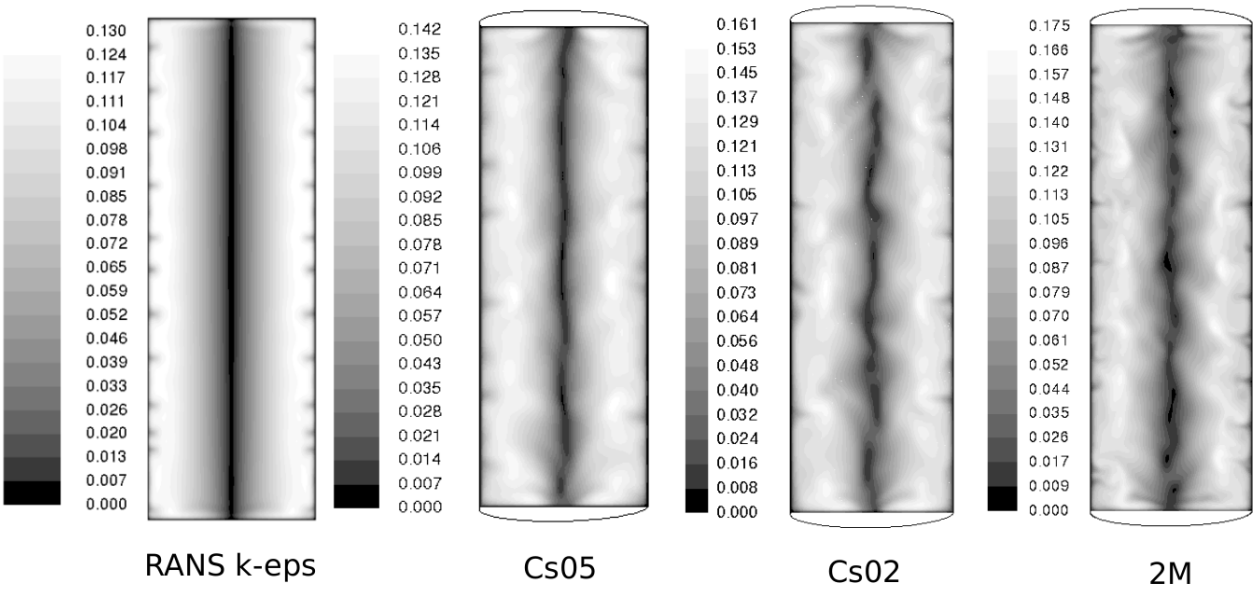

Figure 1. Velocity module of the primary flow in each model

Fig. 2 proofs that there is no eddies except near the boundary inside the domain calculated with the RANS model. In Cs05, the flow nearby the axis hardly disturbed with eddies, but the Cs02 and 2M models put forth eddies everywhere across the melt.

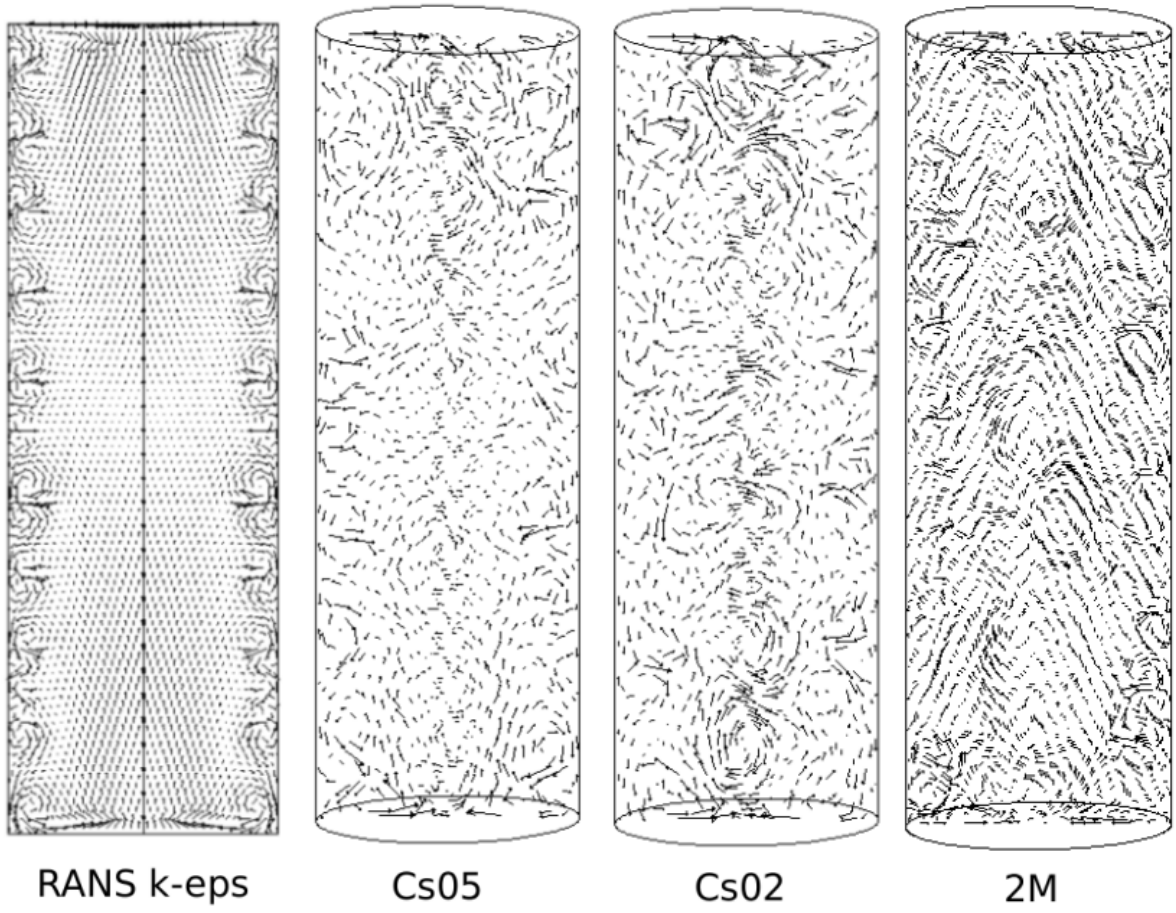

Figure 2. Vectors of the secondary flows for each models

Turbulent kinetic energy. Considering the last results, the RANS model and the most accurate LES model – 2M – will be discussed. The turbulent kinetic energy had to be computed in post-processing for the LES model (because it just provides the velocity data) with the following equation:

$$k = \tfrac{1}{2} (u'^2 + v'^2 + w'^2) \qquad (1)$$

where u', v', w' are the fluctuations of the velocity x, y and z components. The RANS model calculates k and ε directly.

Fig. 3 show the radial distribution of turbulent kinetic energy in RANS (bottom) and 2M (top). In the k-epsilon model, a peak can be seen at 4 mm (near wall region). In the LES model there are 2 peaks – at the axis and at 3 mm, nearby the half of the radius. This proofs that the turbulence exist inside the melt and it is much stronger than turbulence predicted by the RANS model, especially near the wall. It should be stresses however that the symmetry condition at the axis of the domain used in RANS in fact imposes a regularity on the flow and therefore decreases fluctuations.

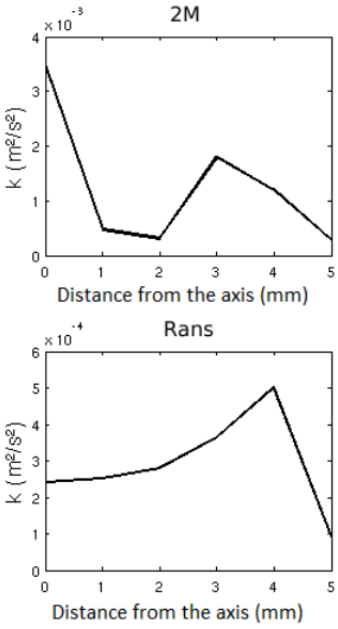

Figure 3.Turbulent kinetic energy alond the radius – RANS & 2M

The average *k* is about 5 times higher in 2M – $3x10^{-4} m^2/s^2$ for RANS & $1,5x10^{-3} m^2/s^2$ for 2M.

Comparing the LES models with the Kolmogorov Theory. To examine the behavior of the LES models, the turbulent (frequency and wave number) energy spectra were provided [4,5]. The frequency spectra of the 3 LES models are shown on Fig. 4. The turbulent spectra show how the energy of turbulence is dissipated in the domain for each frequency. As the eddy is getting smaller, its frequency is getting higher, providing a faster fluctuation. The energy of turbulence is transported from large scales to small scales where it is damped by viscosity – that is why the spectra are decaying at the higher frequencies.

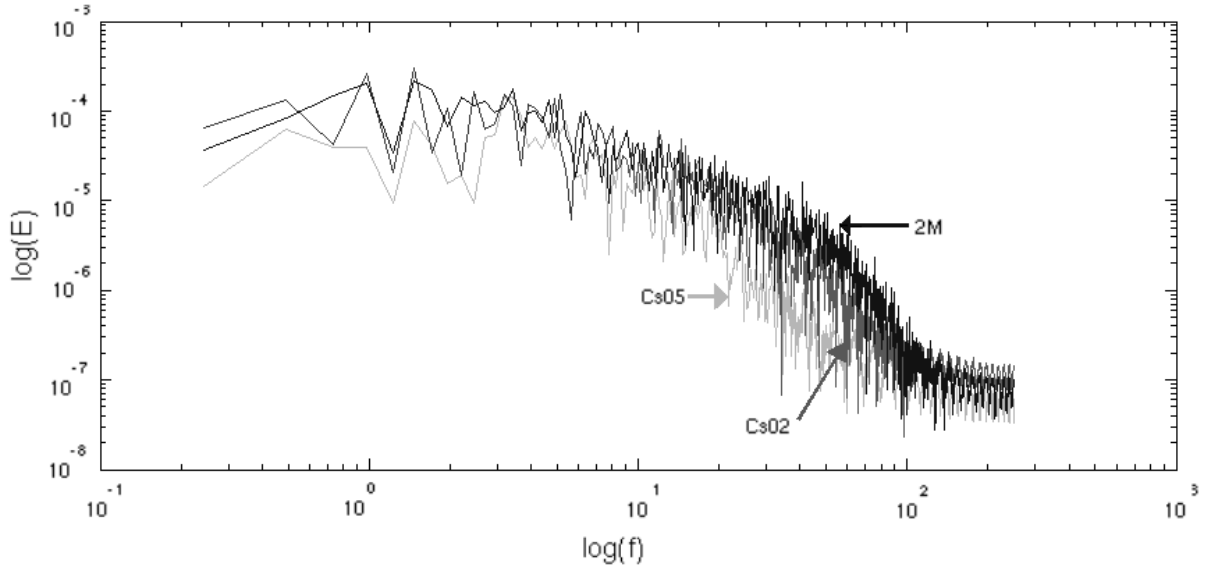

Figure 4. Turbulent frequency spectra of each LES model at 7 s of flow time

The spectrum of Cs05 decays more rapidly, that confirms the filtering phenomenon of the small scales in the liquid, whereas 2M decays last – as expected – which means, that there are more and smaller eddies in the flow. Using Taylor hypothesis, the turbulent wave number spectrum and the compensated spectrum were provided for the 2M model. To be able to make the compensated spectrum, the turbulent dissipation rate is needed – see the following equation:

$$E_{comp} = E(\eta)\, \varepsilon^{-2/3}\, \eta^{5/3} \tag{2}$$

Where *E(η)* is the original wave number spectrum, *η* is the (characteristic) wave number and *ε* is the turbulent dissipation rate. The wave number of turbulence is similar to the frequency, but it describes the number of waves (turns of eddies) per unit time. The latter can be computed in several ways and we used the following equation:

$$\varepsilon = u'^3/\lambda \tag{3}$$

where *u'* is the (azimuthal) velocity fluctuation and *λ* is the turbulent wavelength – the size of the eddy. *λ* and *η* can be computed by means of Taylor hypothesis with the following equations:

$$\eta = 2\pi/v_{av} f \tag{4}$$
$$\lambda = 2\pi/\eta \tag{5}$$

where v_{av} is the average local azimuthal velocity and f is the turbulent frequency. The turbulent wavenumber spectrum is produced with the replacement of the frequencies with the wavenumbers. To be able to estimate the characteristic wavenumber, the inertial range of the spectrum has to be found. For this, the *Kolmogorov line* can be used.
The function of the Kolmogorov line (for wave number spectrum) is:

$$E_{Kolm} = \eta^{-5/3} \tag{6}$$

The inertial range corresponds to the spectrum range where the Kolmogorov line runs identically. After determining the minimum and maximum η or f value in this region, the average of them is used as the characteristic wave number or frequency. The frequency spectrum with the Kolmogorov line for 2M at 7 seconds of flow time can be seen in fig. 5.

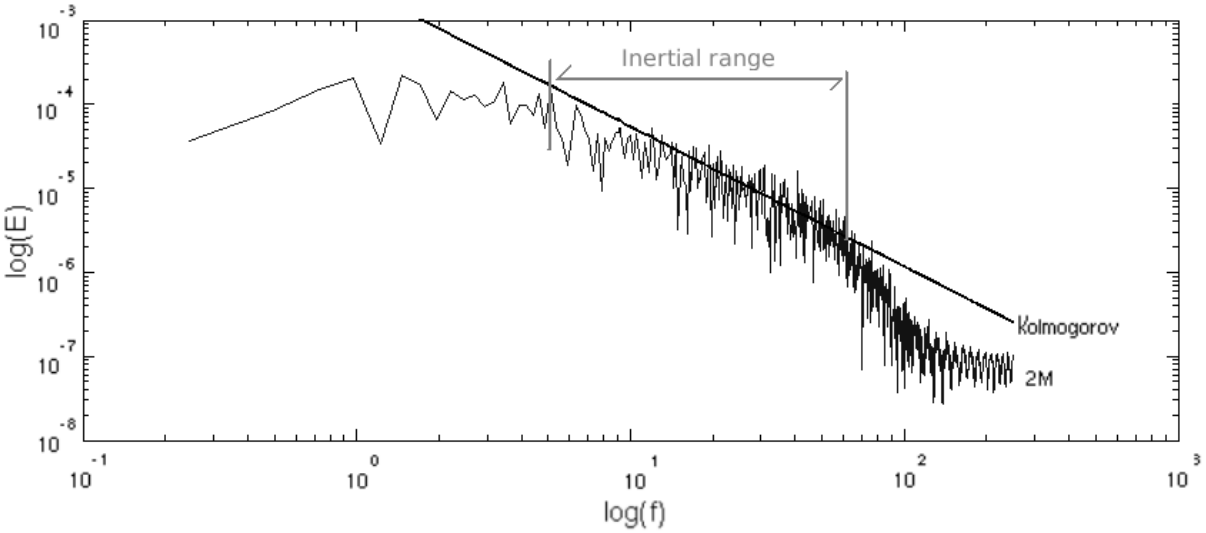

Figure 5. The frequency spectrum of 2M with the Kolmogorov line – at 7 s of flow time

The turbulent dissipation rate was computed only for the 2M model. The RANS has 50 times smaller dissipation than 2M – 0,002 m^2/s^3 & 0,101 m^2/s^3.

The original and compensated wavenumber spectrum can be seen on Fig. 6 for the 2M model at 68,536 seconds of flow time. These spectra have to be provided from at least one minute of flow time for a well-developed turbulent flow – to have correct information about the length scales. If the compensated spectrum reaches the well-defined *Kolmogorov constant,* $C_k = 1,5$ [4], the model provides a reliable physical information about the flow. If the compensated spectrum is well defined and the turbulence is well developed, it can also show the inertial range – where the compensated spectrum reaches the value of C_k.

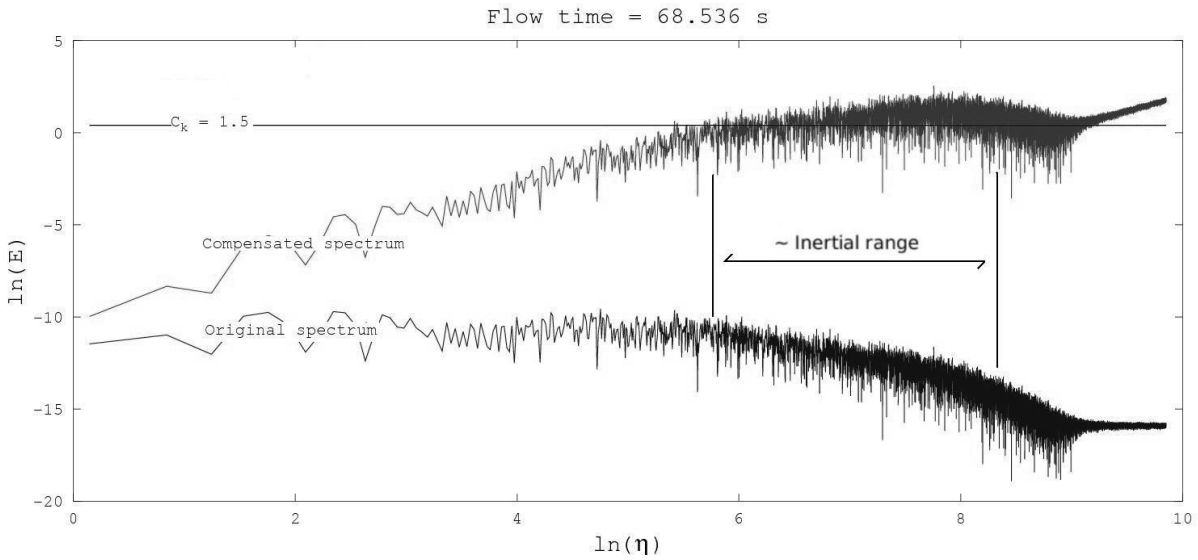

Figure 6. Original and compensated wavenumber spectrum of turbulence – at 68,5 s of flow time, 2M

Comparing the results with measured angular velocity. To be able to determine the accuracy of the simulated flow, a comparison has been achieved with measured angular velocity data. The measurements were made with *pressure compensation method*. Detailed information can be found in [3]. Other measured velocity components are not available for our system, so just volumetric average of the primary flow is compared. The results can be found in Table 1.

Table 1. Measured and simulated volumetric average angular velocities

	ω (rad/sec)	Rel. error (%)
Measured	38,83	-
RANS	31,79	-18,14
Cs02	39,47	1,64
Cs05	37,79	-2,68
2M	37,82	-2,61

In this case the relative error of the RANS is quite high, but generally 3-10 % error could be reached with other models with other magnetic induction [1,2]. The LES models seem to be much more accurate.

Summary

Several numerical simulations were done to provide a very accurate turbulent model of the electromagnetic stirring of liquid metals – here eutectic Ga-In. The results of RANS model suggests that too much averaging is used. The flow pattern seems to be too ordered to be realistic. However, the LES models provides statistically a more accurate primary flow and qualitatively more realistic secondary flow pattern.

Acknowledgements

The scientific work was supported by the *MICAST-ESA-MAP AO-99-031 project.*

This research was supported by the *European Union* and the *State of Hungary, co-financed by the European Social Fund* in the framework of TÁMOP 4.2.4. A/2-11-1-2012-0001 '*National Excellence Program*'.

References

[1] Cs. Nagy, L. Gyulai, A. Rófaföldi, A. Roósz; Investigation of the hydrodynamic properties of magnetically stirred molten gallium-indium alloy by numerical simulation. Materials Science And Engineering, vol. 39, (2013) pp. 41-50.

[2] Cs. Nagy, A. Rónaföldi, A. Roósz: Comparison of measured and numerically simulated angular velocity of magnetically stirred liquid Ga-In alloy. Materials Science Forum, vol. 752, p. (2013) pp. 157-166.

[3] A. Rónaföldi, J. Kovács, A. Roósz: Revolution number (RPM) measurement of molten alloy by pressure compensation method. Materials Science Forum, vol. 649. (2010) pp. 275-280.

[4] F. Felten, Y. Fautrelle, Y. Du Terrail, O. Metais; Numerical Modelling of Electromagnetically-Driven Turbulent Flows Using LES Methods. App. Math. Modelling, vol. 28, n°1, (2004) pp. 15-27.

[5] A. Bakker: Lecture 9 - Kolmogorov's Theory, Applied Computational Fluid Dynamics. Educational material. © Fluent Inc. (2002)

Effect of Electromagnetic stirring on the solidification of Al-7wt%Si alloy: experiment and simulation

Csaba Nagy[1,2,3], Olga Budenkova[2,3], Yves Du Terrail[2,3], Yves Fautrelle[2,3], András Roósz[1]

[1] University of Miskolc, Miskolc-Egyetemváros, H-3515, Hungary
[2] Univ. Grenoble Alpes, SIMAP, F-38000 Grenoble, France
[3] CNRS, SIMAP, F-38000 Grenoble, France
Corresponding author: ntsart@gmail.com

Abstract
To understand resulting effect of an electromagnetic stirring during solidification of alloy one should use either well-controlled experiments or numerical simulations. In the present work experiments on solidification of Al-7wt%Si alloy with RMF stirring performed in University of Miskolc are presented. Temperature data obtained during the experiments are used for simulations which are performed with a purely columnar solidification model. The numerical code developed in the SIMAP laboratory based on the ensemble averaged multiphase model with the envelope approximation is used for the simulations.

Keywords: electromagnetic stirring, solidification, alloy, simulation, envelope model, segregation

Introduction
Alternating electromagnetic fields are widely used in alloys solidification to control the structure of the material. Generally, convection leads to a smaller primary and secondary dendrite spacing due to more intense mass transport in the liquid phase. Eventual fragmentation of solidified dendrites also promotes finer solidified structure. On the other hand forced convection can have negative impact because of directed mass flow through the mushy zone which leads to the segregation. Furthermore, transport of dendrite fragments also can affect composition distribution [1]. To examine these phenomena, two laboratory setups for directional solidification equipped with electromagnetic stirrer were constructed and equipped with thermocouples allowing for the temperature measurement along the sample during the solidification [2]. Obtained data were used in simulations of solidification process.

The solidification facility and experimental results
The sketch of the solidification facility is shown in Fig. 1. The Ø8x100 mm sample is placed into a holder cartridge whose lateral wall allows for the placement of 13 thermocouples lengthwise for the temperature data collection. The cartridge is connected to a copper cooling core and is placed into a quartz tube – making the sample holder assembly. The copper core is constantly in the water to provide a heat flux for the solidification. The whole sample is kept in a rotating magnetic field during the solidification experiment.

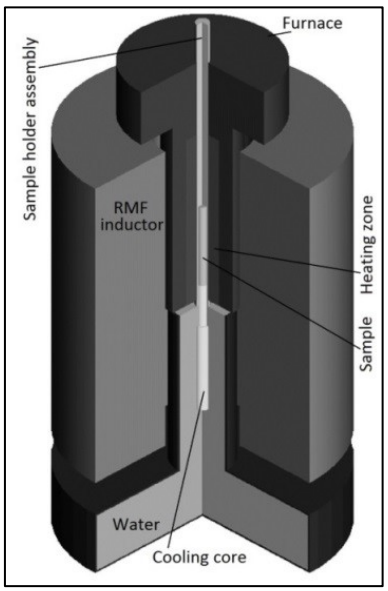

Fig. 1: The solidification facility equipped with RMF stirrer

The experiments are performed as follows:

1. The sample is heated up over a liquidus temperature,
2. An initial temperature gradient is set up in the sample using the cooling rod and the lowest zone of the furnace,
3. The lowering of the sample holder assembly is started – optionally with RMF stirring – to induce solidification.

The temperature field is recorded with National Instruments® data collector tool using a LabView® program. There are 3 zones in the furnace and the lowest zone is set to a higher temperature. In the beginning of the experiment the lower half of the sample is in the lowest hot zone, while the upper part of the sample is in a middle furnace zone which is colder. During the sample drawing its upper part first pass a warmer zone. Due to this, the thermocouples at higher positions first record an augmentation of the temperature, and then the cooling occurs as seen in Fig. 2.

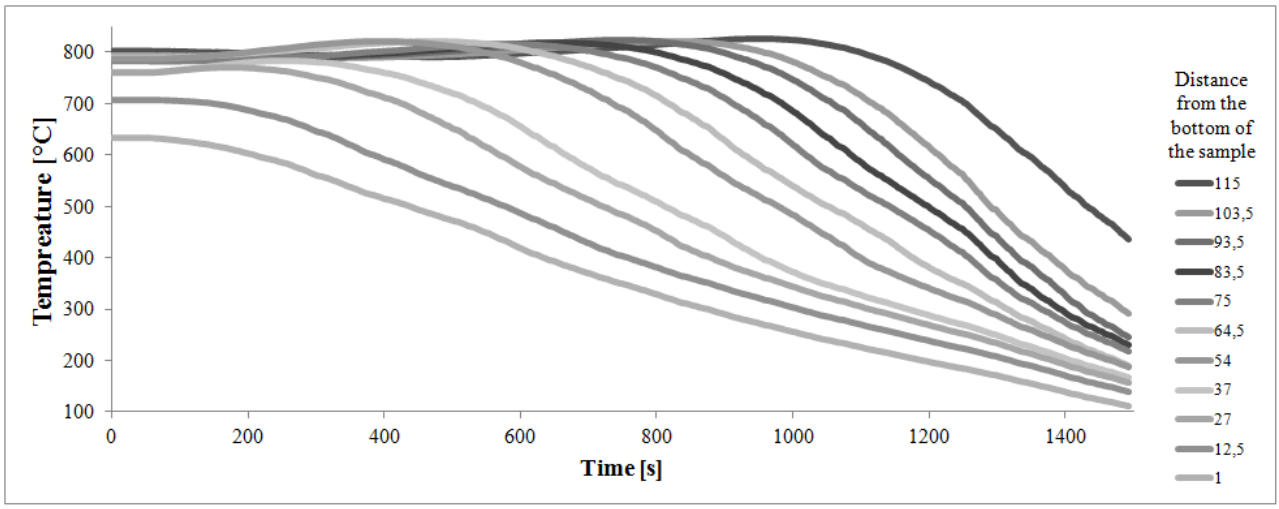

Fig. 2: Cooling curves obtained from the thermocouples during the solidification experiment with B=6 mT

The structures of two directionally solidified samples with and without electromagnetic stirring are shown in Fig. 3. As a result of the secondary flows, a strong central segregation appears.

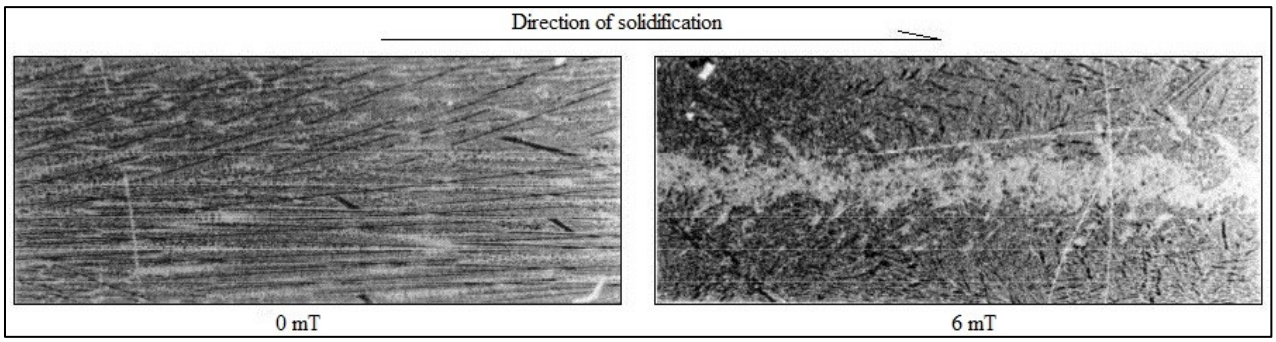

Fig 3: Microstructure of directionally solidified Al-7Si samples with (right) and without (left) RMF stirring. Light grey color corresponds to a higher concentration of the Si (eutectic structure).

Two-dimensional and three-dimensional modeling

We perform 2D and 3D modelling for the experiments in order to capture three-dimensional effects of the flow and their effect on the segregation. Two-dimensional modelling is made with an axisymmetric swirl for a rectangular calculation domain 4x100 mm meshed with 40000 uniform tetragonal cells. In three dimensions the calculations are made for a cylinder of 100 mm high and 8 mm diameter using 510600 hexahedrons with the biggest skewness 0.54. The modeling is performed with a commercial code Ansys Fluent® with UDF functions. . Both models have the same user defined functions written for the phase transition during the solidification and for the specie transport with segregation at the solid-liquid interface [3-4].Two hydrodynamic phases are considered, solid and liquid and Euler model is used. Three thermodynamic phases, namely, solid, interdendritic- and extradendritic liquid are considered according to the envelope model [5-6]. The induced Lorenz force field is set as momentum source using analytical approximation since the length of the inductor is larger than that of the sample [7]. Darcy law is used to model the flow through the mushy zone.

Previous two-dimensional modeling was made for such experiments but with adiabatic conditions at the lateral wall, a given cooling rate at the bottom and a fixed thermal gradient at the top. In the present case the temperature dataset of experiments is used as a boundary condition along the lateral wall of the calculation domain. A linear interpolation in space for calculation points is made because there are 10 data points for 100 mm height, which are two orders of magnitude less than the number of cells along the height Fig. 5. Interpolation in time is also needed since the data collection interval is much higher than the used time steps in the model and also.

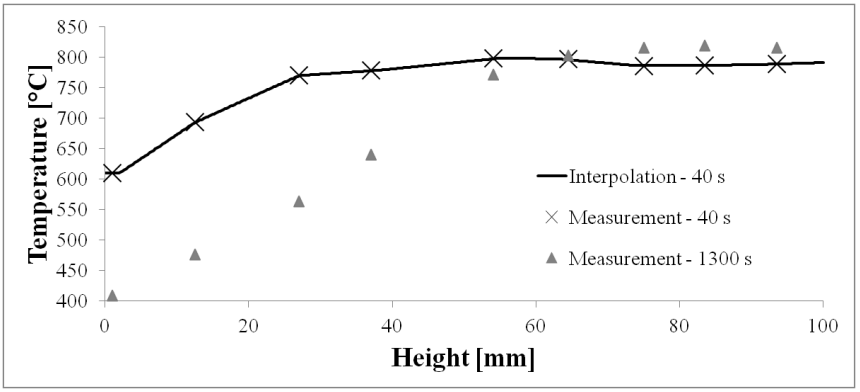

Fig 5: Temperature distribution along the sample from measurements and interpolation

Results of two-dimensional simulations

In Fig.6 results for the flow in the crucible and initial stage of the solidification are presented. In this case the flow consists of small vortices moving downward and upward near the lateral wall. An averaged axial flow may be identified in the center of the sample which is directed upward in the lower part of the sample and is descending for its upper half. The solidification started with a strong central segregation, but due to the temperature field, the whole cross section has been closed by the mushy zone. The blocked melt with higher concentration solidifies later than the melt near the wall (Fig 6.).

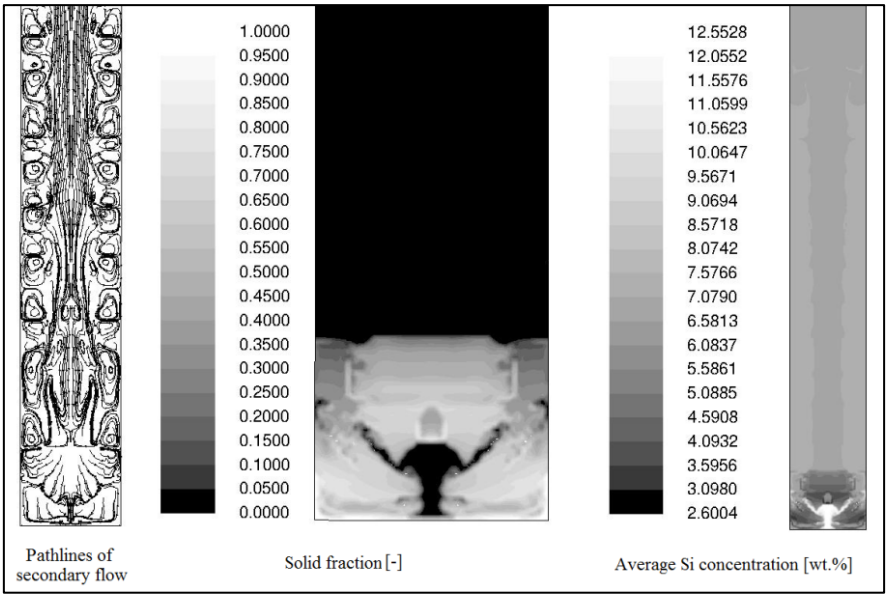

Fig. 6: Intermediate results of the 2D model at 95.26 seconds flow time

Results for three-dimensional simulation

The 3D model's computational time per time step is about 50-60 times higher than the 2D, so the following intermediate results can be presented. Similar to the 2D case, the induced secondary flow provides a central segregation and slows down the solidification process in the center as shown in Fig. 7.

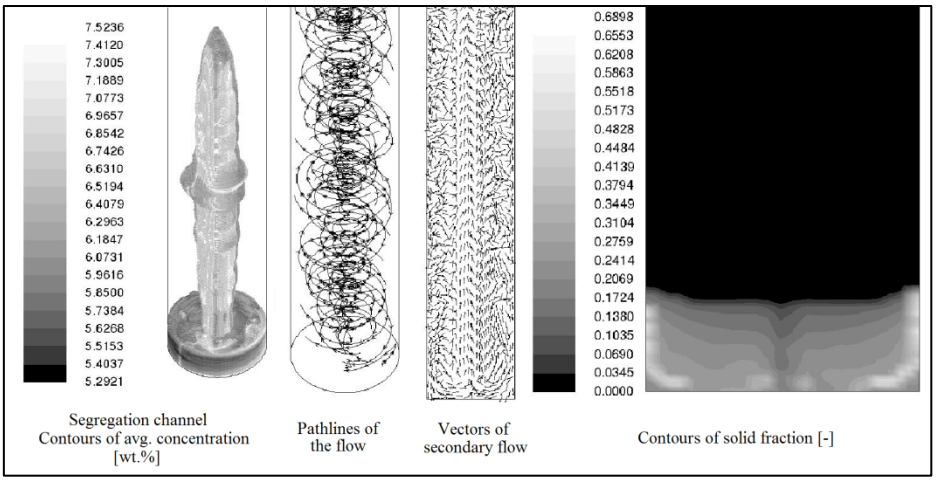

Fig. 7: Intermediate results of the 3D model at 24.7 seconds flow time

The need of the 3D domain is proven on Fig 8. The flow is shifting between axis-symmetric and asymmetric from one time step to another.

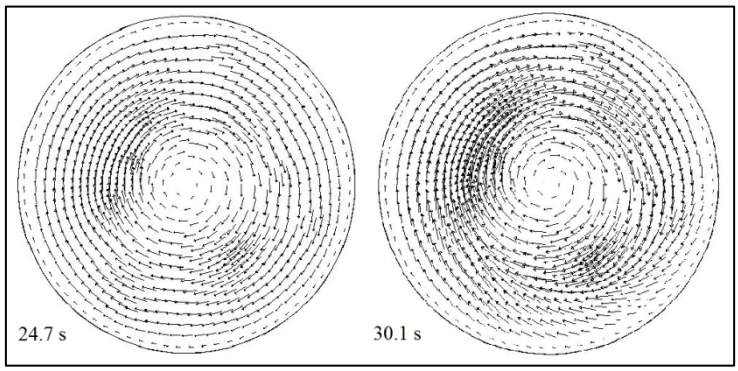

Fig. 8: Shifting between axis-symmetric and asymmetric flow pattern presented by vectors of velocity magnitude

Summary
A facility for examining the solidified structure of different alloys under natural or forced convection has been developed; and used for Al-7Si binary alloy. The solidified structures and a concentration map are presented. With the aid of the collected temperature data, 2D axisymmetric and 3D solidification models are provided using ensemble averaged envelope model.

Acknowledgements
This research was supported by the European Union and the State of Hungary, co-financed by the European Social Fund in the framework of TÁMOP 4.2.4. A/2-11-1-2012-0001 'National Excellence Program' (Nagy Csaba).

The collaboration between the French and Hungarian team was supported by CNRS PICS-2014 project 231386.

References
[1] L.Hachani, I.Kaldre, J.Wang et al. (2014), Mat.Sci.Forum, 790-791, 375-383
[2] J. Kovács, G. Gergely, Z. Gácsi, A. Roósz, A. Rónaföldi (2007), Trans. Indian Inst. Met. Vol.60, Nos. 2-3, 149-154
[3] A. Ciobanas and Y.Fautrelle (2007), J. Phys. D: Appl. Phys., 40, 3733–3762
[4] H Combeau, M Bellet, Y Fautrelle, D Gobin, E Arquis, O Budenkova, B Dussoubs, Y Du Terrail, A Kumar, C -A Gandin, B Goyeau, S Mosbah, T Quatravaux, M Rady and M Založnik (2012), IOP Conf. Series: Materials Science and Engineering, Vol 33, 012086
[5] M. Rappaz, P.h. Thévoz (1987), Acta Metallurgica 35, 1487–1497
[6] C. Y. Wang, C. Beckerman (1993), Materials Science and Engineering, A 171, 199-211
[7] O. Budenkova, A. Noeppel, J. Kovács, A. Rónaföldi, A. Roósz, A.-M. Bianchi, F. Baltaretu, M. Medina and Y. Fautrelle (2010), Materials Science Forum, Vol.649, 269-274